Power Electronics Design and Simulation of a Solar House

Zahra Asadi

A Thesis

in

The Department

of

Electrical and Computer Engineering

Presented in Partial Fulfillment of the Requirements

for the Degree of

Master of Applied Science (Electrical and Computer Engineering) at

Concordia University

Montréal, Québec, Canada

November 2022

CONCORDIA UNIVERSITY
SCHOOL OF GRADUATE STUDIES

This is to certify that the thesis prepared

By: Zahra Asadi

Entitled: Power Electronics Design and Simulation of a Solar House

and submitted in partial fulfillment of the requirements for the degree of

Master of Applied Science (Electrical and Computer Engineering)

complies with the regulations of this University and meets the accepted standards with respect to originality and quality.

    Signed by the final examining committee:

_____ Chair
            Dr. Luiz Lopes

_____ Internal Examiner
            Dr. Chunyan Lai

_____ Supervisor
            Dr. P. Pillay

    Approved by: _____
                        Dr. Yusef R. Shayan, Chair
                Department of Electrical and Computer Engineering

                        _____
                            Dr. Mourad Debbabi, Dean,
                    Faculty of Engineering and Computer Science

Abstract

Power Electronics Design and Simulation of a Solar House

Zahra Asadi

The increasing trend of Earth's temperature in the past century has made the world search for solutions to preserve our planet in a livable condition and prevent the climate from exacerbating. Becoming net-zero energy can pave the way to achieving the global goal of reducing gas emissions and saving the planet. This can be done by practicing various approaches. Switching to renewable energy sources in the residential sector, which accounts for a considerable portion of global energy consumption, is one of the most effective ways.

This study aims to design and simulate the power electronics of a research solar house located at the Loyola Campus of Concordia University, Montréal, Canada. This research facility is built to investigate numerous renewable energy systems that can help achieve the net-zero energy goal for a typical detached single-family dwelling in Québec. This building, known as Future Buildings Laboratory (FBL), has integrated renewable energy sources such as solar, solar-thermal, and wind which allow the opportunity of testing different scenarios.

In this research, the power electronic system of the solar power system of the FBL is simulated in PSIM software considering the rated load of the house and the ratings of the real-life system. other. The simulations are straightforward models of the actual system in three modes of operation: 1) grid feeds the load, 2) grid charges the battery, and 3) battery feeds the load. Each mode of operation is modeled as a unique circuit. Frequency-domain modeling of the system is also carried out in order to design the controllers. The system's transfer function is estimated considering the system as a black box and is compared with an analytically derived transfer function to check the accuracy of the estimation.

The last step is to validate the simulation results. For this, the third mode of operation is performed experimentally at the PEER group laboratory, Concordia University, using available converters, devices, and the real-time simulator (OPAL-RT). Various experiments are conducted to observe the performance of the simulated model in real conditions. The time-domain and frequency-domain experimental results closely match those acquired via simulation.

Acknowledgement

به نام خداوند گیتی فروز

In the name of God who lightens the universe

I would like to express my genuine gratitude to my supervisor Dr. Pragasen Pillay, who provided this opportunity to me so that I could further explore science under his valuable supervision.

I would like to sincerely acknowledge the guidance of Dr. Akrem Aljehaimi and Dr. Mathews Boby throughout this research.

I would also like to cordially thank my colleagues who made a home-like atmosphere in the PEER group lab. Nazanin, Amir, Sumeet, Yupeng, Gayathri, Mohanraj, Tamanwe, Neetusha, Bassam, Koteswara, Tolga, Talha, Tshamala, and Gabriel.

Finally, I would like to express my heartfelt appreciation to my parents Maryam and Fereydoon, my beloved sister Melina, and my one and only friend Matin who were always the most understanding in difficult times.

*This thesis is wholeheartedly dedicated to my uncle **Farid**.*

Table of contents

List of Figures

List of Tables

Nomenclature

AC	Alternative Current
BIPV/T	Building Integrated Photovoltaic/Thermal collector
CO₂	Carbon Dioxide
COP 24	2018 United Nations Climate Change Conference
DC	Direct Current
EHBE	Experimental House for Building Energetics
EV	Electric Vehicle
FBL	Future Building Laboratory
FEAR	Front-End Active Rectifier
FFT	Fast Fourier Transform
GHG	Greenhouse Gas
HCC	Hysteresis Current Control
IBR	Inverter-Based Resources
LEED	Leadership in Energy and Environmental Design
M.I.	Modulation Index
MPP	Maximum Power Point
NZEB	Net-Zero Energy Building
P	Proportional
PCC	Point of Common Coupling
PF	Power Factor
PI	Proportional-Integral
PID	Proportional-Integral-Derivative
PLL	Phase-Locked Loop
PR	Proportional-Resonant
PV	Photovoltaic
PWM	Pulse Width Modulation
RMS	Root Mean Square
SOC	State of Charge
SPWM	Sinusoidal Pulse Width Modulation
STPV	Semi-Transparent Photovoltaic
TF	Transfer Function
THD	Total Harmonic Distortion
UPF	Unity Power Factor
WT	Wind Turbine

Chapter 1 Introduction

1.1 Introduction

In this chapter, the question of why this research is done is answered. A brief explanation of the issue of global warming followed by the concept of net-zero energy buildings is presented. Then, the case study of this thesis is explained in detail.

1.2 Global warming and renewable energy use

As the observations have shown, the average earth's surface temperature has had an increasing trend since the pre-industrial period between 1850 and 1900 [1]. In 2020, the planet's temperature was above the baseline by one-degree centigrade as shown in Figure 1.1. The heating of the atmosphere, which leads to an increase in the earth's temperature, is caused by the trapped heat as a reason for the greenhouse effect [2].
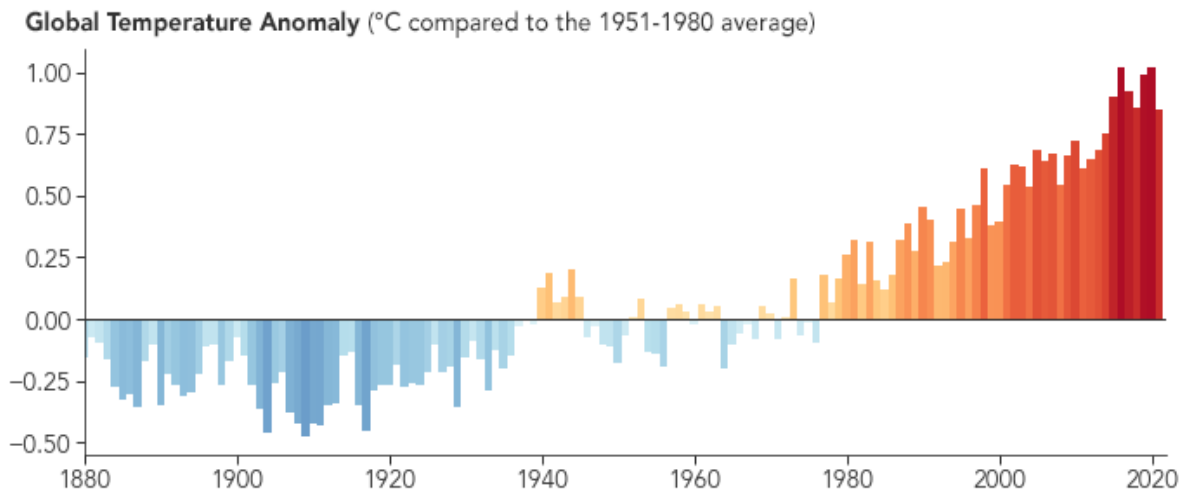
Figure 1.1 The change in the global average temperature relative to the average temperature during the period of 1951-1980 [1].

This has urged the world to find solutions to preserve a habitable climate. The global carbon footprint can be decreased in several ways. The United Nations presented ten potential solutions at the Climate Change Conference (COP24) in 2018, and two of those were the conversion of transportation to electric and the use of renewable energy sources for residential buildings [3]. The reason why most of the focus is on residential buildings is that this sector accounts for 25-30% of global energy consumption and CO_2 emissions [4], [5]. By adopting net-zero energy technologies,

it is possible to reduce energy consumption by a noticeable amount and therefore reduce the rate of global warming [6].

1.3 Net-Zero Energy Buildings (NZEBs)

Equipping buildings with more renewable energy sources results in having net-zero energy buildings, which means that the annual energy consumption for these buildings is offset by the energy generated from renewables [7]. Integrating solar panels and/or wind turbines into the electrical system of a residential building makes it possible to achieve the net-zero energy goal in the long term. Nowadays, many residential and institutional buildings across Canada use renewable energy sources to become completely net-zero or to reduce their carbon footprint to meet Canada's Greenhouse Gas (GHG) Emissions reduction target by 2030 [8]. Figure 1.2 shows the distribution of Canada's Photovoltaic (PV) capacity as of December 2020.
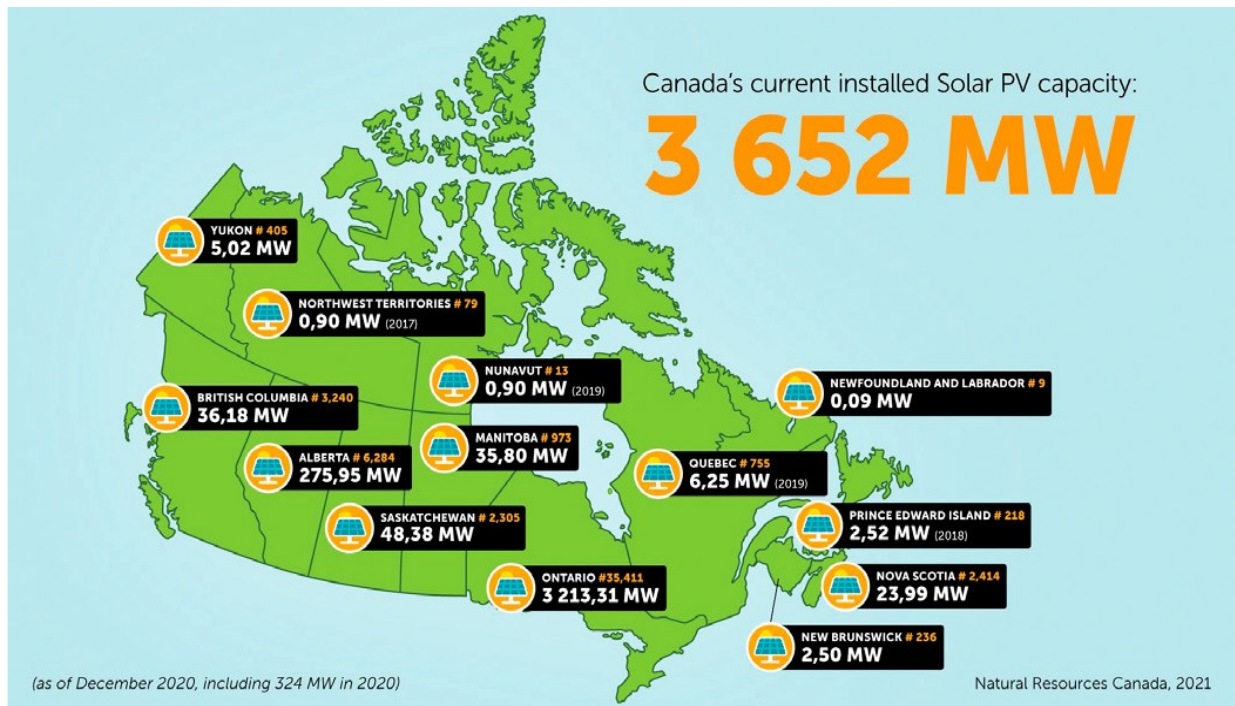
Figure 1.2 Canada's installed PV capacity as of December 2020 [9].

1.4 NZEBs in Canada

Many buildings across Canada are achieving the net-zero energy goal. Some have already reached the goal and some are in the middle of the race. Some examples are brought in the following subsections.

1.4.1 Varennes Library

Varennes Library which is shown in Figure 1.3, is the first institutional net-zero energy building (NZEB) in Canada that can produce as much energy as it needs from renewable resources in annual periods [10]. This 2,100 square-meter two-story building with 110 kW of solar panels on its 37-degree tilted southern roof has received the Leadership in Energy and Environmental Design (LEED) gold certificate [10], [11].

1.4.2 John Molson School of Business

Another example is the John Molson School of Business in Sir George Williams Campus, Concordia University. The nearly south-facing facade consists of a building-integrated photovoltaic/thermal system. This 288 m^2 system can simultaneously generate up to 25 kW of electricity and 75 kW of solar heat [12]. The southern view of the building is shown in Figure 1.4.

Figure 1.3 Varennes Library, Varennes, Québec [13].

1.4.3 Val-des-Ruisseaux

Apart from institutional buildings, many residential buildings also use renewable energy sources to reduce their annual bills or to become net-zero energy. The Val-Des-Ruisseaux Condos in Laval, Québec, are six net-zero energy condominiums in a three-story building that are built by Construction Voyer in partnership with National Resources Canada. The project has 150 solar

panels with 225 W each. It can produce 148.57 GJ of energy per year and its annual consumption is 146.49 GJ, which makes the building net-zero energy [14].

Figure 1.4 John Molson School of Business, Concordia University, Montréal, Québec.

1.4.4 Experimental House for Building Energetics

Another example of a residential building is the Hydro-Québec Experimental House for Building Energetics (EHBE) located in Shawinigan, Québec, which is shown in Figure 1.5. It is a two-story single-family detached house with a net area of 60 m^2 consisting of three bedrooms and one bathroom. It has on-site solar panels with a total capacity of 5 kW and lithium-ion batteries of 10 kWh. The building is 35 degrees towards the southwest [15]. This house is an unoccupied building and is mainly used as a research facility for net-zero energy technologies and is the closest available example to the case study of this thesis.

1.5 Future Buildings Laboratory

This thesis is focused on the analysis of the electrical power converters of the solar power system of a research facility located in Loyola Campus, Concordia University, Montréal, which is shown in Figure 1.6. It is called Future Buildings Laboratory (FBL). It is funded partially by the Canada Foundation for Innovation and led by the Centre for Zero Energy Building Studies (CZEBS) and in partnership with the Electrical and Computer Engineering department at Gina

4

Cody School of Engineering and Computer Science, Concordia University. The FBL is a single-family detached house for testing net-zero energy technologies.

Figure 1.5 EHBE, Shawinigan, Québec [15].

Figure 1.6 South-eastern view of FBL, Loyola Campus, Concordia University.

This house has the capability of using solar and wind energies to feed its loads. The house has four south-facing test cells (rooms) which can either act as an integrated system or each can act as an isolated system for testing purposes. Three rooms have semi-transparent photovoltaics (STPV) cells, and one has a Building Integrated Photovoltaic/Thermal collector (BIPV/T). The southern roof is tilted 45 degrees, based on the latitude of Montréal, to absorb the maximum solar irradiance throughout the year. On the roof, there are three racks built for the installation of PV arrays. The house is also equipped with 2 stands on the roof for the installation of wind turbines (WTs).

Moreover, the house is equipped with an electric vehicle (EV), which has a bidirectional charging capability.

1.6 Contribution

The contribution of this thesis is the illustration of the design and simulation of the time-domain and frequency-domain models for the power electronics of the solar power system for the FBL. The models are easy to comprehend, show the important characteristics of the real-life system, and are adequately precise. The advantage of this type of modeling and simulation is that it can illustrate the performance of the system and brings a more intuitive understanding of the solar power system, especially in the absence of the equipment or when the available information of the purchased equipment is not adequate enough to see through the inner components and how they work. An experimental setup for one operating mode (the battery system feeds the loads) is prepared, and the obtained experimental results are used to validate the simulated results.

1.7 Thesis organization

The thesis proceeds as follows.

Chapter 2. This chapter reviews the available material in the literature regarding the electrical aspects of NZEBs, available solar converters' topologies, and converters used in this thesis.

Chapter 3. In this chapter, different parts of the system are studied. The design, time-domain modeling, and frequency-domain modeling of the system are discussed. The results and parameters of the system are brought into detail.

Chapter 4. In this chapter, an experimental setup is made for one of the operating modes presented in chapter 3, and experiments are done to validate the simulated model and results.

Chapter 5. This chapter presents the conclusions and future work.

Chapter 2 Literature Review

2.1 Introduction

In this chapter, the literature on power converters and control techniques is brought for a better perception of the present academic research. The types of converters that are then used for this study are brought into further detail.

2.2 Power converters

Power converters are used in various forms throughout the industry. From transmission and generation to energy harvesting and implantation, different types of power converters are used [16]. In most power converters, the input comes from the utility grid, and the load can be either direct current (DC) with a constant or adjustable magnitude or alternative current (AC) with constant or adjustable frequency and/or magnitude [17]. Based on the type of input and output, there are four classes of power converters which are described in Figure 2.1 and are mentioned as follows [18].

I.   AC input → DC output: rectifier.
II. AC input → AC output: AC controller (adjustable magnitude) and/or frequency converter (adjustable frequency).
III. DC input →DC output: chopper.
IV. DC input → AC output: inverter.
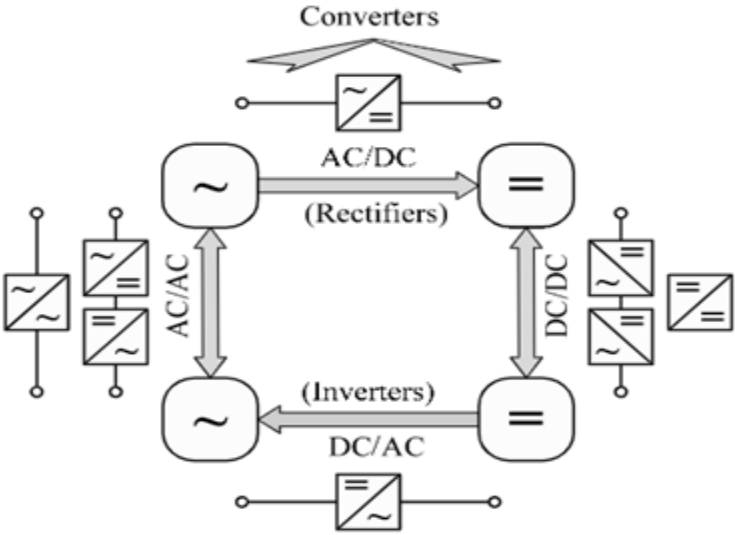
Figure 2.1 Types of power converters [18].

When integrating a renewable energy source into a microgrid, the use of a power converter(s) is always necessary. The reason is that the output voltage of a renewable energy source can be either unregulated DC or AC, and the loads require a certain DC or AC voltage to operate. For example, to feed an AC load using a PV panel(s), a regulator and an inverter are needed. Whereas a rectifier, a regulator, and an inverter are needed when feeding the same load from a wind turbine (WT). Therefore, based on the available input and the desired output, a certain type of power converter or a combination of power converters is needed for benefiting from renewable energy sources. Hence, these renewable energy resources (PVs and WTs) are also called inverter-based resources (IBR) [19].

When there is an on-site generation, the microgrid can operate in either grid-following or islanded modes [20, 21, 22, 23]. The two important types of inverters that are used in these applications are 1) grid-following inverters and 2) grid-forming inverters. Grid-following inverters follow and match the magnitude and phase of the grid at the output. Grid-forming inverters, on the other hand, generate a grid-like voltage at the output in case of grid failure so that the loads, which were previously connected to the grid, are connected to the output of these inverters and see a regular grid voltage. This is an off-grid or an islanded microgrid operation. The most important features of these converters are brought up in the following sections.

2.3 Grid-following inverters

These inverters are connected to the grid at the point of common coupling (PCC) and inject currents into the grid as seen in Figure 2.2. Therefore, their output voltage is an AC in phase with the grid. Thus, the measurement of the grid's phase and control of the output voltage are important aspects of these inverters.

2.3.1 Control of grid-following inverters

There are many control methods with a different number of loops and feeding for grid-following inverters. As an example of the grid-following inverters' control, a single-phase inverter with an LCL filter in the output can be controlled for different voltages and currents [24], [25].

Like other inverters, different types of controllers (compensators) can be used in the control loops based on the parameters that need to be controlled [26], for example, Proportional (P),

Proportional-Integral (PI), Proportional-Integral-Derivative (PID), Proportional-Resonant (PR) [27], and Hysteresis Current Controllers (HCC) [28, 29, 30].
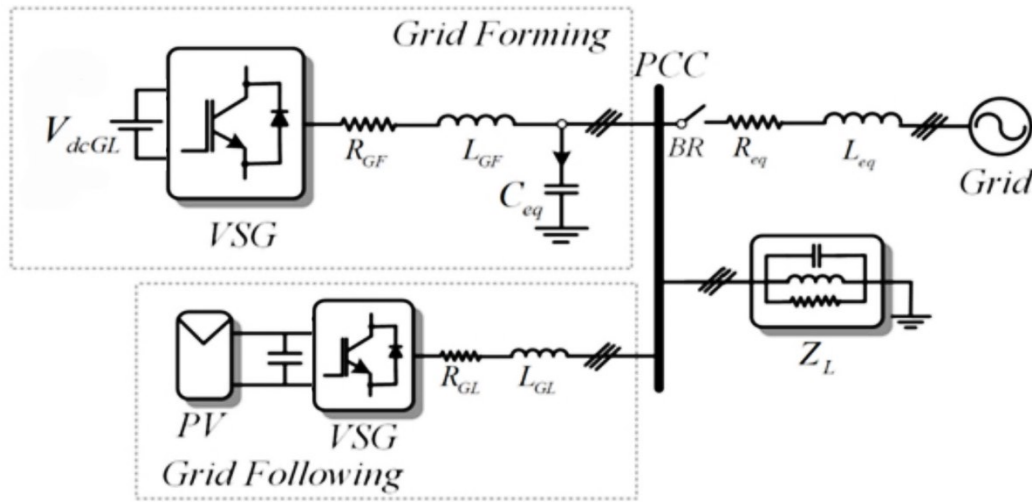
Figure 2.2 Grid-connected (grid-following and grid-forming) inverters connections to the PCC in the microgrid [31].

2.4 Grid-forming inverters

Grid-following inverters are designed and built based on the assumption that the grid is always present. They stop working in case of a power failure because there is no grid voltage available for the regulation of their output magnitude and phase [31]. By integrating more and more renewable energy sources, the use of these inverters cannot guarantee the stability of the grid in case of a partial or full power shutdown [32]. Hence, in the near future, the grid will become more and more dependent on the grid-forming inverters as shown in Figure 2.3 [32].

Grid-forming inverters play an important role in case of power failures. When a sudden power shut-down occurs, a transition from grid-following mode to grid-forming (islanded) mode is done. Grid-forming inverters generate a grid-like voltage at the PCC and feed the loads that need power with the same voltage characteristics as the grid as shown in Figure 2.2. Based on the load that is connected to the PCC, grid-forming inverters can provide the amount of power needed [33]. One of the advantages of grid-forming inverters is the ability to black-start without the need for any external voltage source for regulation purposes [33].

9
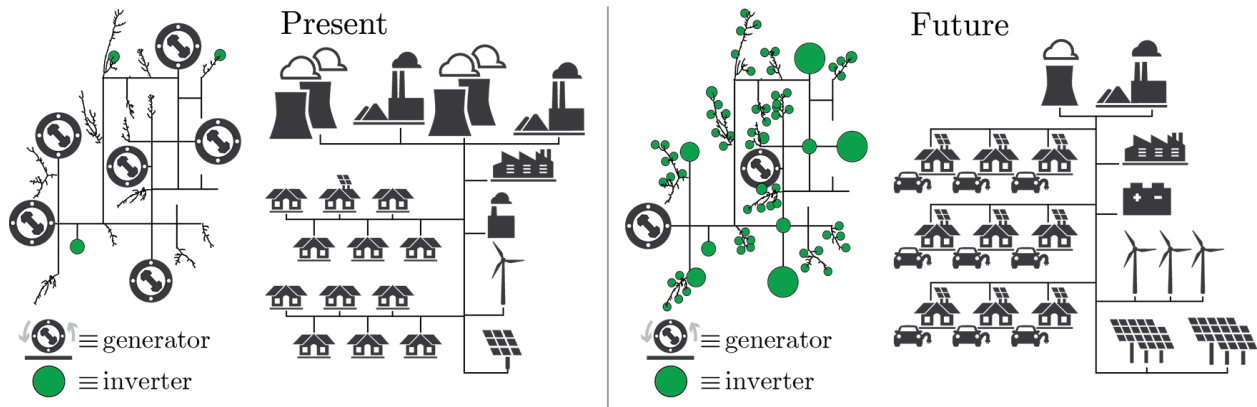
Figure 2.3 Future of the grid with the dominance of IBRs [32].

2.4.1 Control of grid-forming inverters

The two most important aspects of these inverters are voltage and frequency control. [34] has reviewed the control techniques of grid-forming inverters or in more correct terms, voltage-forming or grid-voltage-forming inverters. Various approaches of control [35] are available in literature such as droop control [36, 37], power synchronization techniques [38, 39, 40], voltage control, and Phase Locked Loop (PLL) based control [41, 42, 43, 44].

2.5 Inverters in this research

The goal of this thesis is to model the electrical parts of the solar power system, in an uncomplicated and straightforward manner so that the performance of the real-life system can be easily observed in the time-domain and frequency-domain models. The solar power system was previously measured by a technician and the components were ordered from the manufacturer. However, the components are considered black boxes as zero/little information is available on the inner connections and circuits except that on the input and output characteristics. In this thesis, the modeling of the grid-forming inverter is done.

2.6 Grid-forming inverter topologies

Grid-forming inverters are controlled voltage-source converters with the ability to black-start the system and create an AC voltage at the PCC [45, 46]. The most general topology consists of a switch-mode converter with a pulse width modulation (PWM) generator unit, which is controlled by one of the mentioned methods in 2.4.1, and a filter, usually LC or LCL, which connects the converter to the PCC. The inverter may be connected to the PCC via a transformer if it is inverting

the DC voltage to an AC voltage or connected directly if the voltage has been boosted in previous stages [31, 47].

In reference [47], a topology for a three-phase grid-forming inverter and its control scheme is proposed. The topology includes three legs for the switch-mode inverter, an LCL filter for the AC voltage smoothing, and a step-up transformer between the inverter and the PCC. A power-balance-based synchronization system is used for the inverter as shown in Figure 2.4 [47].

In this topology, an LCL filter is used which makes the voltage and the current highly smooth at the PCC, but it also adds a zero to the system which makes the control of the output voltage more difficult if proper values are not selected for the filter [47].

[48] has also used a transformer to step-up the voltage at the PCC and has used the PV array voltage as the DC input. The advantage of the transformer is that it isolates the inverter form the grid, but on the other hand, it exhibits a significant voltage drop. The voltage drop happens because of the winding impedance of a non-ideal transformer which causes power loss in the system.
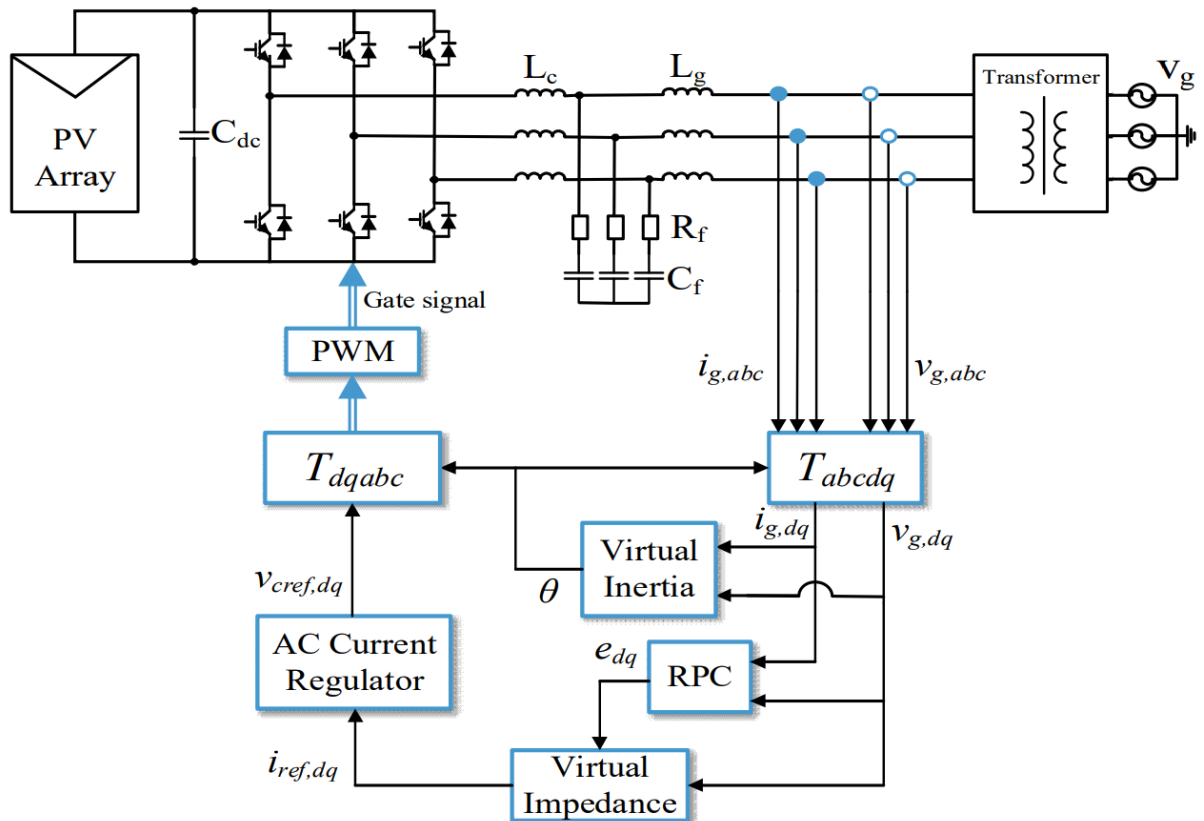
Figure 2.4 Grid-forming inverter topology and control scheme proposed in [47].

Reference [48] has discussed the two basic control schemes of grid-forming inverters. In the first method, the inverter is seen as a voltage source. So, the only parameters that need to be controlled are the voltage's amplitude and frequency without the need for a PLL. The second method controls the output voltage via PI controllers in the *dq*-frame. Figures 2.5 and 2.6 show the two mentioned methods. [48] discusses that both control schemes give the same results; however, the first method is much simpler to implement.
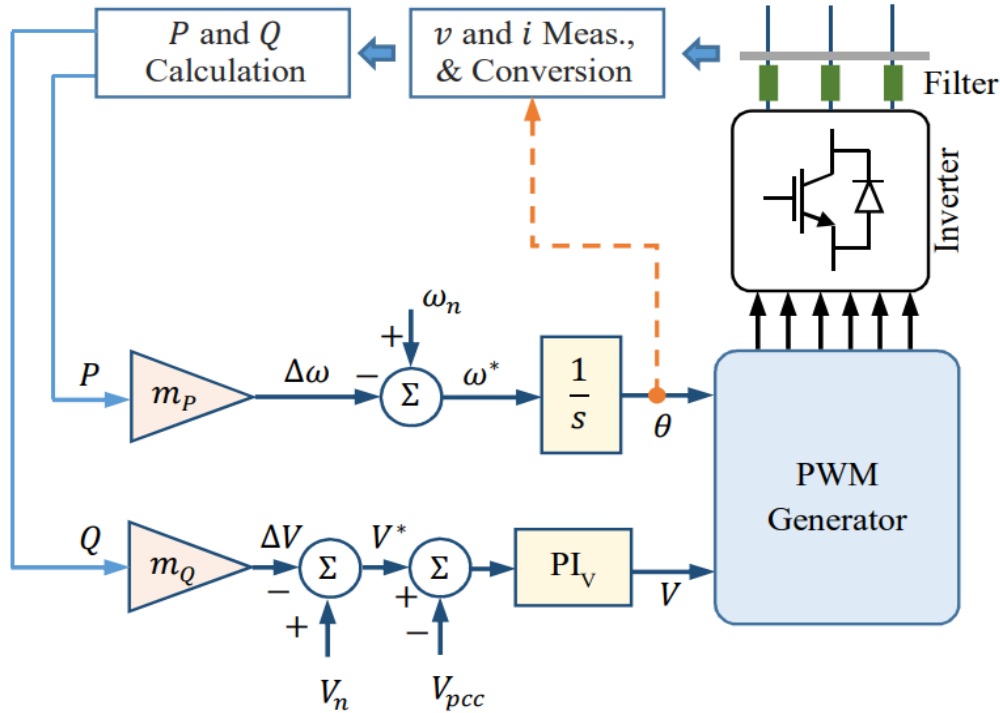
Figure 2.5 Grid-forming inverter with droop-based voltage control [48].

2.7 Proposed grid-forming inverter topology

An effort is made to figure out a topology that is easy to implement in both simulation and practice, shows the most important features of the ordered black-box inverter, and has the closest performance to the commercial device.

In this thesis, the adopted converter consists of a DC/DC boost converter to step-up the DC input voltage, a switch-mode single-phase converter with a bipolar Sinusoidal PWM (SPWM) scheme, and an LC filter that connects the inverter to the PCC. The voltage of the DC-link between the two converters is controlled by a PI controller. The inverter topology, the design, and the simulation process are discussed in detail in Chapter 3.

The benefit of the DC/DC converter is to eliminate the need for a step-up transformer. Although the isolation from the PCC increases the safety of the system, the transformers are bulky, expensive, and create a voltage drop which results in loads drawing more current to meet their operating power level.
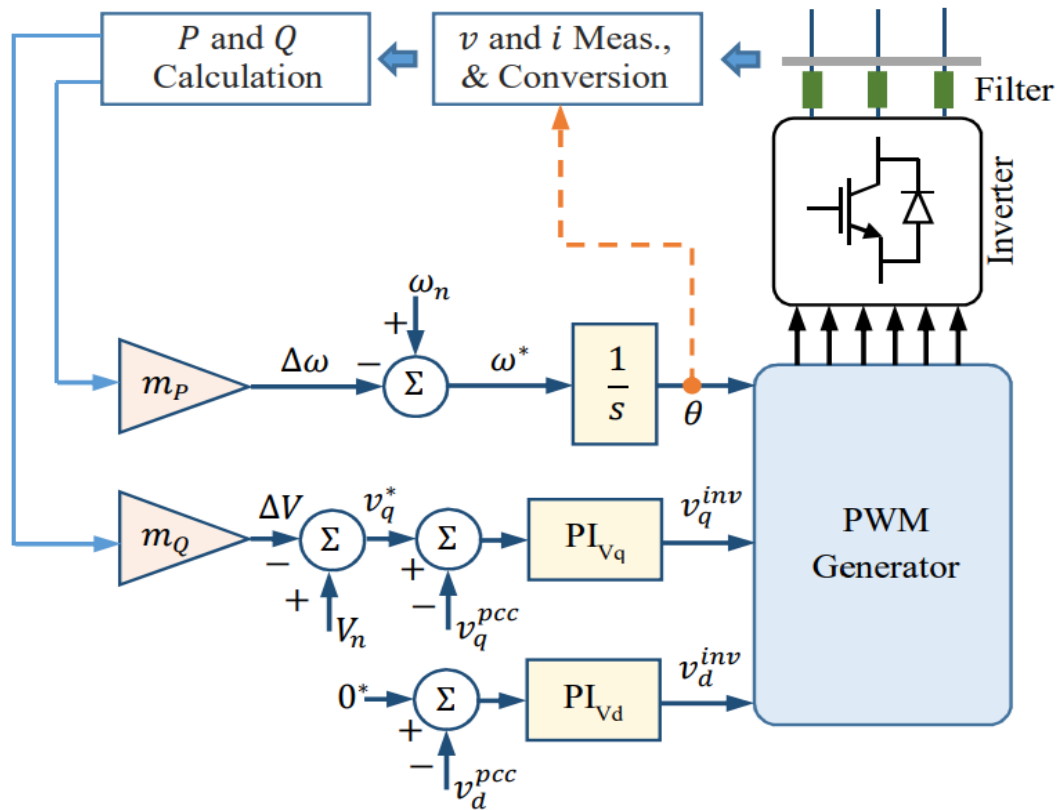
Figure 2.6 Grid-forming inverter with voltage control in the *dq*-frame [48].

2.8 Summary

In this chapter, the literature on power converters is presented. The inverters which are the most important type of converters in the future of the IBR-based grids are reviewed. The control techniques and types of compensators are also presented. In the next chapter, the solar power system of the FBL is brought into further detail.

Chapter 3 FBL's Solar Power System

3.1 Introduction

In chapter three, the details of the solar power system are brought along with the characteristics of the devices used. Different modes of operation of the system are designed and simulated. The results of the time-domain modeling are presented in this chapter.

3.2 Solar power system and devices

Based on the specifications of the house such as its size, load, resources, etc., a commercial system was designed by a licensed electrician to benefit from the solar energy captured via PV panels. The knowledge of the house's original electrical system was needed to find the best way of connecting the solar power system. A block diagram of the original system is shown in Figure 3.1. The grid input of 600 V and 225 A is connected to the Δ-Y 600-120/208 V, 150 kVA transformer. The stepped-down voltage is connected to the distribution panel, which then feeds the loads. The total load of the house is 70 kVA.
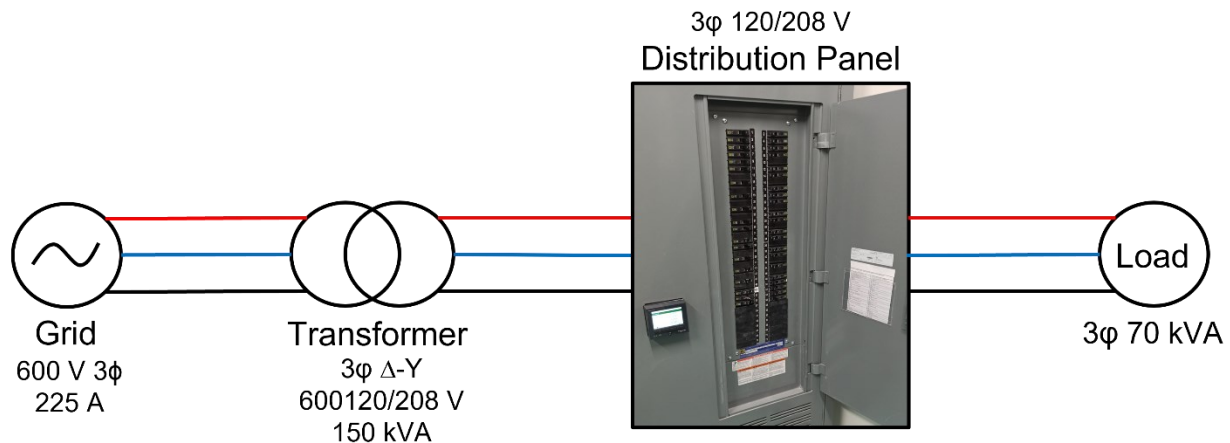
Figure 3.1 Block diagram of the electrical system of the house.

The solar power system is connected in parallel to the original system as in Figure 3.2. This is done by connecting the input and output of the solar power system to two three-phase 70 A circuit breakers inside the distribution panel which are shown as Disconnector 1 and Disconnector 2 in Figures 3.2 and 3.3. The connection is done in a way that there will be no interference with the original system. The system consists of three grid-following inverters, three grid-forming inverters, and six batteries. The connection of the solar power devices is illustrated by the block

diagram in Figure 3.3. The output of each grid-following inverter is connected to two lines at the PCC and the output of each grid-forming inverter is connected to a single line. So, the three inverters of each type will make a three-phase connection at the PCC to feed the three-phase load.
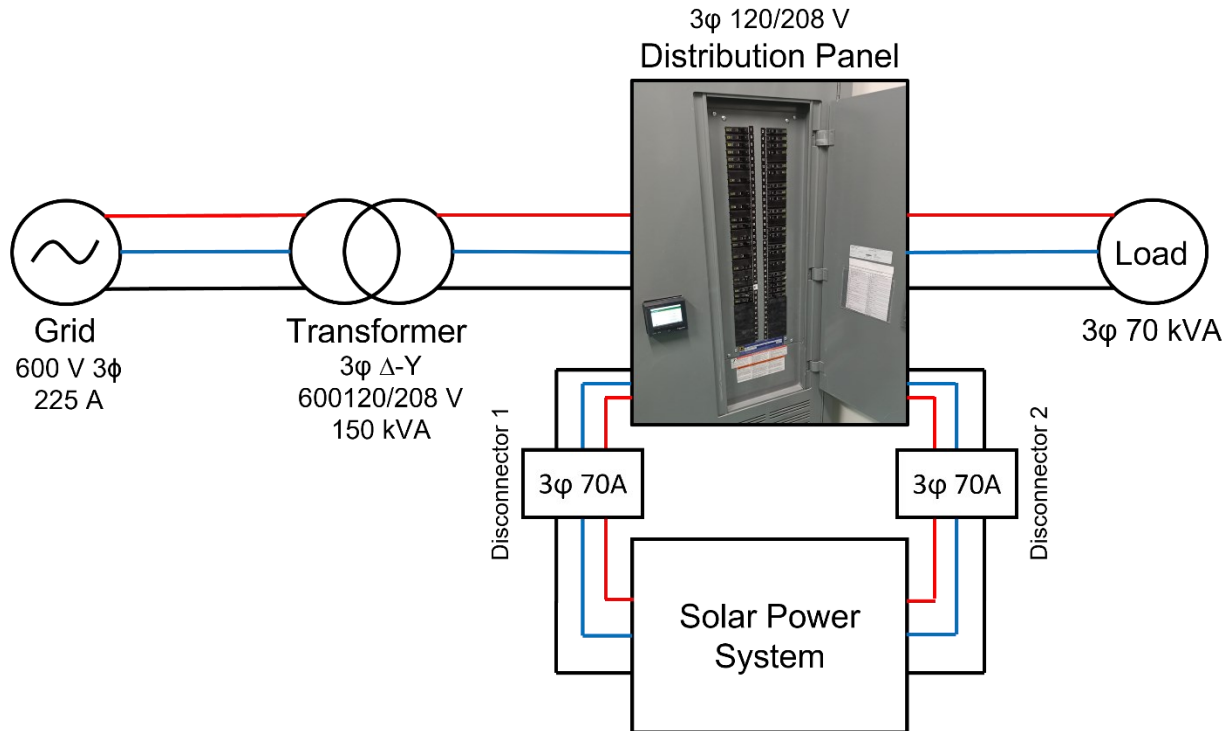
Figure 3.2 Connection of the solar power system to the electrical system of the house.
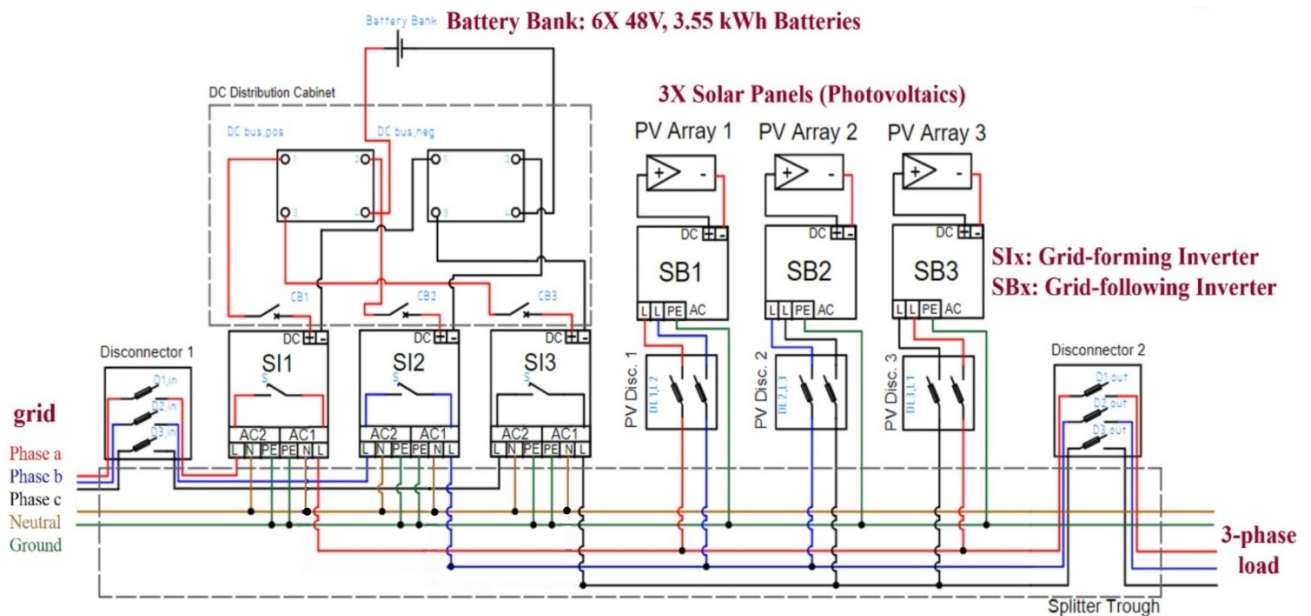
Figure 3.3 The wiring diagram of the solar power system devices.

The system was sized by an electrician and the devices were ordered accordingly. All the modeling procedures are done based on the house's consumption and the specifications of the ordered equipment. The specifications of the commercial devices are brought in Table 3.1.

For research purposes, the modeling is done for different modes of operations, which are explained in the following section.

Table 3.1 Characteristics of the commercial devices of the solar power system.

Device Name and Brand	Characteristics	
Grid-forming inverter[1] *SMA Sunny Island 6048-US*	*Input* (Rectifier Mode)	AC: 120 V/60 Hz, 56 A
	Output (Inverter Mode)	AC: 120 V/60 Hz, 48 A
	Battery-side	DC: 48 V, 110 A
	Power	5.7 kW
Grid-following inverter *SMA Sunny Boy 7.0-US SB7.0-1SP-US-41*	*Input*	DC: 600 V, 10 A (maximum)
	Maximum Power Point (MPP) range	100 - 550 V
	Rated input	245 - 480 V
	Output	AC: 208 V/60 Hz, 32 A
	Power	PV-side input: 11.2 kW (maximum), Grid-side output: 6.6 kW at 208 V, and 7 kW at 240 V
Battery *Pylontech - US3000C LiFePO4*	*Voltage*	44.5-53.5 V, 48 V (nominal)
	Current (charge/discharge)[2]	74 A (maximum), 37 A recommended
	Capacity	3.55 kWh

---

1 Based on the modes of operation explained in section 3.3, the Sunny Island converter can operate in inverter or rectifier modes. Therefore, the grid-side AC connection can either be the input or the output of the converter.

[2] According to the data provided by the manufacturer, the recommended charge/discharge current of the battery is 37 A [49]. This information is used in section 3.3 for designing the controllers.

3.3 Modes of operation

The system under study has different modes of operation at any given time based on the status of the grid, the availability of the power from PV panels, the state of charge of the storage, and the connected loads. Out of all possible modes of operation, three modes are selected. These modes are as follows.

1) Grid feeds the load.
2) Grid charges the battery.
3) Battery feeds the load.

The three mentioned modes are designed in a very straightforward model based on the characteristics of the system and the involved devices. These designs are then simulated in PSIM, and the results of each mode are presented.

3.3.1 Mode 1: grid feeds the load

In this mode, the grid is available and works properly. The house has a fair amount of load to be fed. The grid input comes from Montréal's network. The transformer is physically available in the house and is simulated with the same characteristics. The secondary of the transformer is connected to an RL load that represents the house loads.

3.3.1.1 Circuit design

All the parameters are selected based on the characteristics of the grid and transformer. The load is assumed to be an RL load with a 0.8 power factor (PF), and the values are derived below.

$$S_{load-3\varphi} = 70 \text{ kVA} \tag{3.1}$$

$$S_{load-per-phase} = \frac{70}{3} = 23.3 \text{ kVA} \tag{3.2}$$

$$V_{load-per-phase} = 120 \text{ V} \rightarrow I_{load-per-phase} = \frac{23.\overline{3}}{120} = 194.4 \text{ A} \tag{3.3}$$

$$PF_{load} = 0.8 = \cos\varphi \rightarrow \varphi = 36.86° \tag{3.4}$$

$$Z = R + j\omega L = |Z|e^{j\varphi} \tag{3.5}$$

$$|Z|e^{j\varphi} = \frac{V}{Ie^{-j\varphi}} = \frac{120}{194.4e^{-j36.86}} = 0.61e^{j36.86} \tag{3.6}$$

$$Z = R + j\omega L = 0.49 + j0.37 \rightarrow R = 0.49 \text{ }\Omega \tag{3.7}$$

$$\omega = 2\pi f, f = 60 \text{ Hz} \rightarrow L = 980 \text{ μH}, \tag{3.8}$$

where $S_{\text{load-3}\varphi}$ is the three-phase apparent power of the load, $S_{\text{load-per-phase}}$ is the per-phase apparent power of the load, $V_{\text{load-per-phase}}$ is the per-phase load voltage, $I_{\text{load-per-phase}}$ is the per-phase load current, PF_{load} is the load power factor, φ is the angle between the load voltage and the load current, Z is the impedance of the Load, R is the resistance of the load, L is the inductance of the load, ω is the grid angular frequency, and f is the grid frequency.

Table 3.2 shows the parameters of the system in this mode.

3.3.1.2 Simulation

The simulation is done in three phases as in Figure 3.4. The power direction is from the grid to the load. The results of this simulation are brought in the following subsection.

Table 3.2 System characteristics for the operating mode 1.

Grid input	600 V/60 Hz, 225 A maximum
Transformer	150 kVA, 600-208Y120 V/60 Hz
Load	3-phase Y-connected RL Load R=0.49 Ω, L=980 μH, PF=0.8
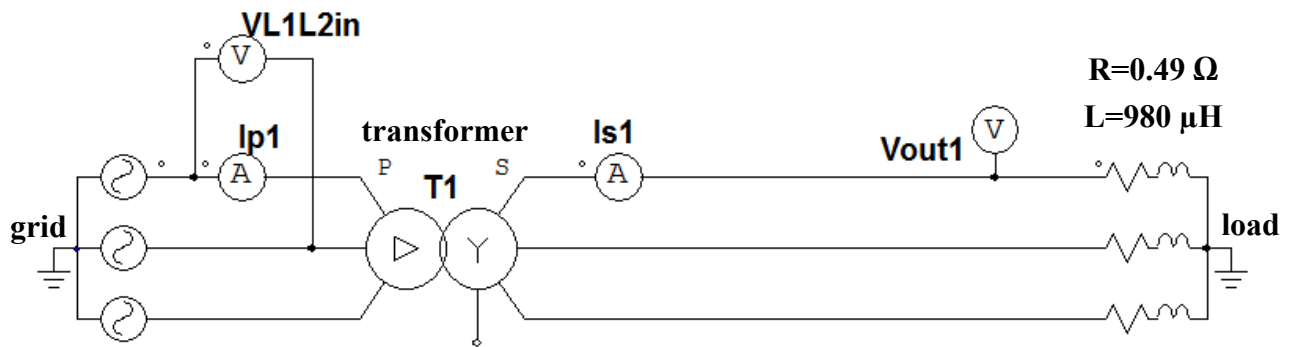
Figure 3.4 Time domain simulation of operating mode 1; The power is sent from the grid on the left to the load on the right. The load and the grid are connected by a transformer.

The measurements are done for the transformer primary line current, I_{p1}, transformer primary line-to-line voltage, $V_{L1L2\text{in}}$, transformer secondary line current, I_{s1}, and transformer secondary phase voltage, V_{out1}.

3.3.1.3 Results

The waveforms of the currents and voltages are shown in Figures 3.5 and 3.6. The parameters derived from the waveforms are shown in Table 3.3. The power balance on both sides of the circuit is checked as follows. The efficiency is 96 %.

$$I_{p1} \times \frac{V_{L1L2in}}{\sqrt{3}} = 70 \times \frac{600}{\sqrt{3}} = 24.3 \text{ kVA} \qquad ; I \tag{3.9}$$

$$I_{s1} \times V_{out1} = 195 \times 120 = 23.4 \text{ kVA} \qquad ; II \tag{3.10}$$

$$\therefore \quad I \cong II \tag{3.11}$$
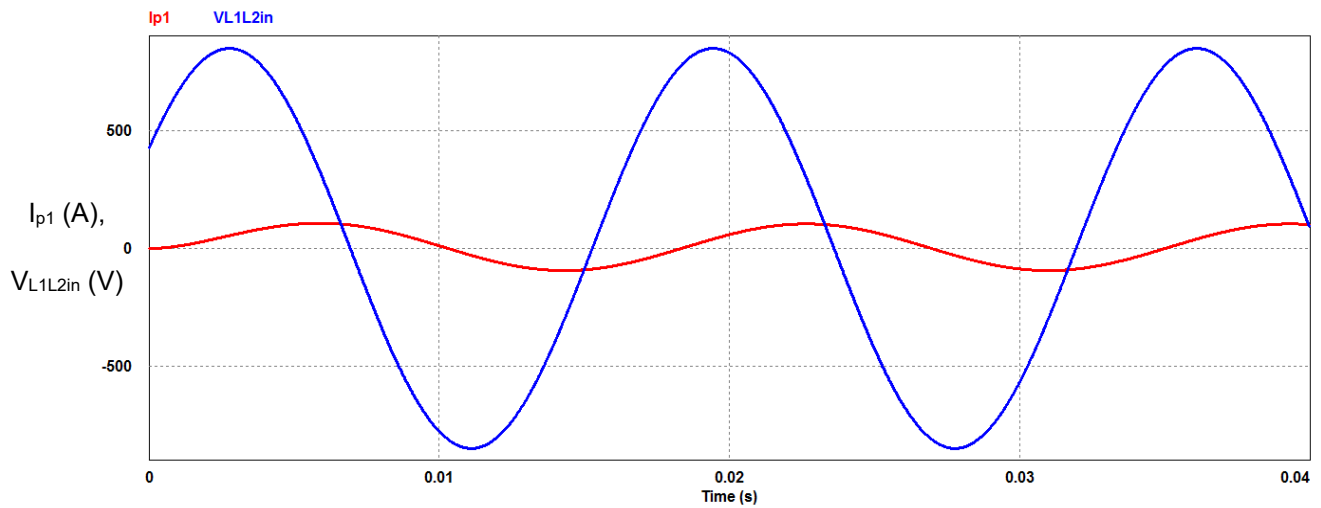
Figure 3.5 Simulation result of mode 1; red trace is the transformer's primary line current, and the blue trace is the transformer's primary line-to-line voltage.
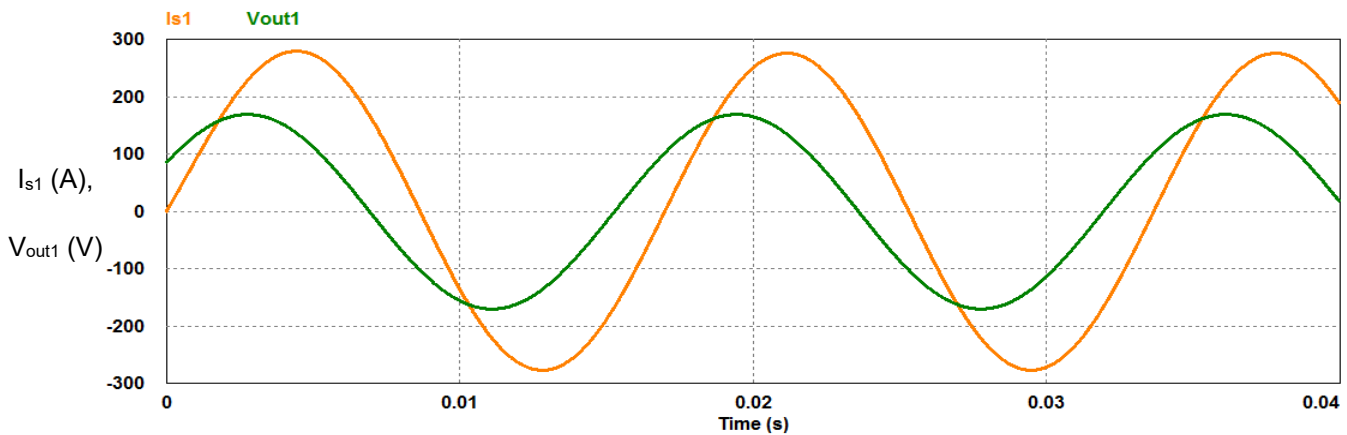
Figure 3.6 Simulation result of mode 1; orange trace is the transformer's secondary line current, green trace is the transformer's secondary phase voltage.

19

Table 3.3 Summary of system parameters of mode 1 from simulation.

I_{p1}	70 A RMS
V_{L1L2in}	600 V RMS
I_{s1}	195 A RMS
V_{out1}	120 V RMS
PF	0.8

3.3.2 Mode 2: grid charges the battery

In this mode, the grid is available and is used for charging the battery. The batteries are connected to the grid via Sunny Island[3] inverters, each for one phase of the grid, in the real setup. Sunny Island inverters can send power in both directions, from the grid to the battery and from the battery to the load.

3.3.2.1 Circuit design

The selected topology is as mentioned in section 2.7 with a difference in the control method so that the converter can work in the opposite direction. For this mode, since the power is sent from the grid (an AC source) to the battery (a DC load), the voltage needs to be converter from AC to DC. The conversion is done by a Front-End Active Rectifier (FEAR) or a switch-mode H-bridge converter. It is switched and/or controlled according to the direction of power. At the output of the rectifier, a DC voltage will be created that is much higher than the voltage of the battery. Therefore, the DC/DC converter is working as a buck converter to step-down the rectified voltage to the battery voltage level. The control of the charging/discharging current of the battery is of high importance as the battery can only tolerate a specific range of current.

In the process of the design, it is important to make sure that the converters are bidirectional. The FEAR is a rectifier and can also work as an inverter if switched accordingly. The DC/DC converter is designed as a bidirectional buck-boost converter to ensure a bidirectional power flow. The schematic diagram of this converter is shown in Figure 3.7. The right side is where the battery is connected, and on the left side, the FEAR will be connected. The output capacitor of the boost converter is the DC-link of the two stages. The DC-link voltage is considered to be 200 V in all

---

[3] Refer to Table 3.1.

modes so that the grid voltage could be easily created at the PCC without the need for a step-up transformer in inverter mode. This converter is switched based on the operating mode. The design process is as follows.
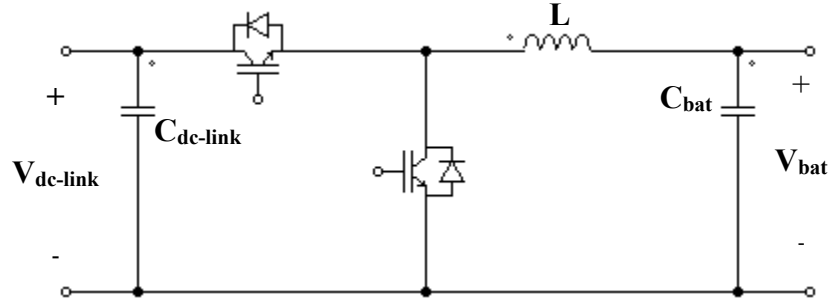
Figure 3.7 Bidirectional DC/DC buck-boost converter.

Buck converter design

$$d = \frac{V_{bat}}{V_{dc-link}} \tag{3.12}$$

$$V_{dc-link} = 200 \text{ V}, V_{bat} = 44.5 - 53.5 \text{ V} \rightarrow 0.22 \leq d \leq 0.26 \tag{3.13}$$

$$I_L = 37 \text{ A}, \Delta V_{bat} = 2\%, \Delta I_L = 2\% \tag{3.14}$$

$$L_{min} \geq \frac{V_{bat}(1-d)}{\Delta I_L f_s} \rightarrow L_{min} \geq 2.5 \text{ mH} \tag{3.15}$$

$$C_{bat} = \frac{\Delta I}{8 f_s \Delta V_{bat}} \rightarrow C_{bat} = 10 \text{ μF}. \tag{3.16}$$

Boost converter design

$$d = 1 - \frac{V_{bat}}{V_{dc-link}} \tag{3.17}$$

$$V_{bat} = 44.5 - 53.5 \text{ V}, V_{dc-link} = 200 \text{ V} \rightarrow 0.73 \leq d \leq 0.77 \tag{3.18}$$

$$I_L = 37 \text{ A}, \Delta V_{dc-link} = 2\%, \Delta I_L = 2\% \tag{3.19}$$

$$L_{min} \geq \frac{d(1-d)V_{dc-link}}{f_s \Delta I_L} \rightarrow L_{min} \geq 2.5 \text{ mH} \tag{3.20}$$

$$C_{dc-link-min} \geq \frac{I_L d}{f_s \Delta V_{dc-link}} \rightarrow C_{dc-link-min} \geq 350 \text{ μF}, \tag{3.21}$$

where d is the DC/DC converter duty-cycle, $V_{dc\text{-}link}$ is the DC-link voltage, V_{bat} is the battery voltage, I_L is the inductor current, L_{min} is the minimum inductance of the converter, C_{bat} is the battery-side capacitor, $C_{dc\text{-}link\text{-}min}$ is the minimum DC-link capacitor, and f_s is the switching frequency.

The DC/DC converter is also working as a charge controller for the battery. The calculation for the minimum values of the DC/DC converter's parameters are done based on the 2% ripple of the inductor current and capacitors' voltages. For the simulation, to decrease the ripple to almost 1%, values of 2 times the inductance and battery-side capacitor are selected. By getting the initial results of the converter, it was observed that the capacity of the dc-link is not enough for the stability of the 200 V dc-link as desired, and it was selected to be 5 mF by trial and error. The selected values for the inductor, the battery side capacitor, and the DC-link capacitor are shown in Table 3.4.

Table 3.4 Bidirectional DC/DC buck-boost converter's parameters.

L	5 mH
C$_{bat}$	21 µF
C$_{dc\text{-}link}$	5 mF

To design the grid inductance, it is assumed that it has a 0.05 Ω resistance, and then the inductance is calculated to be 1.2 mH based on the allowable current ripple as shown in (3.26). The power is sent from one AC source (V_{grid}) to another AC source (V_{conv}). V_{conv} is the voltage created between the middle of the two legs of the H-bridge converter as shown in Figure 3.8.
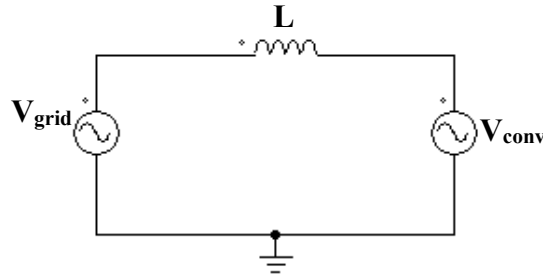
Figure 3.8 Sending power between two AC sources.

Assuming P = 10 kW at most, and

$$V_{grid} = 120 \text{ V RMS}, 60 \text{ Hz}, \tag{3.22}$$

then,

$$I = 83.3 \text{ A RMS. Assuming 5\% current ripple, then } \Delta I = 4.16 \text{ A}. \tag{3.23}$$

The inductor ripple current can be calculated as follows.

$$V_L = L_{line} \frac{di}{dt} \rightarrow \Delta I = \frac{V_L d T_s}{L_{line}}, T_s = \frac{1}{f_s} \rightarrow \Delta I = \frac{V_L d}{f_s L_{line}} \tag{3.24}$$

$$V_L = 200V \text{ at } dT_s \tag{3.25}$$

$$L_{line} = \frac{V_L}{f_s \Delta I} = \frac{0.5 \times 200}{20000 \times 4.16} = 1.2 \text{ mH}, \tag{3.26}$$

where P is the active power transferred between the two sources, V_{grid} is the grid voltage, I is the inductor current, $V_{dc\text{-}link}$ is the dc-link voltage, T_s is the switching cycle, f_s is the switching frequency, L_{line} is the transmission line inductance, and V_L is the grid inductance voltage.

For the FEAR, a closed-loop control is used to control the voltage across the DC-link capacitor and the current drawn from the grid.

The designed bidirectional AC/DC converter is shown in Figure 3.9.
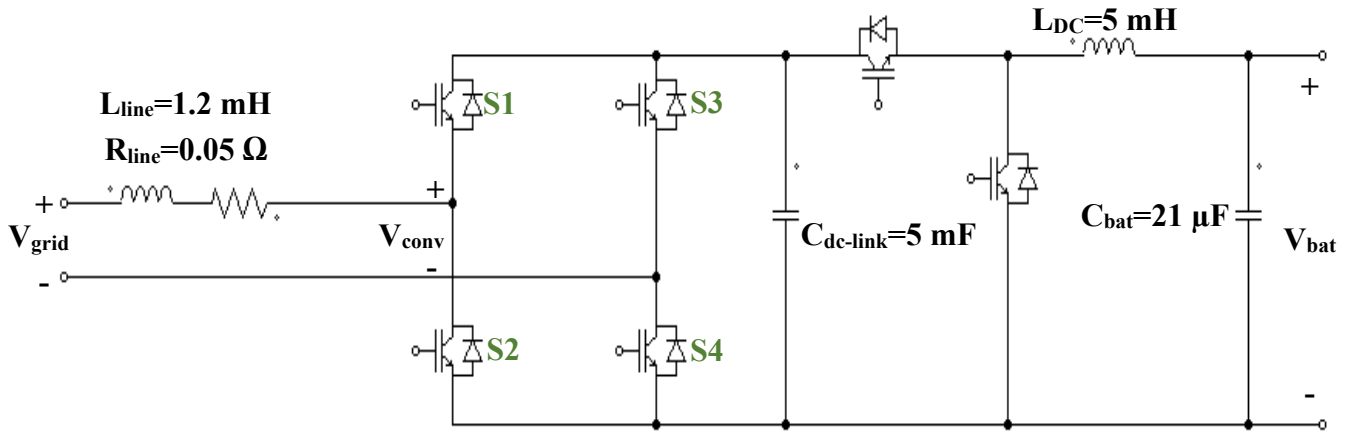
Figure 3.9 Bidirectional AC/DC converter circuit (Sunny Island).

For the battery model, the *Li-Ion Battery* block in PSIM is selected and the values are given to the block based on the characteristics of the commercial battery provided in the datasheet [49]. The values are brought in detail in Table 3.5.

Table 3.5 Values selected for the Li-Ion Battery block in PSIM [49].

Rated Voltage	48 V
Discharge Cut-off Voltage	44.5 V
Rated Capacity	70.29 Ah
Internal Resistance	0.05 Ω
Discharge Current	37 A
Full Voltage	53.5 V
Exponential Point Voltage[4]	48.05 V
Nominal Voltage	48 V
Maximum Capacity	74 Ah
Exponential Point Capacity[5]	33
Nominal Capacity	66.67 Ah

3.3.2.2 Controller design

For the FEAR, two cascaded closed-loop controllers are used for control. A hysteresis current controller (HCC) is used in the inner loop to control the grid current [28], and a proportional-integral (PI) controller is used in the outer loop to control the dc-link voltage at the desired level (200 VDC). The block diagram of the controller is shown in Figure 3.10. The DC-link reference voltage (V_{ref}), which is 200 VDC, is compared with the actual DC-link voltage ($V_{dc-link}$). Then, the error is given to a PI controller for compensation, which generates the reference current ($\hat{I}^*$). The amplitude of the reference current is multiplied by the phase of the grid. This makes the power transfer stay in unity power factor (UPF) mode. Then, the sinusoidal reference current (i^*) is compared to the actual grid current (I_{grid}) via a hysteresis current controller (HCC) PWM, which controls the grid current and generates the needed switching signals for the FEAR. The selected values for the PI controller of DC-link voltage are brought in Table 3.6. K_p is the proportional gain and K_i is the integral gain of the PI controller. To control the charging current of the battery, an HCC with the reference current of 37 A and 2 A total band is used for the buck converter.

---

[4] The exponential point voltage is the voltage of the battery at the end of the exponential region when discharging.
[5] The exponential point capacity is the capacity of the battery at the exponential point voltage.
See Figure A.1 in the Appendix for further information.

3.3.2.3 Simulation

The circuit schematic diagram of this mode is shown in Figure 3.11. The same circuit as in Figure 3.9 is used for the converter along with the control technique in Figure 3.10. The rectifier is switched as a boost rectifier to make the 200 V DC-link. The two gating signals generated by the FEAR's HCC are given to the two switches in the first leg of the FEAR. The other two switches of the second leg are kept OFF. Therefore, only the anti-parallel diodes are used in the second leg to make a path for the current during positive/negative input voltage and/or increasing/decreasing inductor current. All the possible conditions are as below.

1) Positive input voltage
   a. Increasing current→S2 and D4
   b. Decreasing current→D1 and D4
2) Negative input voltage[6]
   a. Increasing current→S1 and D3
   b. Decreasing current→D2 and D3
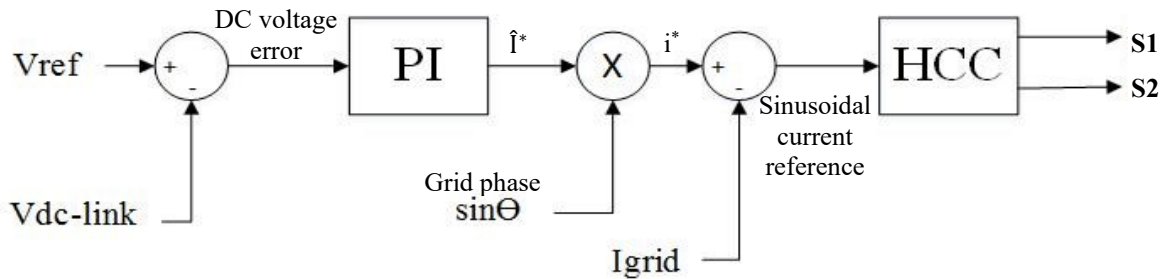
Figure 3.10 Block diagram of the two-loop controller for the FEAR when working as a rectifier.

Table 3.6 PI controller and HCC values for mode 2.

K_p	1
K_i	0.04
HCC band	2 A

---

[6] In this condition, the increase and decrease of the current means the increase in value. The current increases towards negativity and decreases towards positivity.

25

The measurements are done for the grid current, I_{grid}, the grid voltage, V_{grid}, the DC-link voltage, V_{dclink}, the battery charging current, $I_{batcharge}$, the battery voltage, V_{bat}, and the battery state of charge, SOC[7].

3.3.2.4 Results

The results of the time domain simulation of this mode are shown in Figures 3.12 to 3.16. The power balance is checked as in (3.29). The efficiency is 98%. The parameters derived from the waveforms are brought in Table 3.7.

$$I_{grid} \times V_{grid} = 16 \times 120 = 1920 \text{ W} \qquad ; I \qquad (3.27)$$

$$I_{bat} \times V_{bat} = 37 \times 51 = 1887 \text{ W} \qquad ; II \qquad (3.28)$$

$$\therefore I \cong II \qquad (3.29)$$
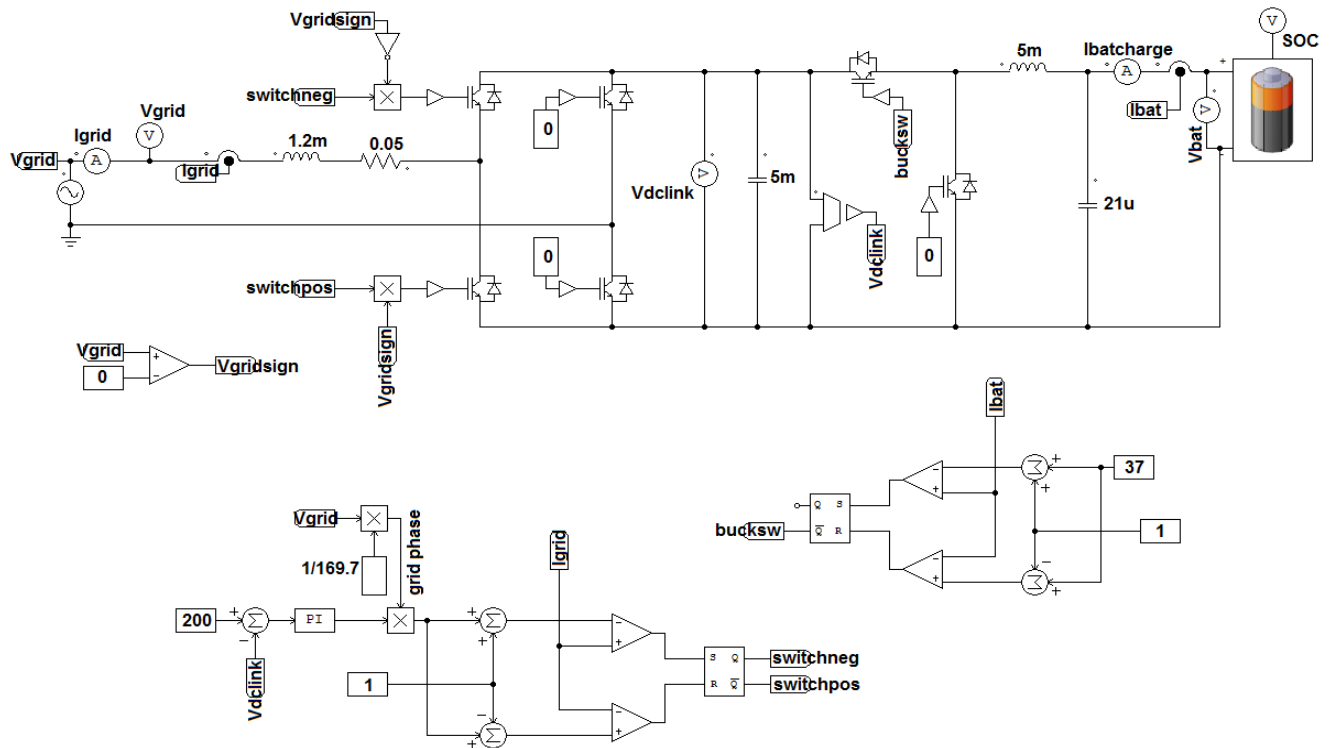
Figure 3.11 Circuit schematic diagram of mode 2; charging the battery from the grid.

---

[7] The state of charge of the battery is usually shown in percentage, 0% as fully discharged and 100% as fully charged. In this thesis, the SOC of 100% is scaled to 1. Therefore, this parameter is unitless in the results demonstrating the battery's SOC.
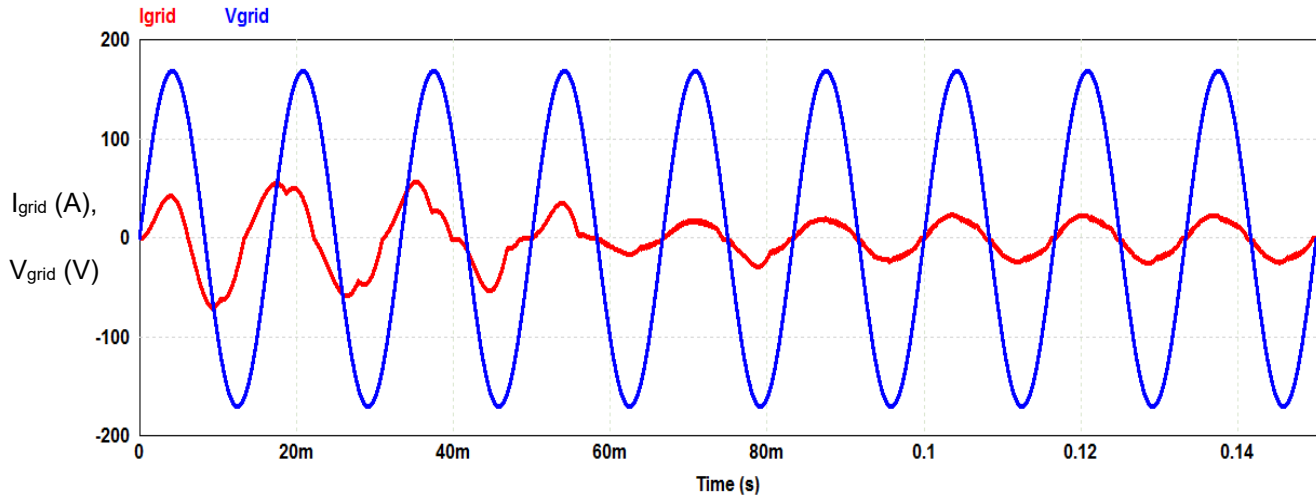
Figure 3.12 Simulation result of mode 2; red trace is the grid current, blue trace is the grid voltage.
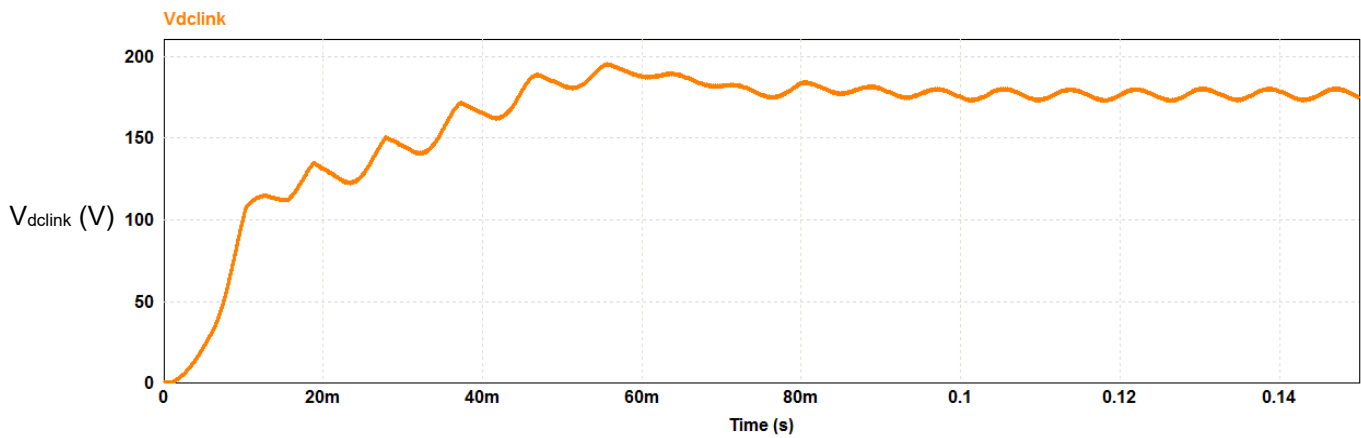
Figure 3.13 Simulation result of mode 2; DC-link voltage.
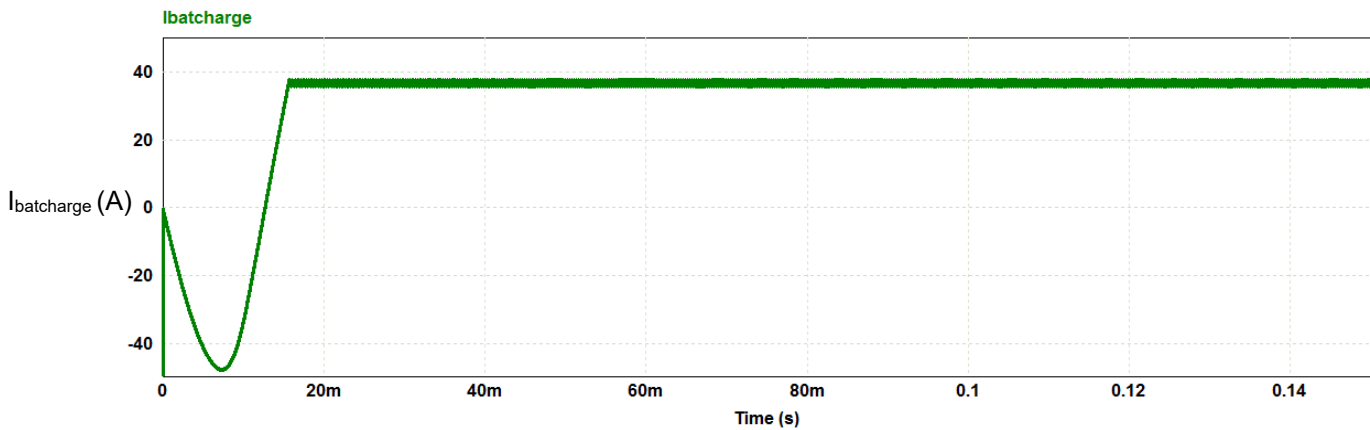
Figure 3.14 Simulation result of mode 2; charging current of the battery.
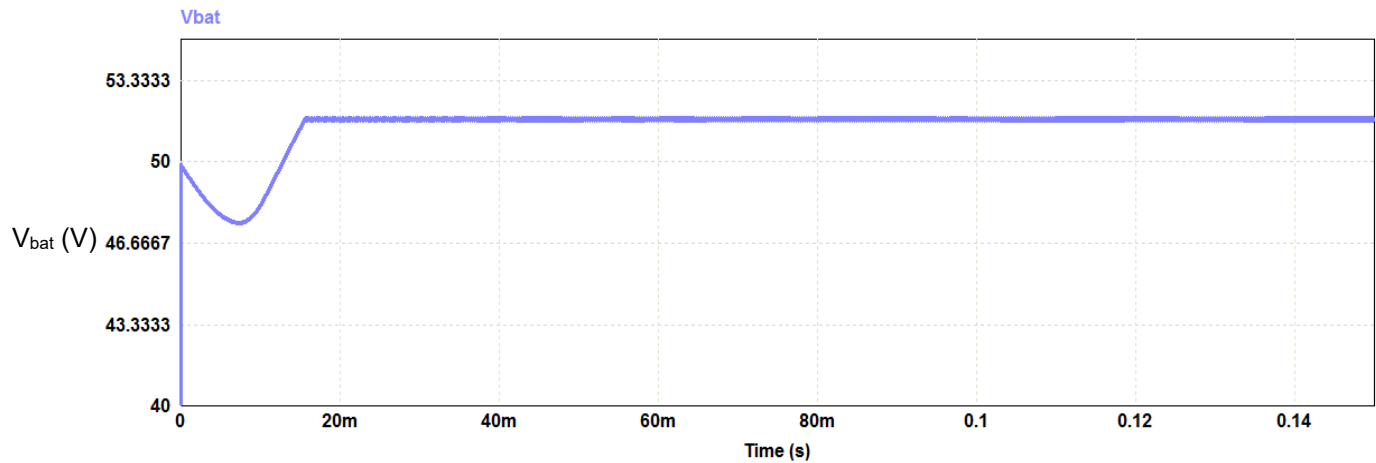
Figure 3.15 Simulation result of mode 2; battery voltage.
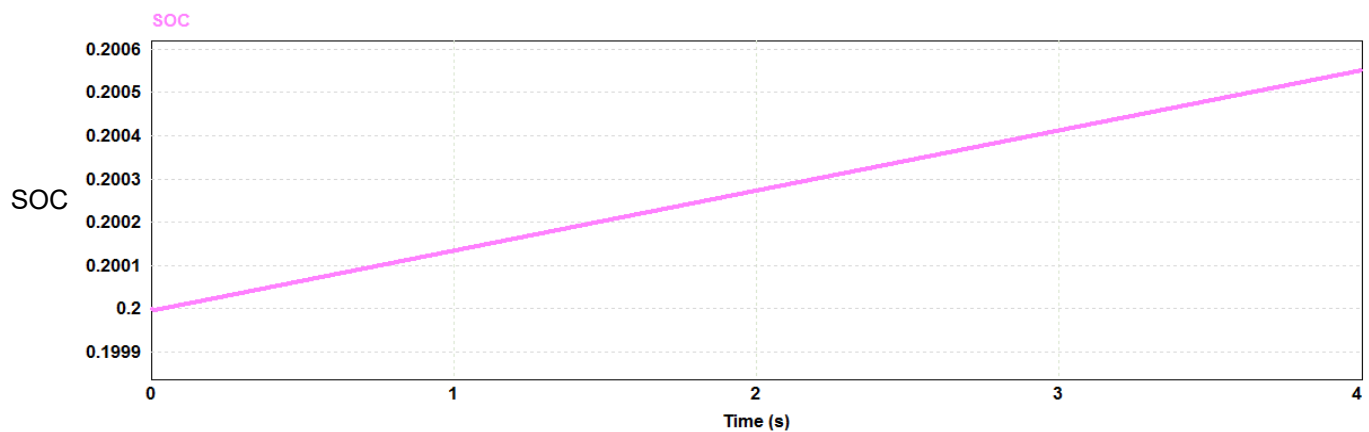
Figure 3.16 Simulation result of mode 2; state of the charge (SOC) of the battery in the first 4 seconds of simulation. The increasing trend is observed.

Table 3.7 Obtained parameters from simulation of operating mode 2.

V_{grid}	120 V RMS
I_{grid}	16 A RMS
	Settles at 0.1 s
	11% ripple
V_{dclink}	180 V
	3% ripple
$I_{batcharge}$	37 A
	5% ripple
V_{bat}	51 V

	<1% ripple
SOC	Increasing

Figure 3.12 shows that a small tolerance band (1 in this case) in the HCC gives a smoother closer-to-reference grid current, but at the same time, it will increase the switching frequency which results in more losses. The result of this phenomenon can be seen in Figure 3.13 in which the DC-link voltage has not reached the 200 V desired level. To settle at this level, more power should be drawn from the grid to compensate the losses caused by the HCC.

3.3.2.5 Transfer functions

As seen from the simulated results, the values are not completely following the references, especially the DC-link voltage. A frequency-domain/mathematical modeling is done to obtain the best values and schematic for the control circuit of this mode. The transfer function of the system is derived analytically, then the controller values are calculated accordingly.

In this mode of operation, there are two closed-loop controllers in a cascaded fashion, the input of the system is the reference DC-link voltage ($V_{dc-link}^*$) and the output is the battery voltage.

The block diagram of the inner control loop (grid current control loop) is shown in Figure 3.17. Then, the outer voltage loop is added to the schematic as shown in Figure 3.18.

The mathematical derivation is done in (3.30) and (3.33). Then, both loops are simulated in MATLAB as shown in Figure 3.19. The PI controller parameters are tuned by MATLAB Simulink and the values are brought in Table 3.8. The circuit is simulated with this control technique as shown in Figure 3.20. The results are presented in Figures 3.21 to 3.28.

Current loop

$$\left[\left(\hat{I}_{grid}^* - \hat{I}_{grid}\right) \times \frac{K_{pc}s + K_{ic}}{s} \times \frac{1/V_{dc}}{1+s\tau} \times (-1) + \hat{V}_{grid}\right] \times \frac{1}{L_g s} = \hat{I}_{grid} \tag{3.30}$$

$$V_{dc} = 200 \text{ V}, \hat{V}_{grid} = 169.7 \text{ V}, L_g = 5 \text{ mH} \tag{3.31}$$

$$\tau = \frac{1}{f_s} , f_s = 20 \text{ kHz} \rightarrow \tau = 50 \text{ ms} \tag{3.32}$$

<u>*Voltage loop*</u>

$$(V^*_{dc-link} - V_{dc-link}) \times \frac{K_{pv}s + K_{iv}}{s} \times \frac{\hat{I}_{grid}}{\hat{I}^*_{grid}} \times \frac{\hat{V}_{grid}}{2V_{dc}} \times \frac{1}{C_{dc}s} = V_{dc-link} \qquad (3.33)$$

$$C_{dc} = 5 \text{ mF}, \qquad (3.34)$$

where $\hat{I}^*_{grid}$ is the grid current reference, M.I is the modulation index, $\hat{V}_{conv}$ is the peak value of the voltage between the middle of the two legs of the FEAR, $\hat{V}_{grid}$ is the peak value of the grid voltage, L_g is the transmission line inductance, $\hat{I}_{grid}$ is the peak value of the grid current, $V^*_{dc-link}$ is the reference value of the DC-link voltage, V_{dc} is the DC-link voltage value in steady state, I_{dc} is the FEAR output current at the DC-link, C_{dc} is the DC-link capacitance, $V_{dc-link}$ is the DC-link voltage, K_{pc} is the proportional gain of the current controller, K_{ic} is the integral gain of the current controller, K_{pv} is the proportional gain of the voltage controller, and K_{iv} is the integral gain of the voltage controller. The transmission line resistance is neglected in the controller design.
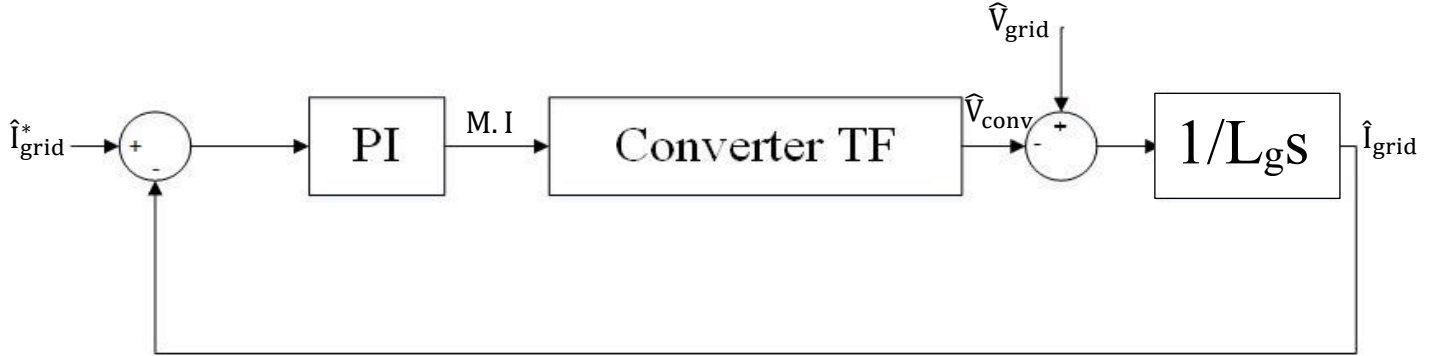
Figure 3.17 Schematic Diagram of the grid current control loop.
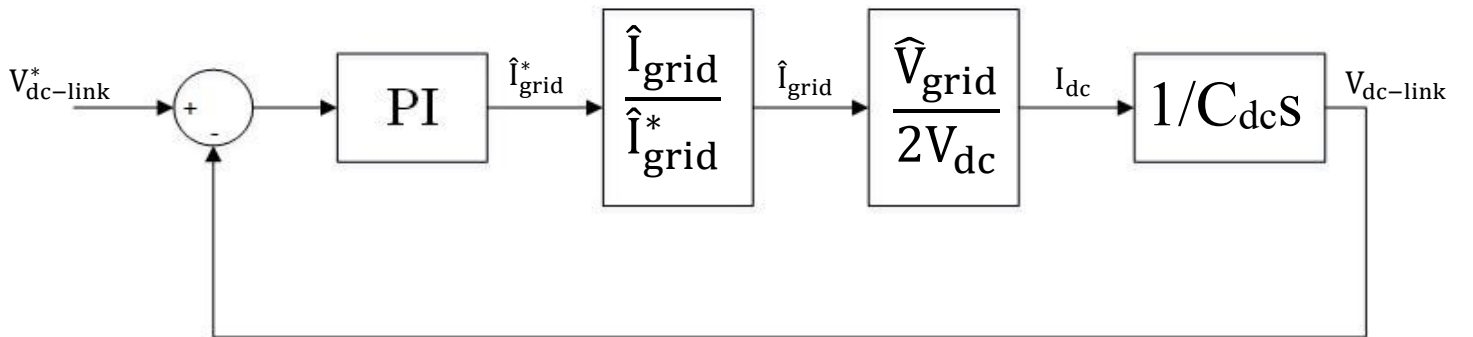
Figure 3.18 Schematic diagram of the DC-link voltage control loop.
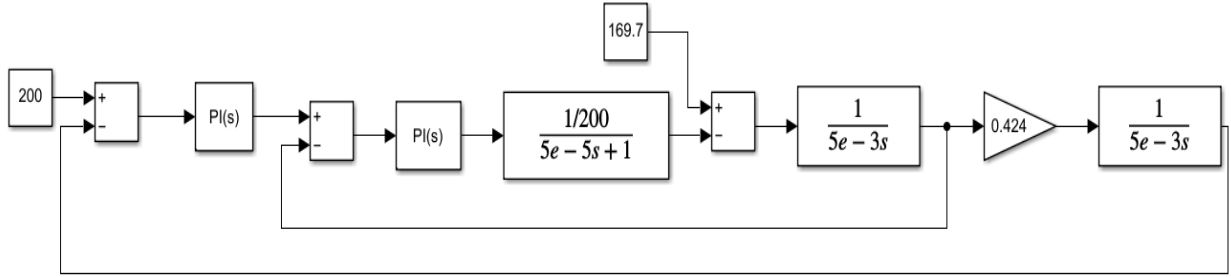
Figure 3.19 Control circuit simulation of the FEAR in mode 2 using Simulink.

Table 3.8 Tuned PI controller parameters using MATLAB.

Current loop	K_{pc}	-1.5
	K_{ic}	1.25×10^4
Voltage loop	K_{pv}	7.5×10^{-3}
	K_{iv}	3.75×10^{-2}

The important values of the simulated results are brought in Table 3.9. The grid inductance is increased to reduce the current surge and ripples. Sunny Island can tolerate a current surge of 180 A for 60 ms, and the simulated results have depicted 113 A peak current for 10 ms as shown in Figure 3.21, which meets the transient specifications of the converter.

The measurements are done for the grid current, I_{grid}, the grid voltage, V_{grid}, the DC-link voltage, V_{dclink}, the battery charge current, $I_{batcharge}$, and the battery state of charge, SOC.

Figures 3.21 to 3.23 show different time segments of the grid voltage and current together for better demonstration as the settling time is relatively high.

Figures 3.24 to 3.26 show the DC-link voltage at different times, showing the transient response and the steady state response.
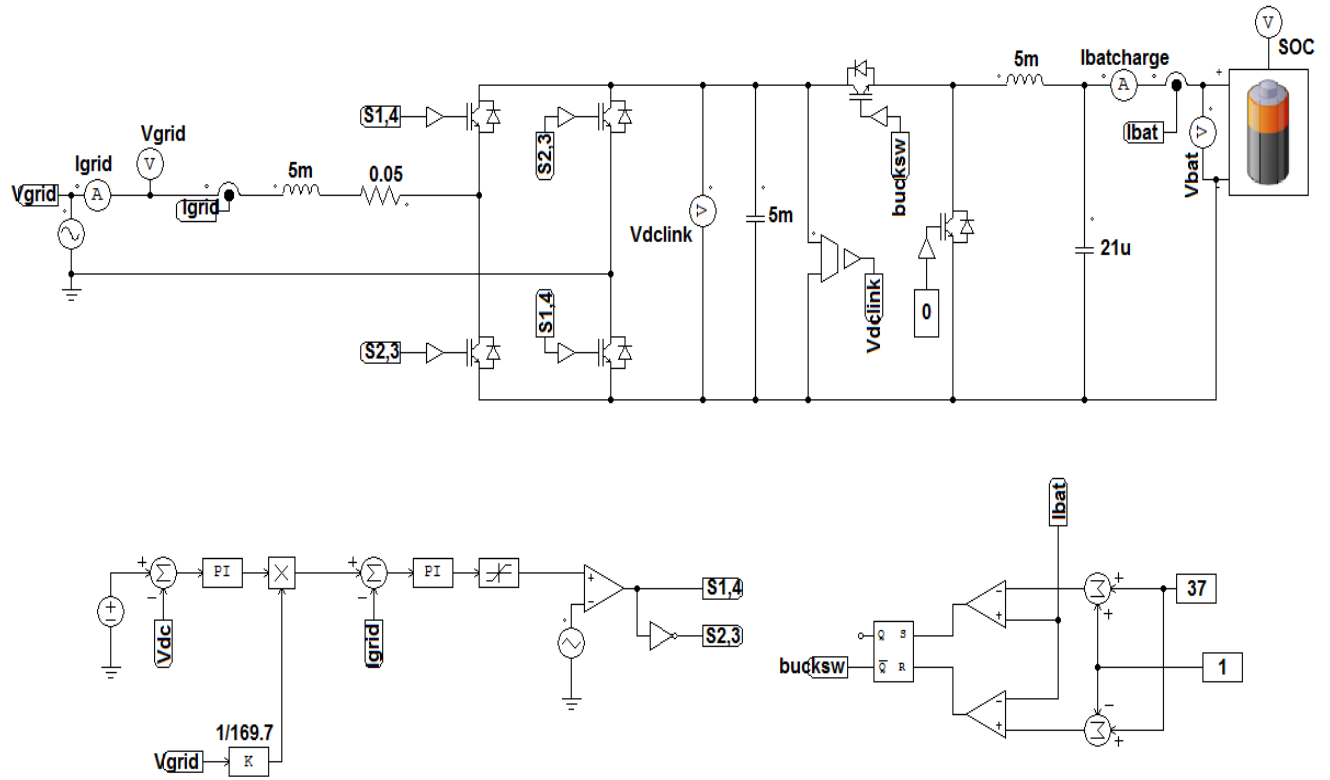
Figure 3.20 Updated circuit schematic diagram of mode 2 using a PI controller for the grid current.
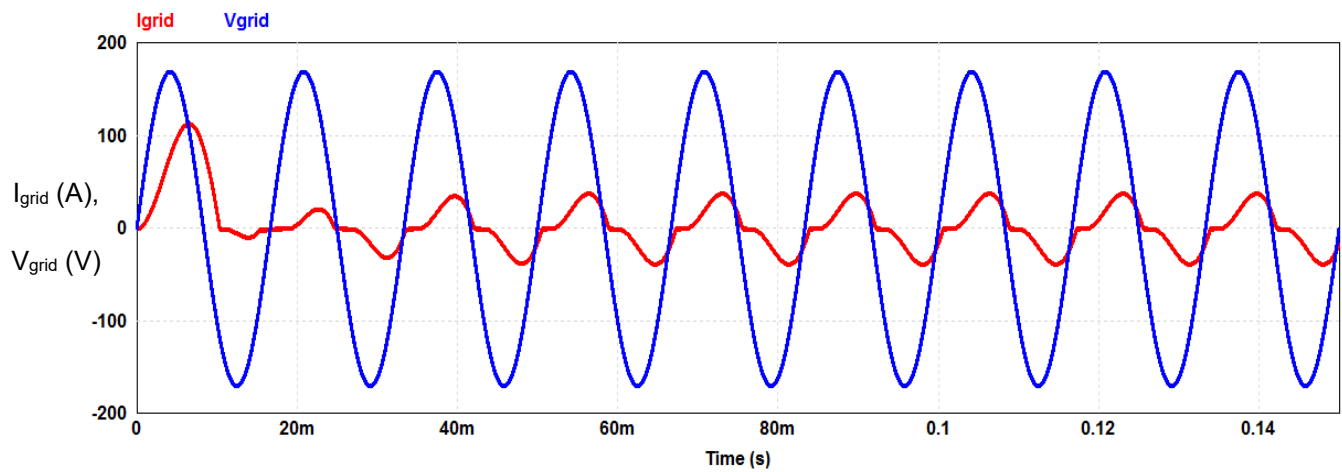
Figure 3.21 Simulation result of mode 2 with two PI controllers; the red trace is the grid current and the blue trace is the grid voltage, and the time segment (1): 0 - 0.15 s.
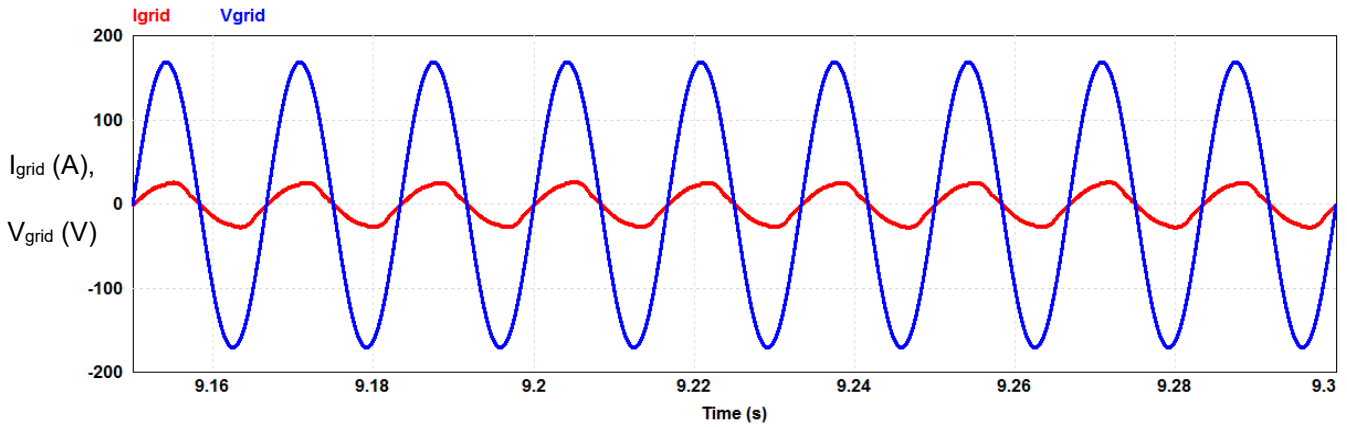
Figure 3.22 Simulation result of mode 2 with two PI controllers; the red trace is the grid current and the blue trace is the grid voltage, and the time segment (2): 9.15 - 9.30 s.
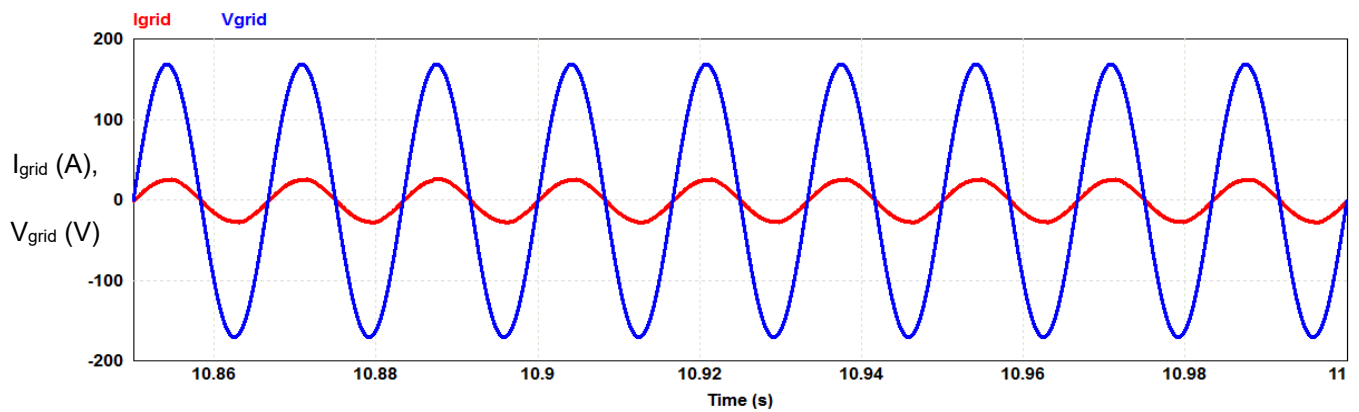
Figure 3.23 Simulation result of mode 2 with two PI controllers; the red trace is the grid current and the blue trace is the grid voltage, and the time segment (3): 10.85 - 11 s.
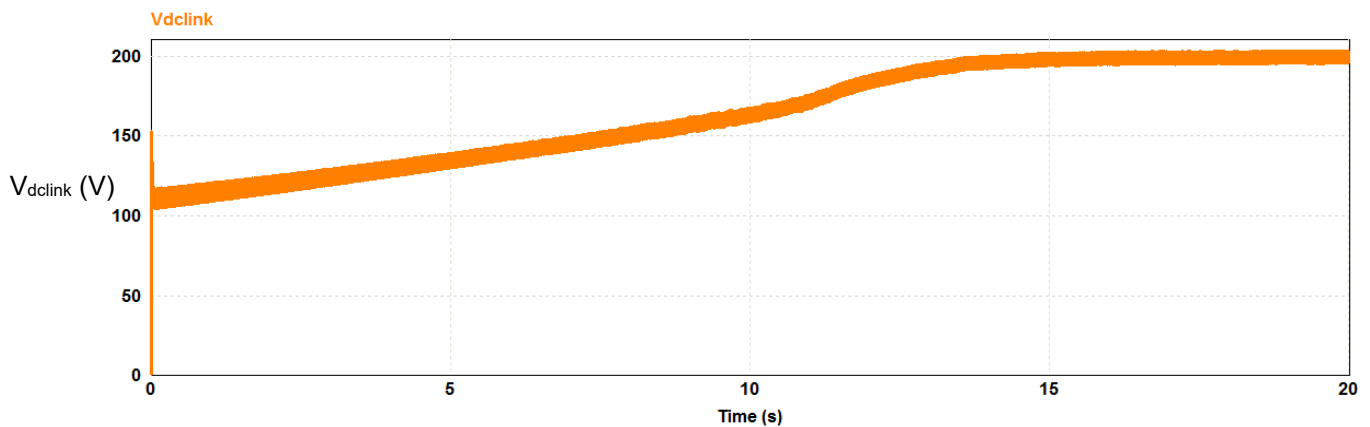
Figure 3.24 Simulation result of mode 2 with two PI controllers; DC-link voltage.

33
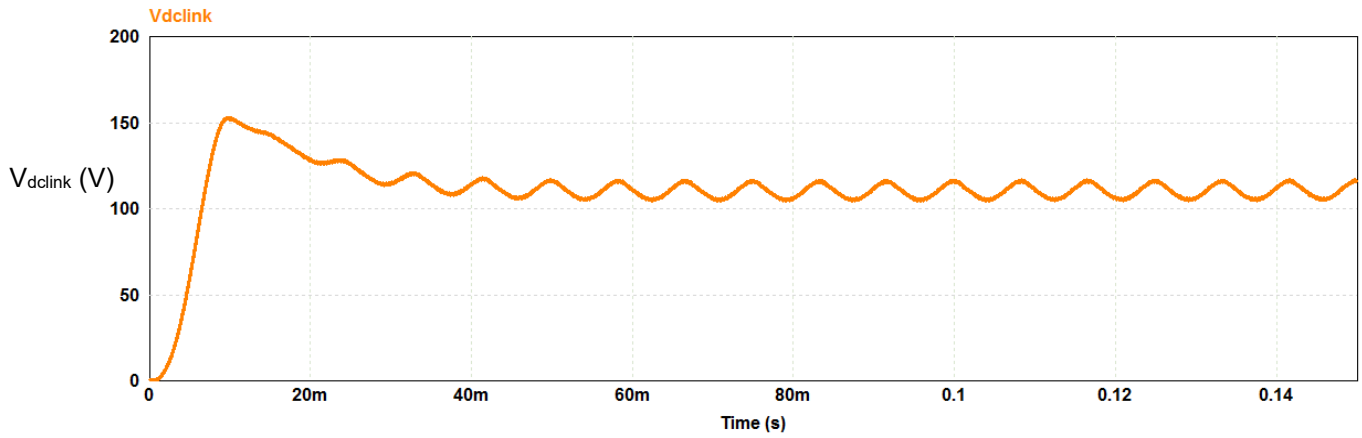
Figure 3.25 Simulation result of mode 2 with two PI controllers; DC-link voltage, and the time segment (1): 0 - 0.15 s.
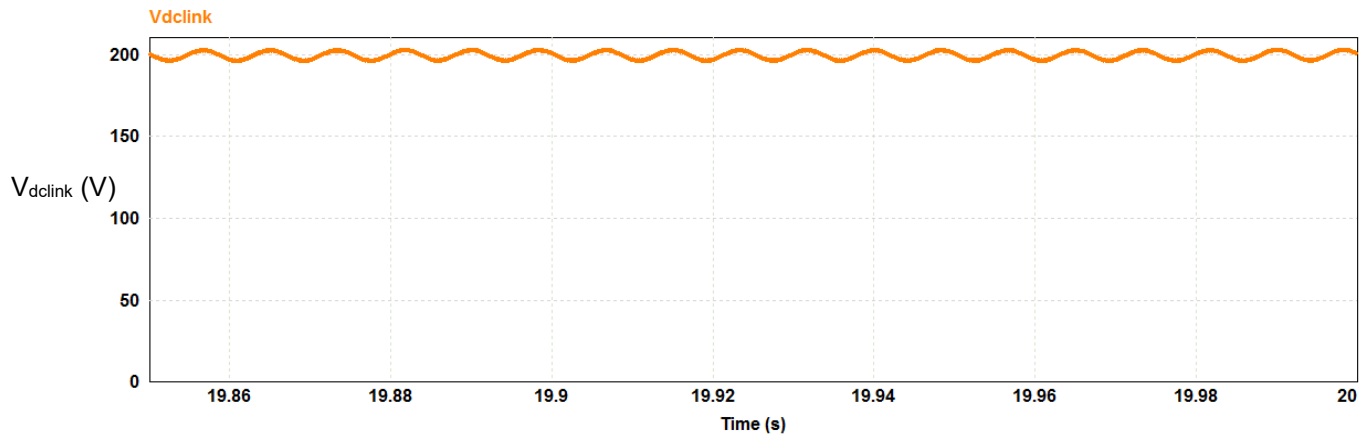
Figure 3.26 Simulation result of mode 2 with two PI controllers; DC-link voltage, and the time segment (2): 19.85 - 20 s.
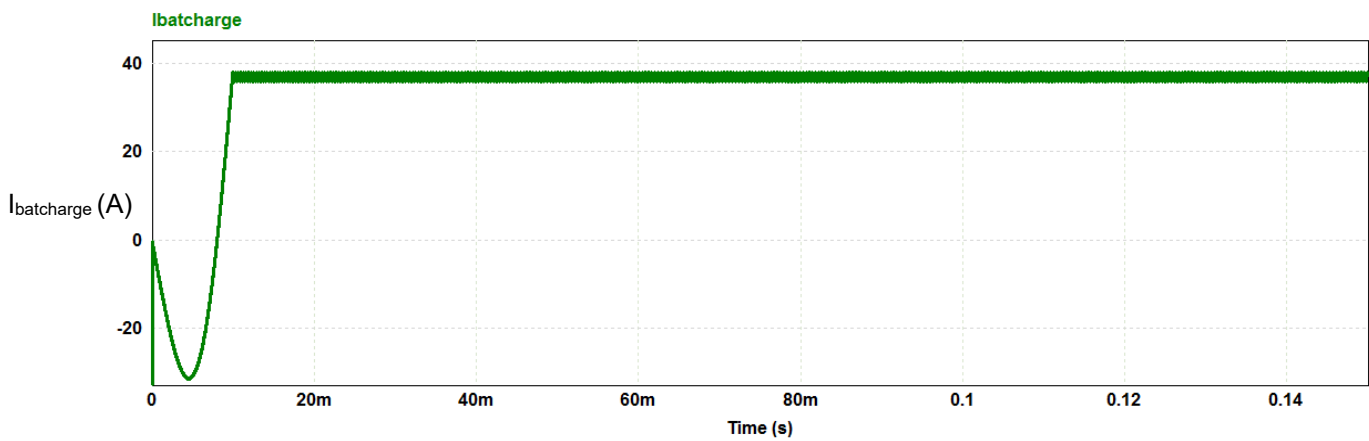
Figure 3.27 Simulation result of mode 2 with two PI controllers; battery charge current.
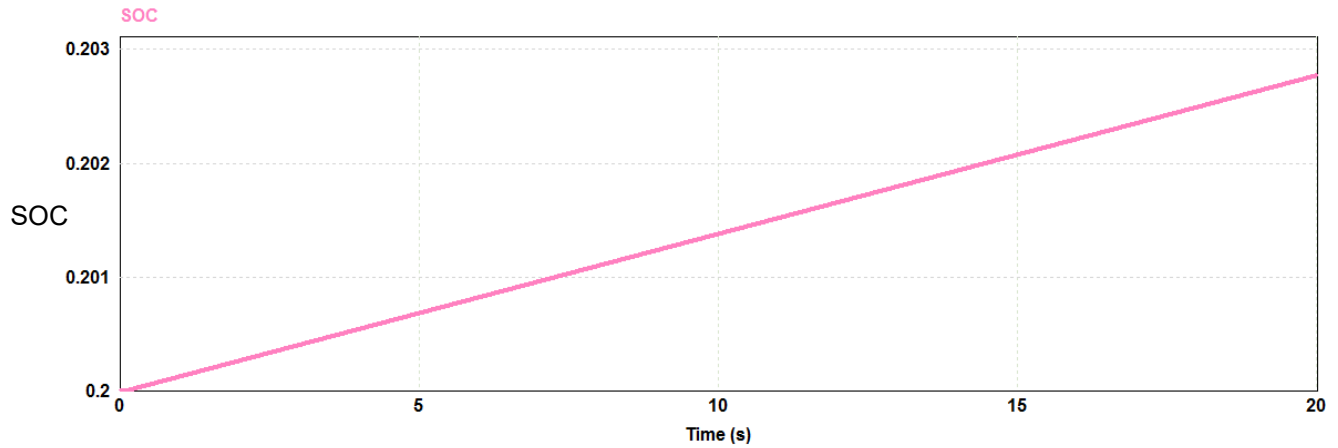
Figure 3.28 Simulation result of mode 2 with two PI controllers; state of the charge (SOC) of the battery.

Table 3.9 Parameters obtained from the updated simulation results of mode 2 simulated with two PI controllers.

V_{grid}	120 V RMS
I_{grid}	19.5 A RMS at steady-state
	Settles at 12 s
	2% ripple
V_{dclink}	200 V
	3% ripple
	Settles at 15 s
$I_{batcharge}$	37 A
	5% ripple
SOC	Increasing

3.3.2.6 Three-phase configuration and results

In the three-phase configuration, each phase of the grid is connected to a single-phase rectifier and altogether they form a three-phase connection to charge the batteries. Instead of a single battery, three batteries (equivalent to a battery stack consisting of three batteries connected in parallel) are used for the three-phase simulation, which keeps the circuit parameters the same for a better demonstration of the results. The schematic circuit diagram is shown in Figure 3.29, and

35

the results are shown in Figures 3.30 to 3.34. The control circuits are the same as in Figure 3.20 for each phase and are not shown in this section.
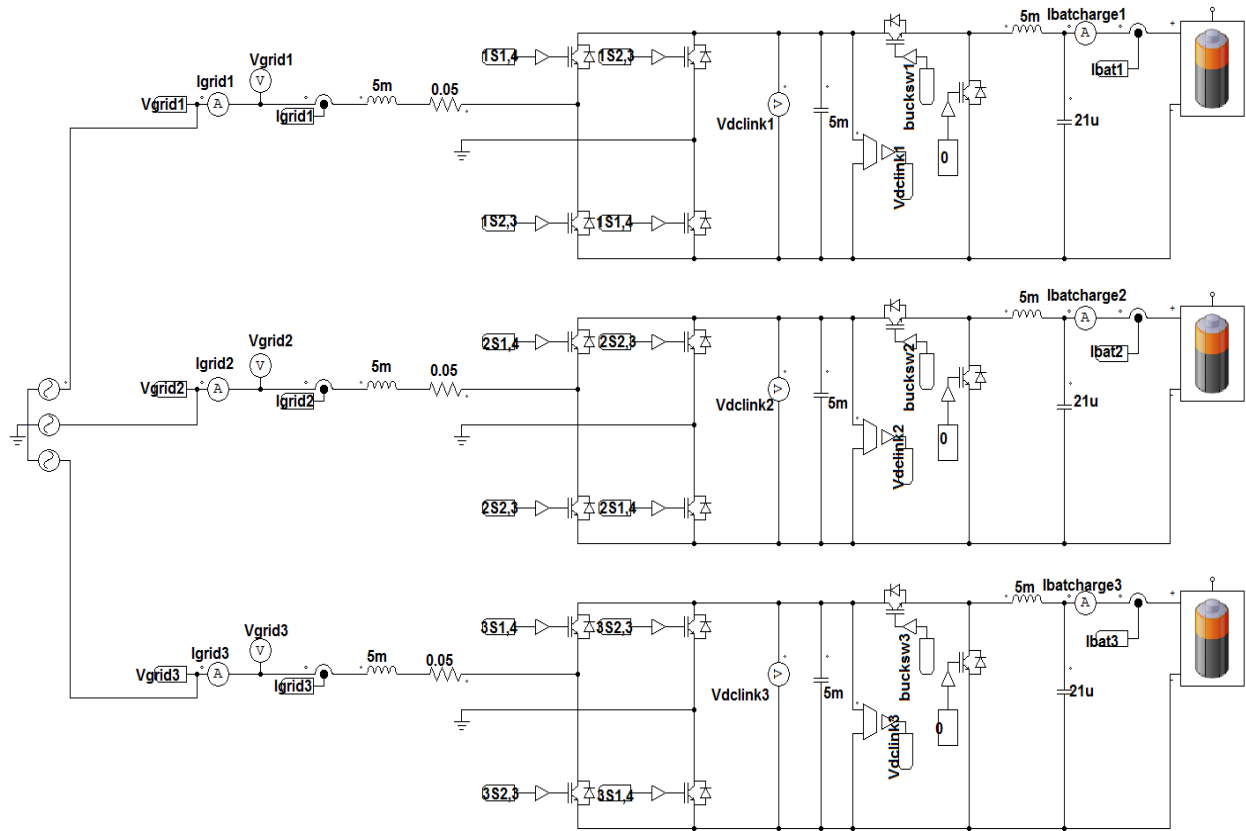
Figure 3.29 Three-phase configuration of mode 2.

The shown simulated results are the per-phase grid current, I_{gridx}, the per-phase grid voltage, V_{gridx}, the per-phase DC-link voltage, $V_{dclinkx}$, and the per-phase battery charge current, $I_{batchargex}$.
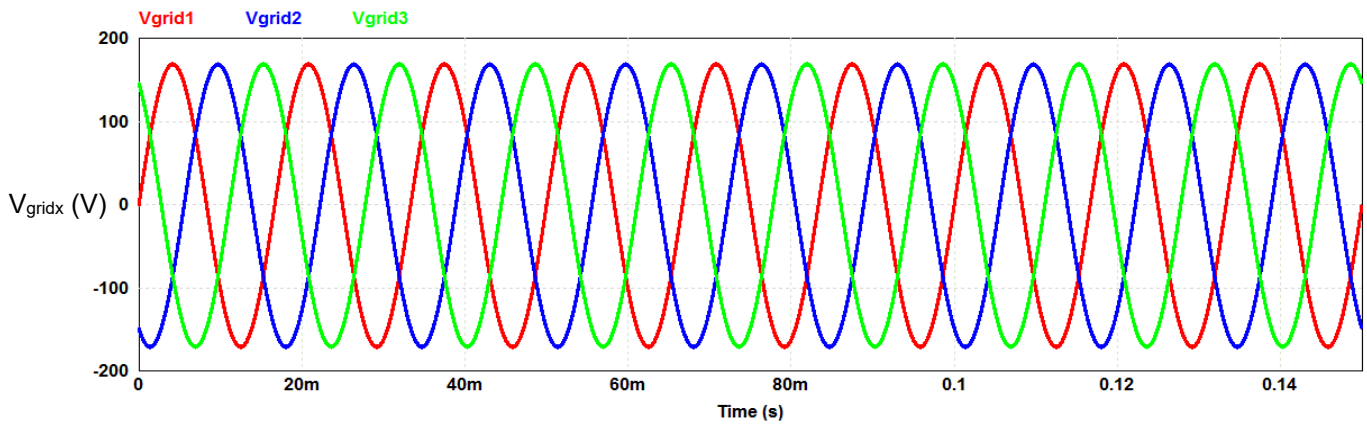
Figure 3.30 Three-phase voltages of the grid in mode 2.
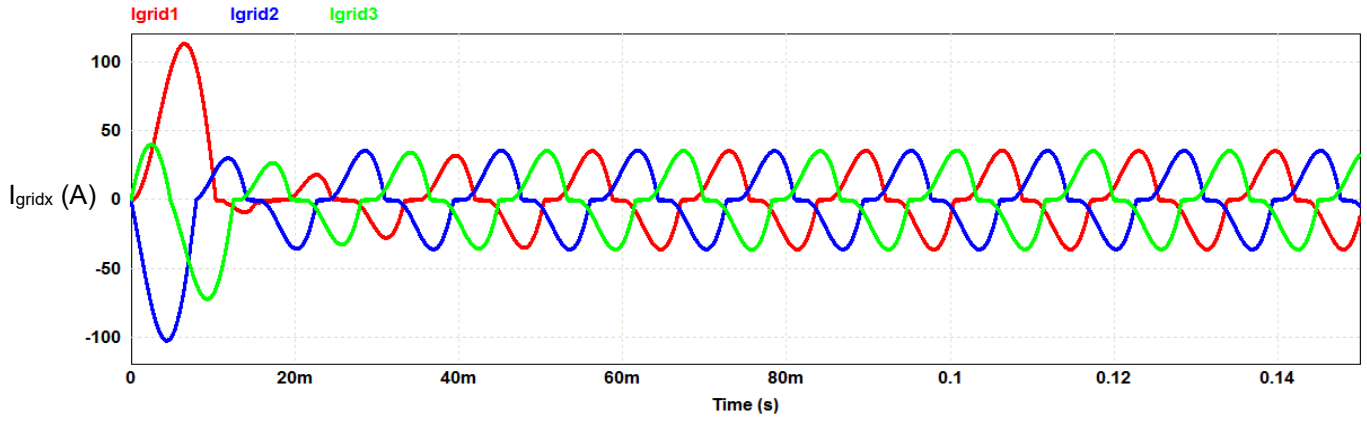
Figure 3.31 Grid three-phase currents in mode 2; transient response.
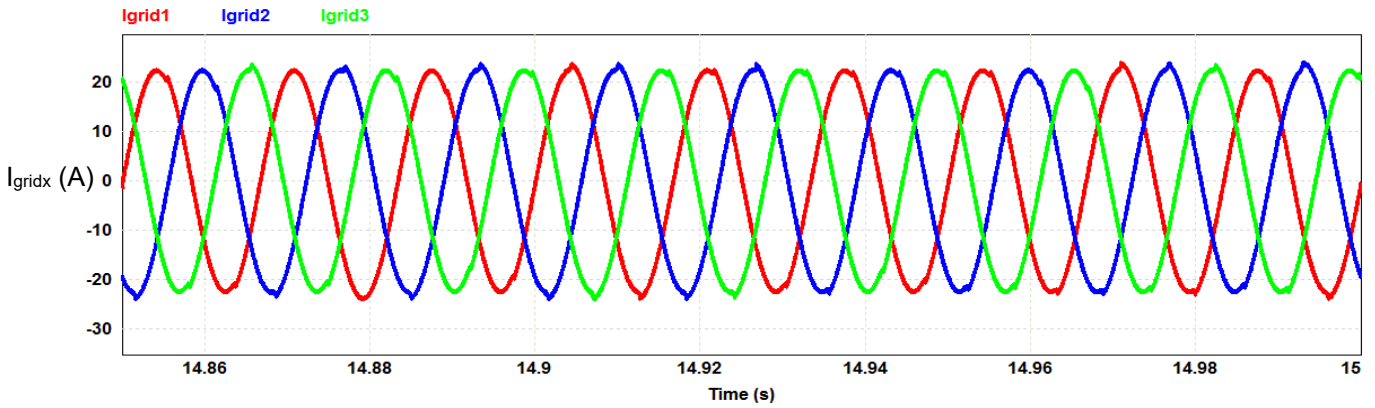
Figure 3.32 Grid three-phase currents in mode 2; steady-state response.
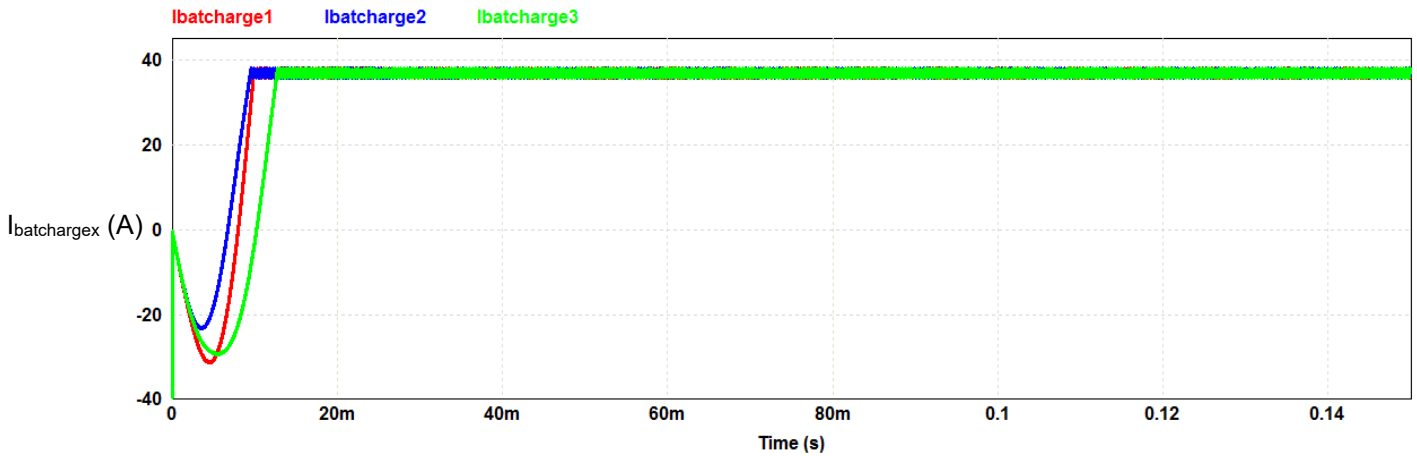
Figure 3.33 Three-phase battery charge current in mode 2.

37
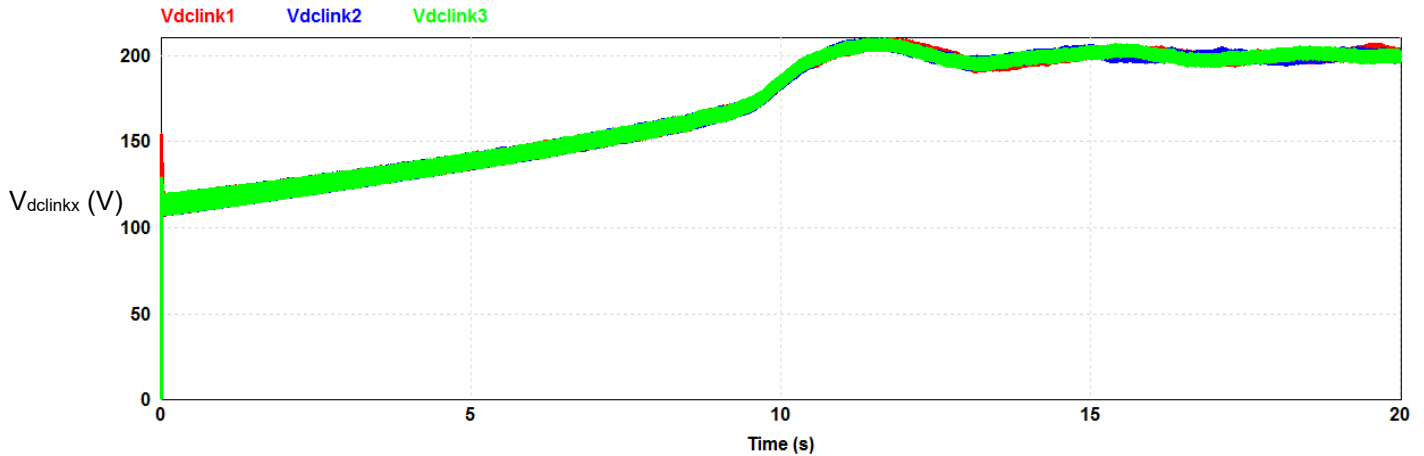
Figure 3.34 Per-phase DC-link voltage in mode 2.

In Figure 3.33, three charging currents are shown, each current represents the charging current of the battery in each phase. In the real configuration, there is a DC bus available, which is the interface between the Sunny Islands and the battery stack. The current drawn from the grid to charge the battery is divided between the three converters.

3.3.3 Mode 3: battery feeds the load

In this mode of operation, the grid has failed and the battery feeds the load. The Sunny Island converter works as a grid-forming inverter and creates a grid-like voltage at the load side.

3.3.3.1 Circuit design

In this mode, the power is sent from the battery to the load. The design of the converter is the same as in Figure 3.9. The only difference is that at the load side, an LC filter is added. Also, the control technique is different as the direction of the power flow is different.

3.3.3.2 Controller design

To have a grid voltage of 120 V at the load side, a DC-link of 200 V is needed. For this, the DC/DC converter needs to work as a boost converter to boost up the battery voltage to 200 V. Therefore, a PI controller is used for the DC/DC converter to keep the DC-link voltage at the desired voltage level. The Sunny Island converter works as an inverter in this mode of operation with an open-loop control fashion using a bipolar SPWM technique. The values of the controllers are in Table 3.10.

The design of the filter inductor is done as in (3.26) and the same value is selected. The calculation for the capacitor is done as in (3.38). After that, a fine tuning is done in order to keep the voltage and current's THDs within the accepted values given by IEEE 519 standard [50]. Based on this, a value of 36 μF is selected for the filter capacitance. The LC filter values are shown in Table 3.11.

$$f_c = \frac{1}{2\pi\sqrt{L_{filt}C_{filt}}} \tag{3.35}$$

$$f_c \leq \frac{f_s}{10}, f_s = 20\ kHz \rightarrow f_c \leq 2\ kHz \tag{3.36}$$

$$L_{filt} = 1.2\ mH \tag{3.37}$$

$$C_{filt} \geq 5\mu F, \tag{3.38}$$

where f_c is the cut-off frequency, f_s is the switching frequency, L_{filt} is the filter inductance, and C_{filt} is the filter capacitance.

3.3.3.3 Simulation

The simulation circuit of mode 3 is shown in Figure 3.35. The parameters selected are the same parameters as in mode 2. An RL load with a power factor of 0.8 is chosen. The load parameters are shown in Table 3.11.

The shown results are the battery voltage V_{bat}, battery discharge current I_{batdis}, DC-link voltage V_{dclink}, load current I_{load}, load voltage V_{load}, and state of charge of the battery SOC.

Table 3.10 Controllers' parameters for the converter in mode 3.

Boost converter PI controller	K_p	1.4×10^{-5}
	K_i	9.4×10^{-4}
Bipolar SPWM	M.I.	0.878
	Modulating signal frequency	60 Hz
	Carrier frequency	20 kHz

Table 3.11 LC filter and load values for mode 3.

LC filter	L_{filt}	1.2 mH
	C_{filt}	36 µF
Load	L_{load}	12 mH
	R_{load}	6.5 Ω
	PF	0.8
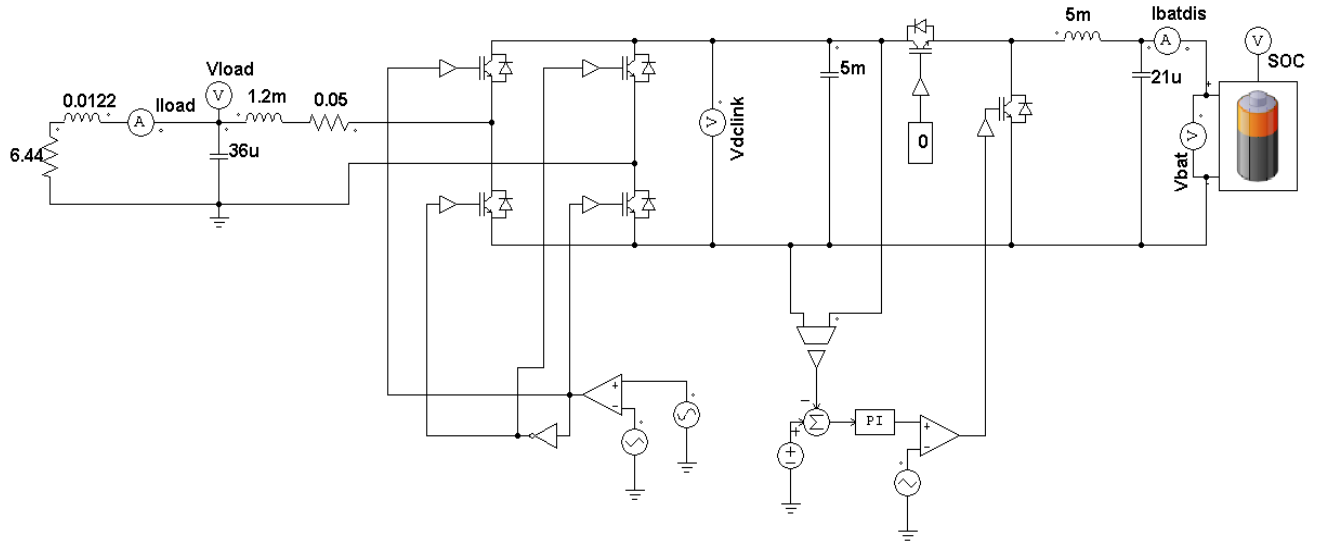
Figure 3.35 Schematic circuit diagram of mode 3. The power flow is from the battery to the load.

3.3.3.4 Results

The simulation results of mode 3 are shown in Figures 3.36 to 3.41. The power balance is checked by (3.39) - (3.41). The efficiency of the system is 96%. The parameters obtained from the simulation results are presented in Table 3.12.

$$I_{bat} \times V_{bat} = 30 \times 50 = 1500 \text{ W} \quad ; I \tag{3.39}$$

$$I_{load} \times V_{load} \times PF = 120 \times 15 \times 0.8 = 1440 \text{ W} \quad ; II \tag{3.40}$$

$$\therefore I \cong II \tag{3.41}$$
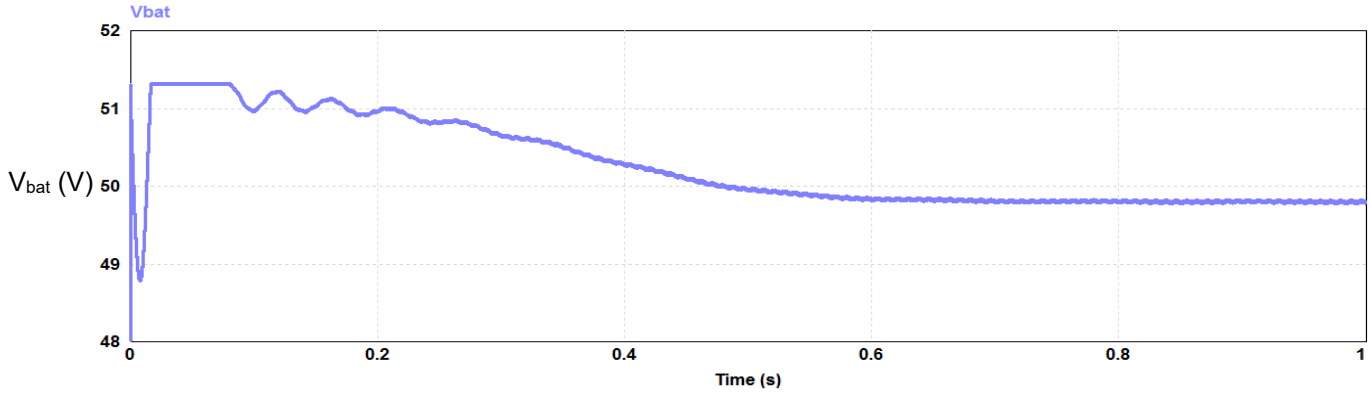
Figure 3.36 Simulated results of mode 3; battery voltage.
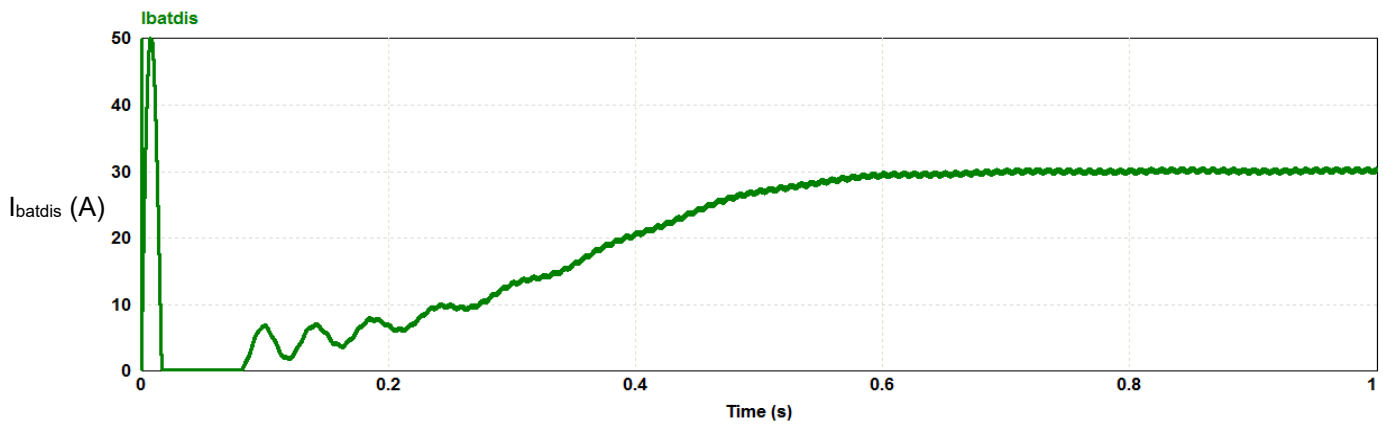
Figure 3.37 Simulated results of mode 3; battery discharge current.
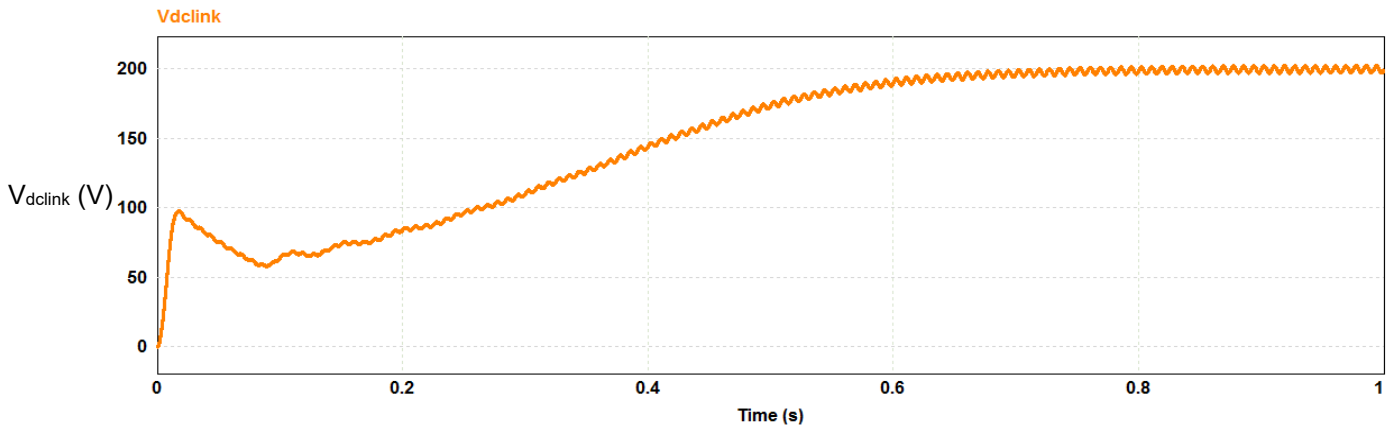
Figure 3.38 Simulated results of mode 3; DC-link voltage.
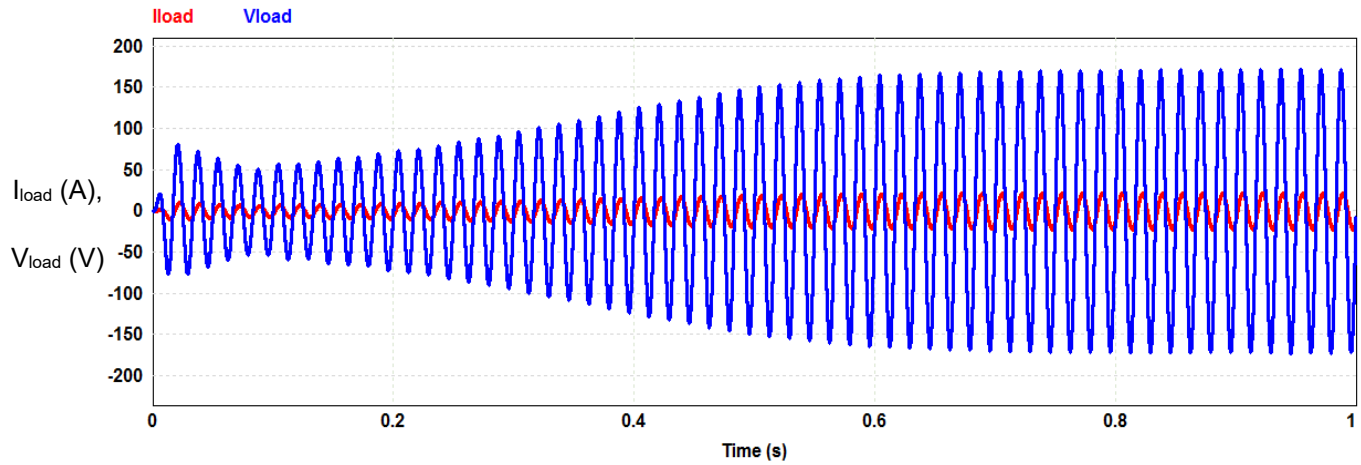
Figure 3.39 Simulated results of mode 3; load voltage and current. The AC voltage is created by the grid-forming inverter in the absence of the grid.
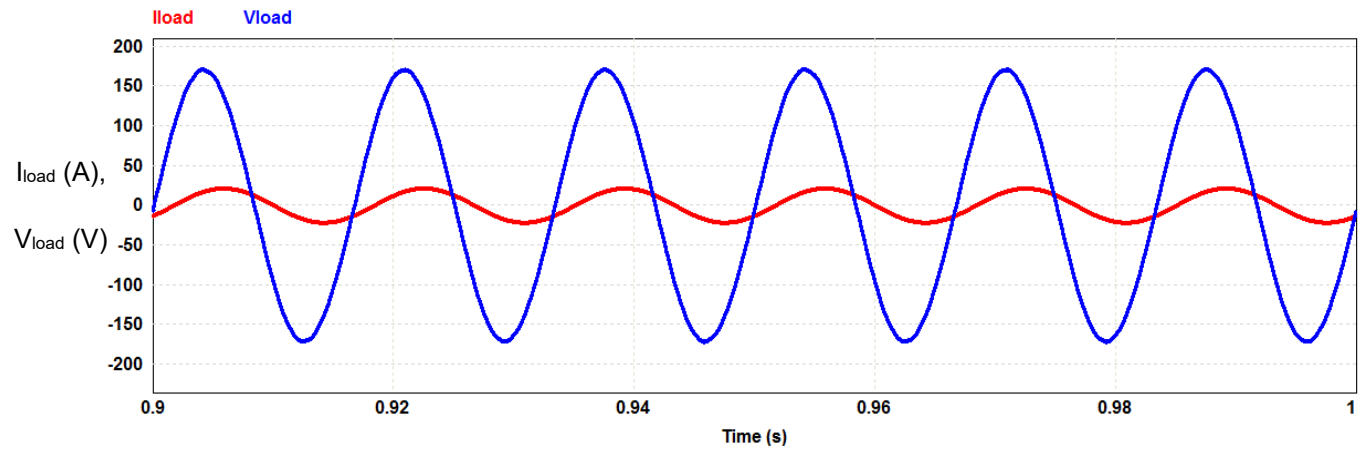
Figure 3.40 Simulated results of mode 3; zoomed version of Figure 3.39 at the steady-state.
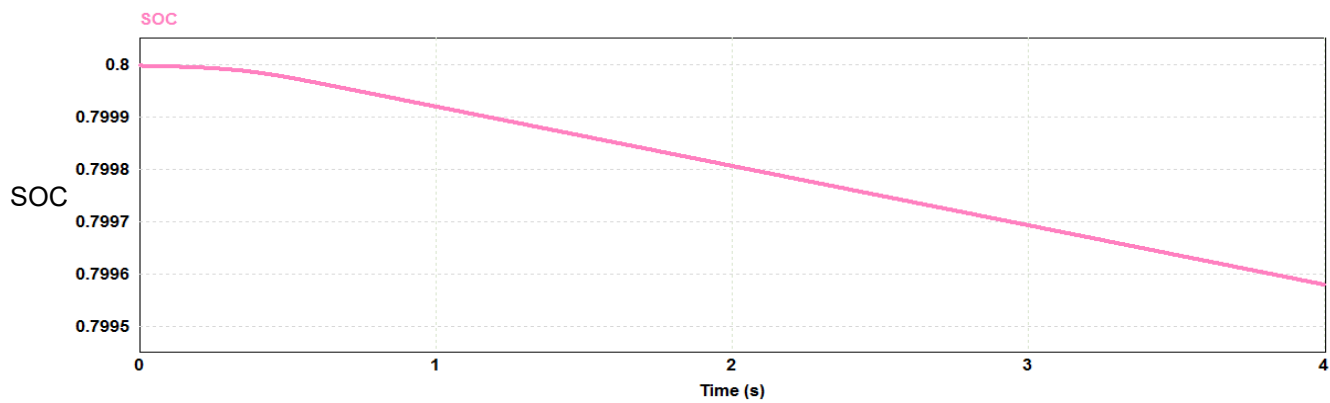
Figure 3.41 Simulated results of mode 3; the battery's SOC. The decreasing trend is observed.

42

Table 3.12 Parameters obtained from the Simulated results of mode 3.

$\mathbf{V_{bat}}$	50 V
$\mathbf{I_{batdis}}$	30 A
	Settles at 0.6 s
	1% ripple
$\mathbf{V_{dclink}}$	200 V
	2% ripple
$\mathbf{I_{load}}$	15 A RMS
$\mathbf{V_{load}}$	120 V RMS
SOC	Decreasing

3.3.3.5 Three-phase configuration and results

In the three-phase circuit, each inverter is connected to one phase at the PCC. The circuit schematic diagram is shown in Figure 3.42. The same as in the three-phase configuration of mode 2, for better demonstration, one battery is used for each phase. This is equivalent to three batteries connected in parallel as a battery pack with a DC bus between the converter and the batteries.

The results of the simulation are illustrated in Figures 3.43 to 3.47. The shown results are the per-phase DC-link voltage $V_{dclinkx}$, the per-phase load current I_{loadx}, and the per-phase load voltage V_{loadx}.

3.3.3.6 Transfer functions

In this mode of operation, the transfer function of the grid-forming inverter is derived, and its frequency response is compared with the result obtained from the System Identification Toolbox in MATLAB. With this toolbox, the converter is seen as a black-box and its transfer function is estimated based on the input and output signals. By knowing the transfer function of a system, the behavior of the system depending on any given input can be mathematically predicted. Transfer functions can also be used for control circuit design and as an approximation for non-linear time-variant systems. The two stages in this converter are the DC/DC boost converter stage and the inverter stage. The analytical derivation of the transfer function for the DC/DC boost converter is done as follows.
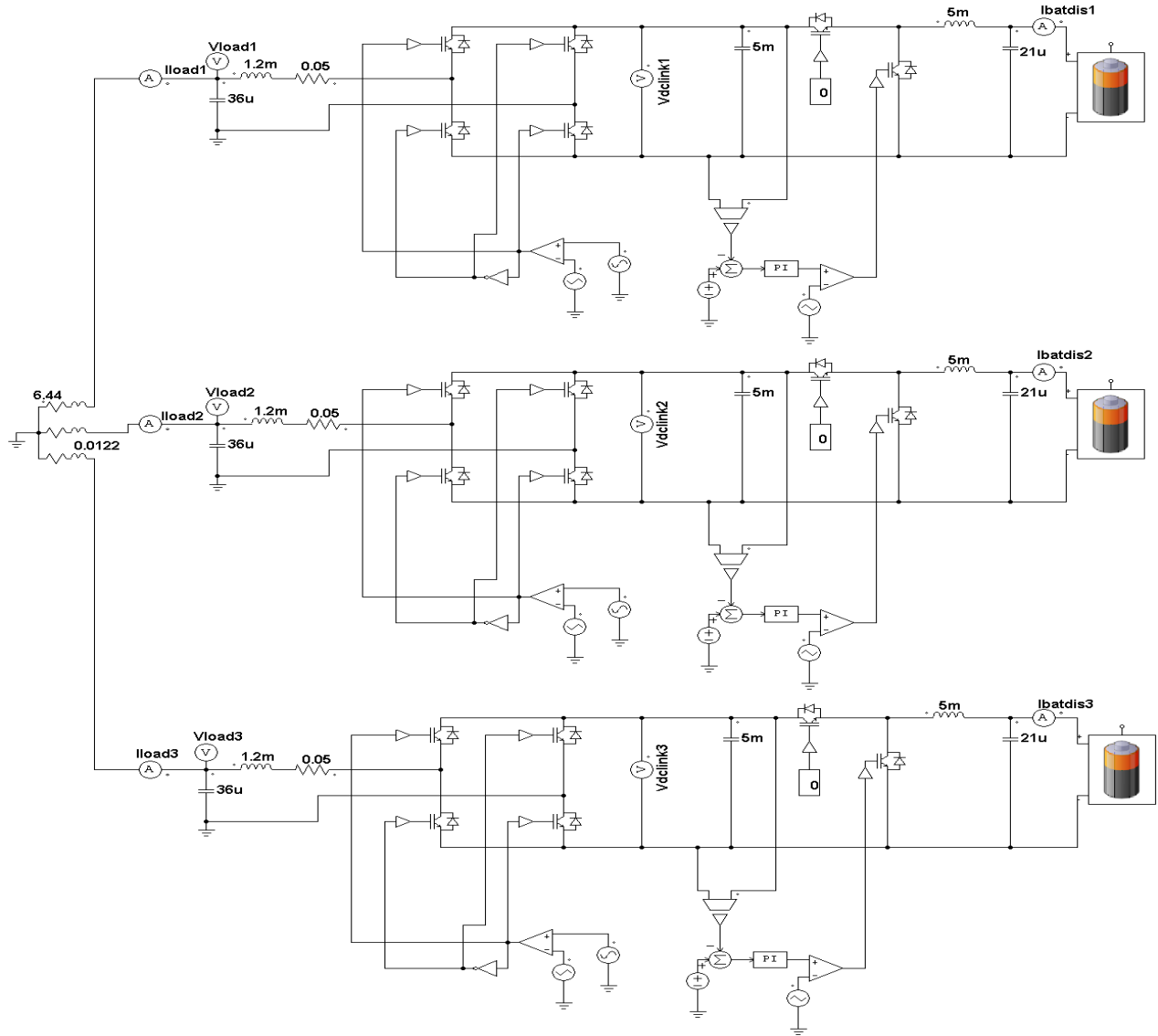
Figure 3.42 Three-phase configuration for the operating mode 3.
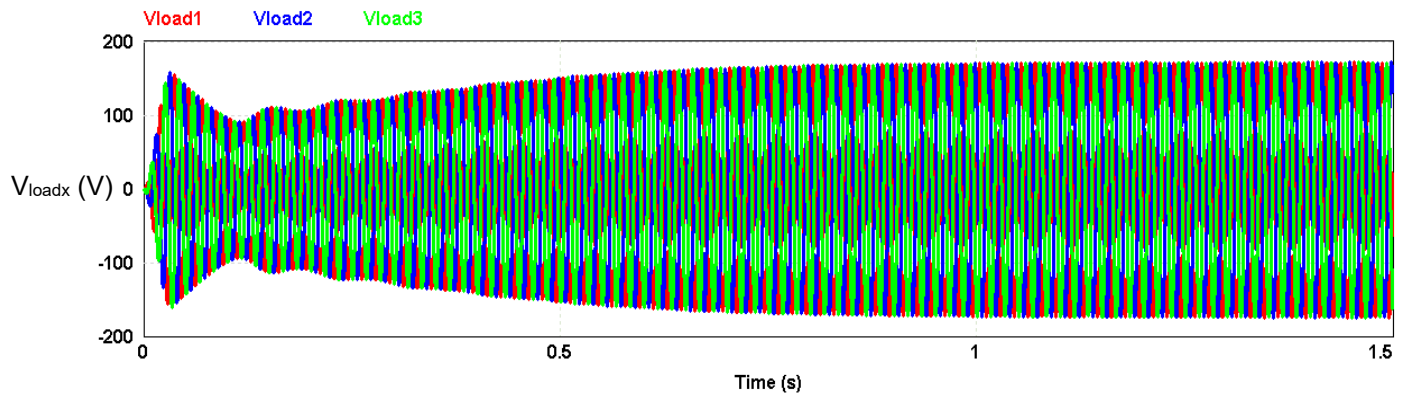
Figure 3.43 Per-phase load voltage in mode 3.
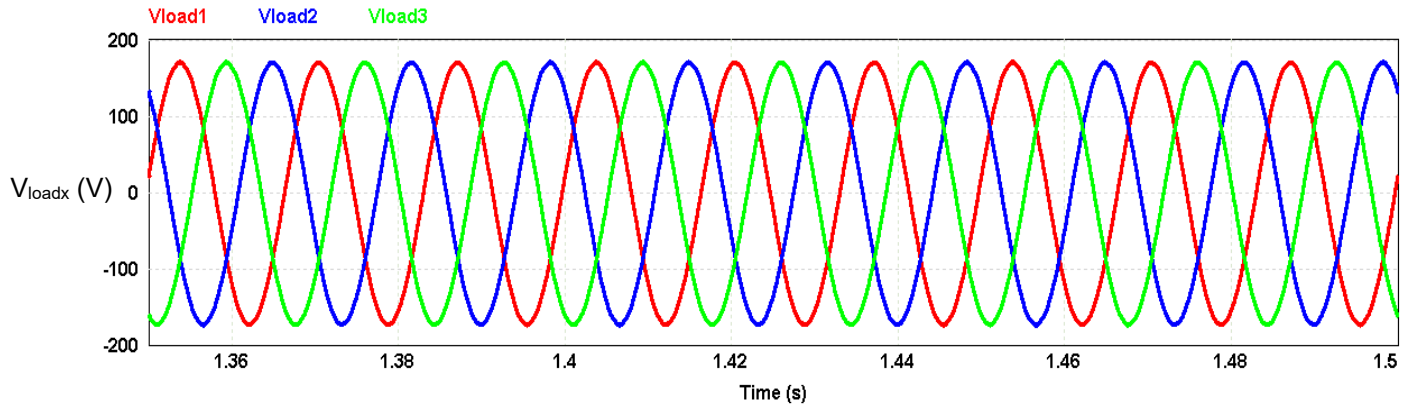
Figure 3.44 Per-phase load voltage in mode 3; steady-state.
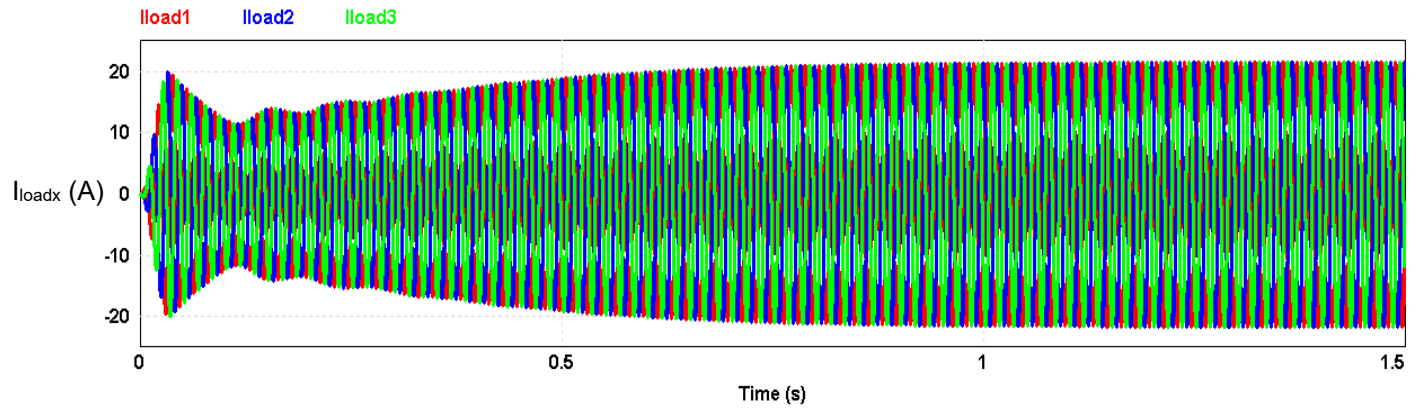
Figure 3.45 Per-phase load current in mode 3.
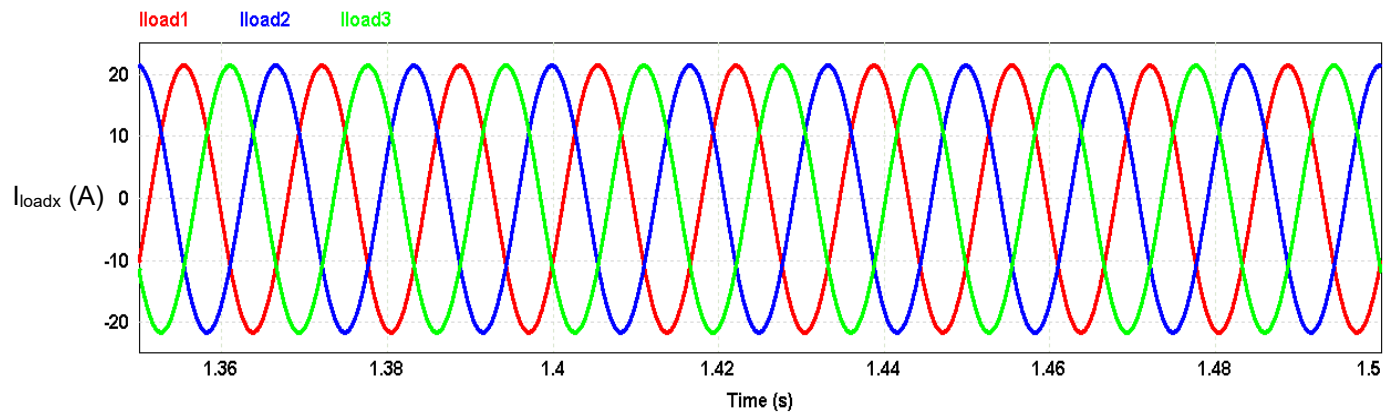
Figure 3.46 Per-phase load current in mode 3; steady-state.
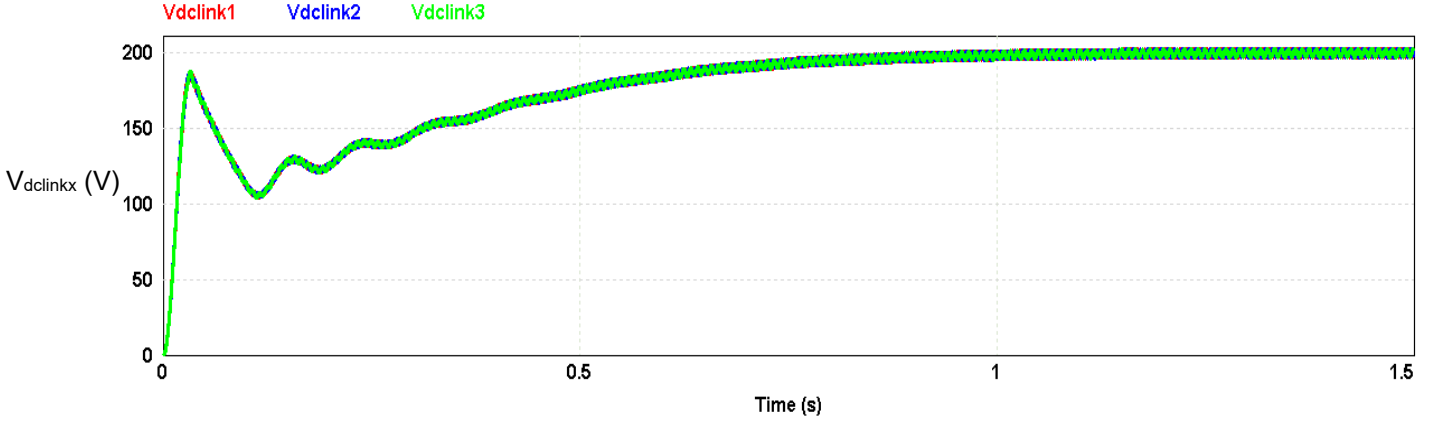
Figure 3.47 Per-phase DC-link voltage in mode 3.

The averaged equations for the DC/DC boost converter are as follows.

$$\begin{cases} L\frac{di_L}{dt} = V_{bat} + (D-1)V_{dclink} \\ C\frac{dv_{dclink}}{dt} = (1-D)i_L - \frac{V_{dclink}}{R} \end{cases} \qquad (3.42)$$

By adding the perturbations, the equations will become as follows.

$$\begin{cases} L\frac{d(I_L+\hat{\imath}_L)}{dt} = (V_{bat} + \hat{v}_{bat}) + (D+\hat{d}-1)(V_{dclink} + \hat{v}_{dclink}) \\ C\frac{d(V_{dclink}+\hat{v}_{dclink})}{dt} = (1-D-\hat{d})(I_L + \hat{\imath}_L) - \frac{(V_{dclink}+\hat{v}_{dclink})}{R} \end{cases} \qquad (3.43)$$

By separating the DC and AC components, the following is obtained.

DC

$$L\frac{dI_L}{dt} = V_{bat} + DV_{dclink} - V_{dclink} \rightarrow V_{bat} = (1-D)V_{dclink} \qquad (3.44)$$

AC

$$\begin{cases} L\frac{d\hat{\imath}_L}{dt} = \hat{v}_{bat} + D\hat{v}_{dclink} + \hat{d}V_{dclink} + \hat{d}\hat{v}_{dclink} - \hat{v}_{dclink} \\ \qquad C\frac{d\hat{v}_{dclink}}{dt} = \hat{\imath}_L - D\hat{\imath}_L - \hat{d}I_L - \hat{d}\hat{\imath}_L - \frac{\hat{v}_{dclink}}{R} \end{cases} \qquad (3.45)$$

The terms which consist of multiplication of two AC components are very small that can easily be neglected. By getting the Laplace transform of the remaining terms in AC equations, two transfer functions are derived as follows.

46

$$\frac{\hat{v}_{dclink}}{\hat{d}} = \frac{V_{dclink}(1-D)R - I_L LRs}{LRCs^2 + Ls + R(1-D)^2} \tag{3.46}$$

$$\frac{\hat{v}_{dclink}}{\hat{v}_{bat}} = \frac{R}{LRCs^2 + Ls + R(1-D)^2} \tag{3.47}$$

The parameters of the DC/DC boost converter are as follows.

$$V_{bat} = 48 \text{ V}, V_{dclink} = 200 \text{ V}, D = 0.76, I_L = 37 \text{ A}, L = 5 \text{ mH}, C = 5 \text{ mF}, R = 13.88 \ \Omega, \tag{3.48}$$

where L is the boost converter inductance, I_L is the inductance current, V_{bat} is the battery voltage, D is the duty cycle of the boost converter, V_{dclink} is the output voltage of the boost converter, C is the output capacitor of the boost converter, and R is the load of the boost converter. The parameters that are written in capital letters are the DC values and the ones written in small letters with hats are the perturbations of the respective parameters.

By plugging the values of the parameters shown by (3.48) in (3.47), the following transfer function is obtained.

$$\frac{V_{dclink}}{V_{bat}} = \frac{13.88}{3 \times 10^{-4} s^2 + 5 \times 10^{-3} s + 0.8} \tag{3.49}$$

R is the load seen at the output of the boost converter. With 200 VDC output, 37 A discharge current, and the same house load as in Table 3.11, R is calculated to be 13.88 Ω. Equation (3.46) is used to design the PI controller for the DC/DC boost converter in MATLAB. The PI controller values are the same as the ones in Table 3.11.

For the inverter, the transfer function is derived as follows. A gain and a time delay are considered for the transfer function as in (3.50), which shows the relationship between the DC-link voltage and the converter PWM voltage.

$$\frac{V_{conv}}{V_{dclink}} = \frac{M.I.}{1 + s\tau} \tag{3.50}$$

$$M.I. = \frac{V_{conv}}{V_{dclink}} = 0.878 \tag{3.51}$$

$$f_s = 20 \text{ kHz} \rightarrow \tau = \frac{1}{f_s} = \frac{1}{20000} = 50 \ \mu s, \tag{3.52}$$

where V_{conv} is the output voltage of the inverter, V_{dclink} is the DC-link voltage, M.I. is the modulation index, f_s is the switching frequency, and τ is the switching period.

The values for the M.I and τ are plugged into (3.50), and the following transfer function for the inverter is obtained.

$$\frac{V_{conv}}{V_{dc}} = \frac{0.878}{1+5\times10^{-5}s}.$$ (3.53)

Lastly, the transfer function of LC filter is given by (3.54).

$$\frac{V_{load}}{V_{conv}} = \frac{1}{1+L_{filt}C_{filt}s^2}$$ (3.54)

$$L_{filt} = 1.2 \text{ mH}, C_{filt} = 36 \text{ μF},$$ (3.55)

where V_{load} is the load voltage, L_{filt} is the filter inductance, and C_{filt} is the filter capacitance.

The designed values for the filter's parameters, which are shown in (3.55), are plugged into (3.54) and the following transfer function is obtained.

$$\frac{V_{load}}{V_{conv}} = \frac{1}{1+4.32\times10^{-8}s^2}$$ (3.56)

The transfer function of the whole system from V_{bat} to V_{load} is calculated by multiplying the transfer functions in (3.49), (3.53), and (3.56), and the following is obtained.

$$\frac{V_{load}}{V_{bat}} = \frac{0.878}{5.4\times10^{-17}s^5+1.08\times10^{-12}s^4+1.266\times10^{-9}s^3+2.502\times10^{-5}s^2+3.631\times10^{-4}s+0.0576}$$ (3.57)

Figures 3.48 to 3.51 show the frequency responses for the different stages of the converter and that for the whole converter.

The System Identification Toolbox in MATLAB is used to estimate the transfer function of the whole converter without the need of knowing the system parameters or equations Equation (3.58) shows the estimated transfer function. The signals that are given to the System Identification Toolbox are V_{bat} as the input (Figure 3.36) and V_{load} as the output (Figure 3.40).

$$\frac{V_{load}}{V_{bat}} = \frac{-2.31\times10^{13}s-4.72}{s^5+4035s^4+1.47\times10^7s^3+1.82\times10^{10}s^2+2.07\times10^{12}s+2.5\times10^{15}}$$ (3.58)

Figure 3.52 shows the frequency response of the estimated transfer function using the System Identification Toolbox. This transfer function is 97% fit to the output. The fit to the output of the estimated transfer function is a metric calculated by the System Identification Toolbox for the validation of the results. The output is calculated by multiplying the input signal in the frequency

domain with the estimated transfer function and doing a reverse Laplace transformation to obtain the time-domain output signal. This signal is then compared to the actual output signal given to the Toolbox for the estimation. The fitting percentage shows how much these two output signals match.

As far as the order is concerned, (3.57) and (3.58) are both fifth-order transfer functions. The estimated transfer function has a zero which cannot be seen in (3.57), and the values of poles are different because the System Identification Toolbox in MATLAB uses different algorithms than how (3.57) was obtained. However, both the calculated and the estimated transfer functions are 5th-order stable transfer functions.
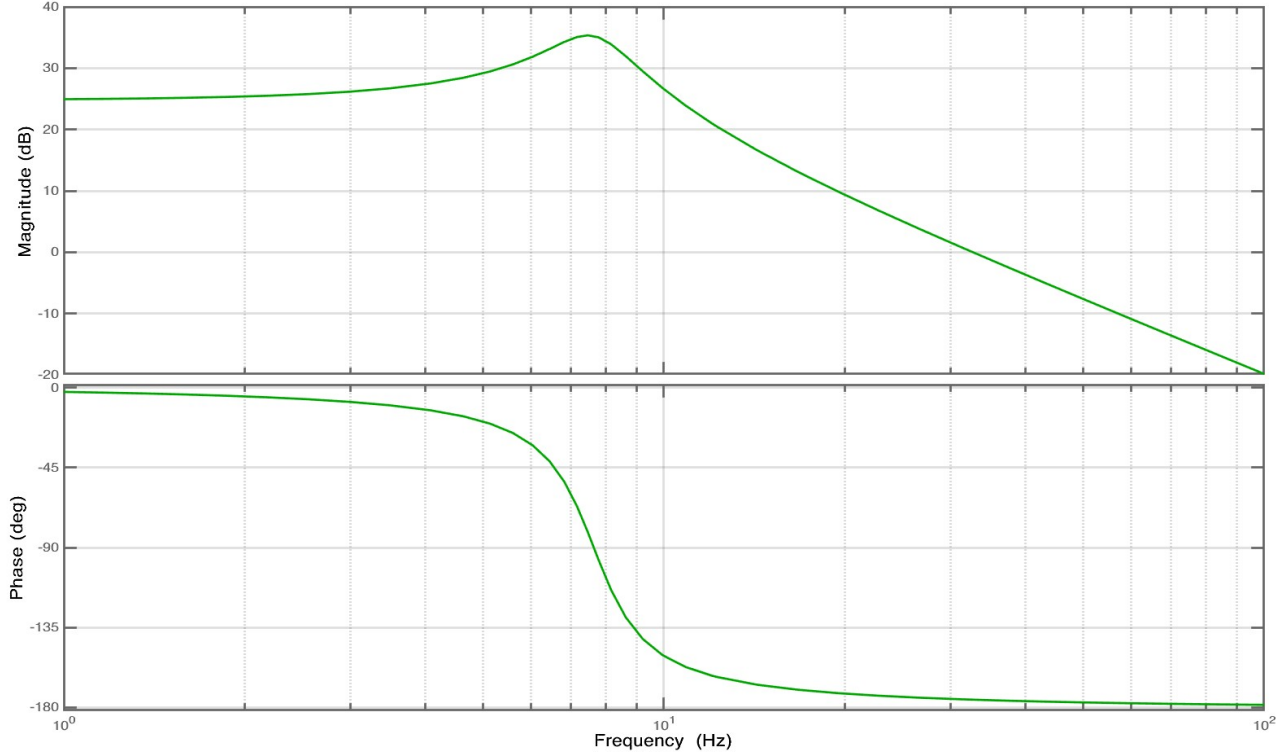
Figure 3.48 Frequency response of the DC/DC boost converter.

49
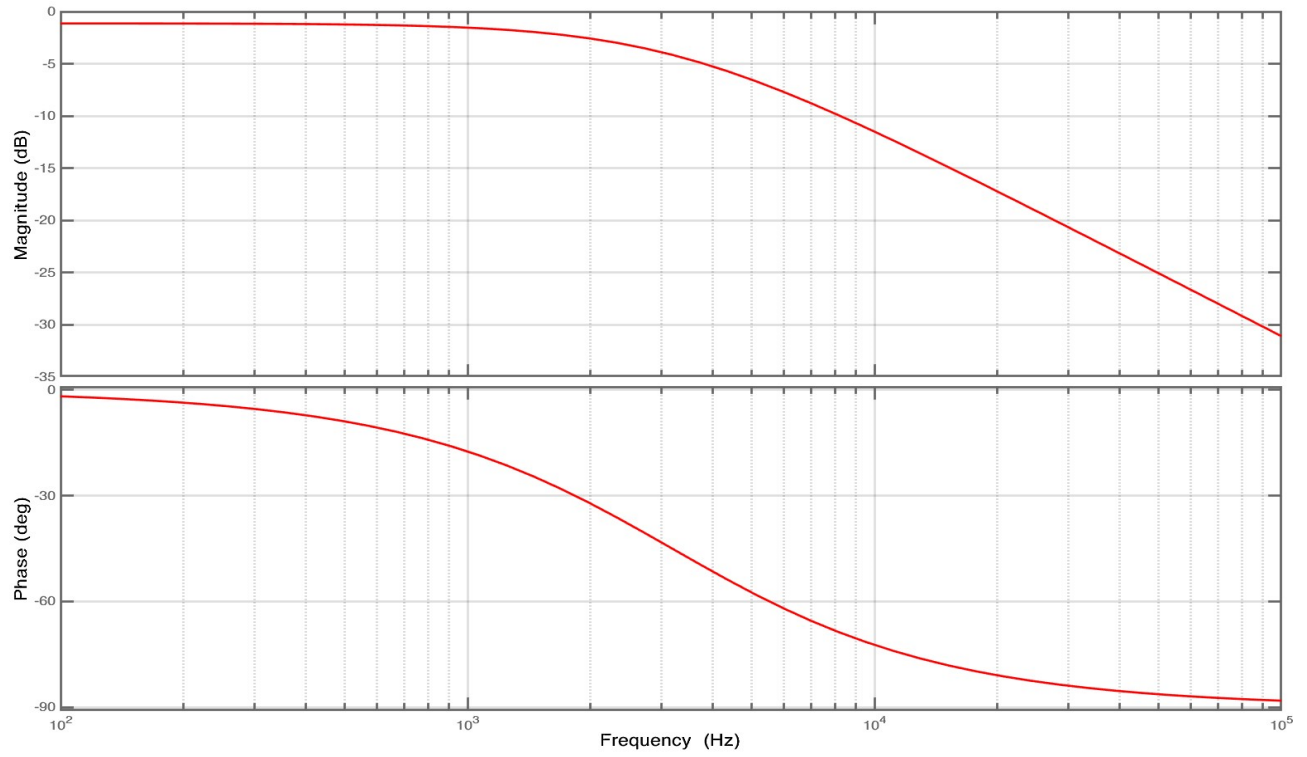
Figure 3.49 Frequency response of the inverter.
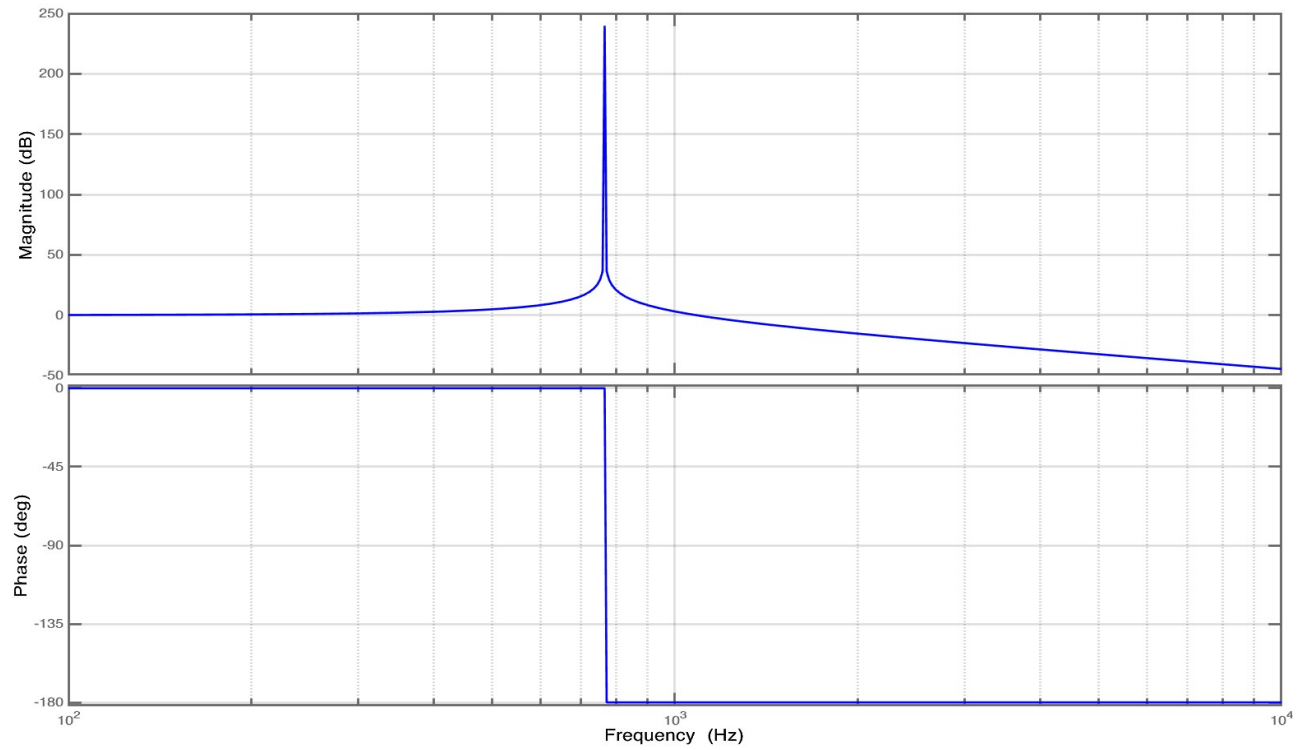
Figure 3.50 Frequency response of the LC filter.
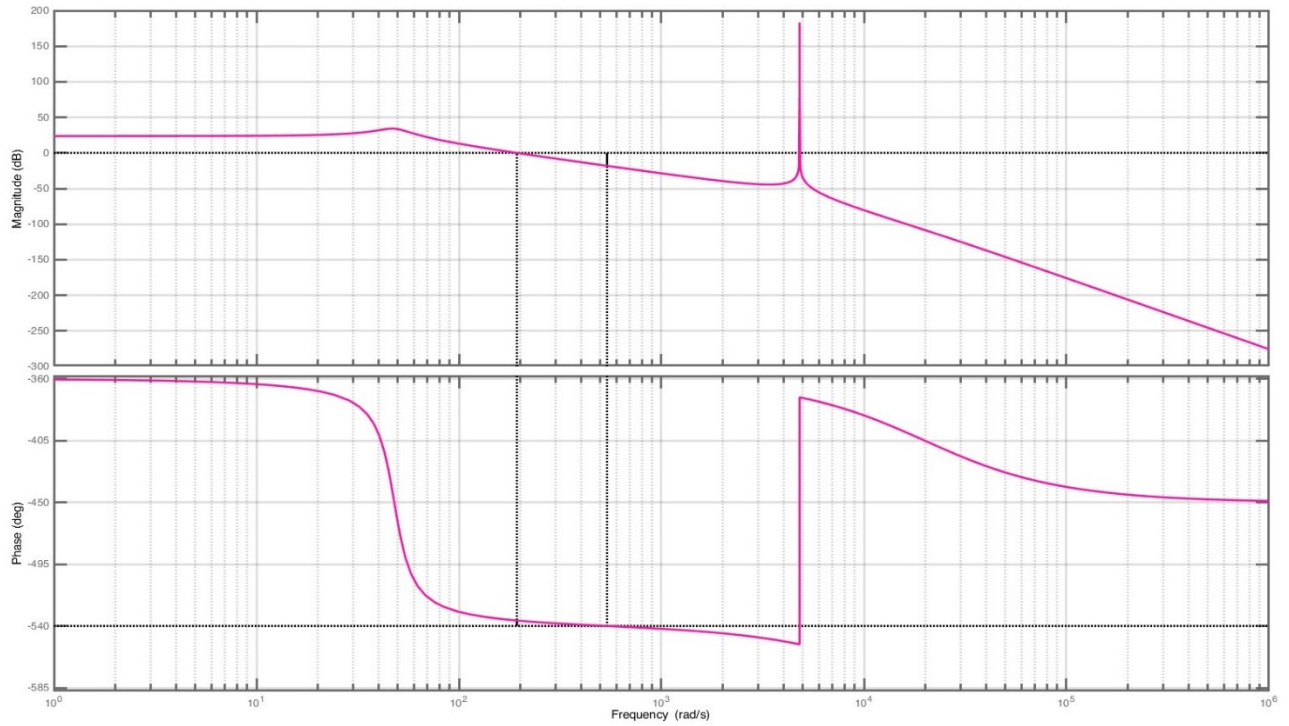
Figure 3.51 Frequency response of the whole converter obtained from the analytically derived transfer function (3.62).
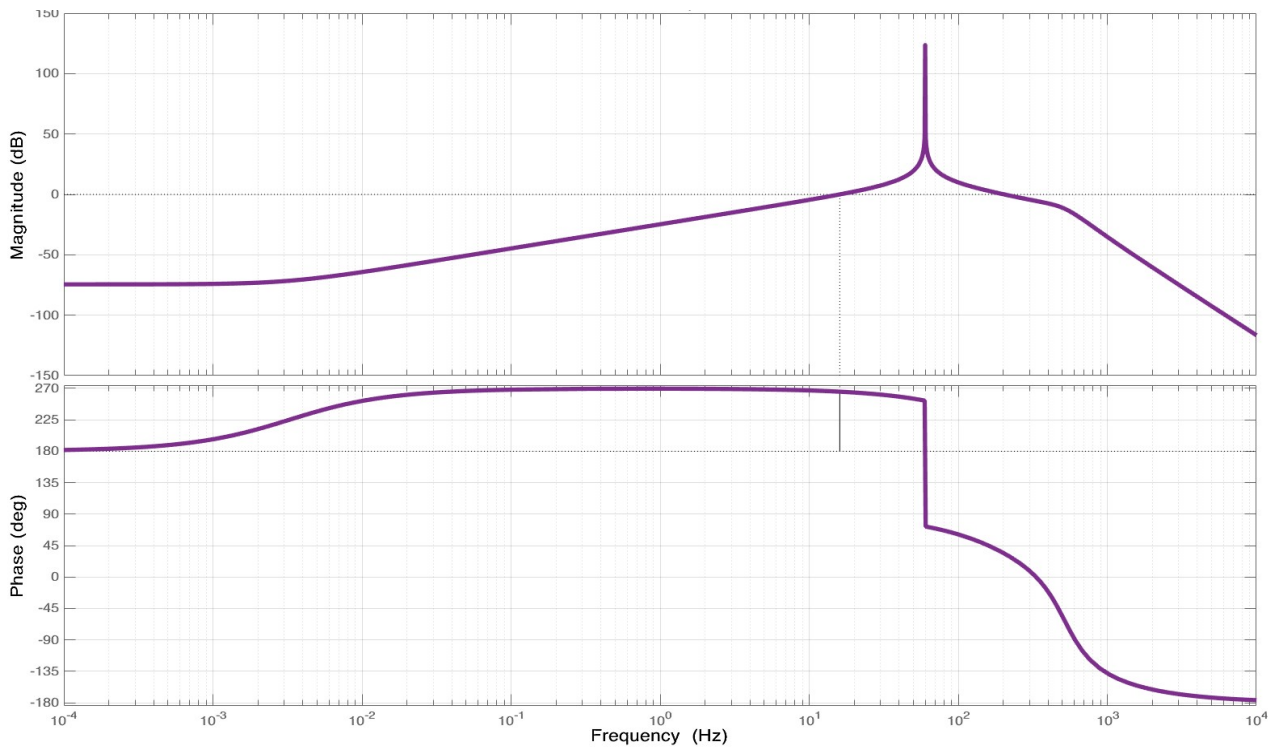
Figure 3.52 Frequency response of the whole converter obtained from the estimated fifth-order transfer function using System Identification Toolbox in MATLAB; 97% fit to the output.

51

3.4 Summary

In this chapter, the electrical aspects of the solar power system for the FBL are presented. The three modes of operation 1) grid feeds the load, 2) grid charges the battery, and 3) battery feeds the load are modeled and discussed in detail. In the next chapter, mode 3 of operation will be experimentally examined and studied.

Chapter 4 Experimental Work

4.1 Introduction

In this chapter, the converter discussed in Chapter 3 for the operating mode 3 (battery feeds the load) is built experimentally. The results are presented and compared with the simulated results.

4.2 Setup and results

The experimental setup is built step-by-step to make an AC grid-like voltage from a DC battery voltage at the PEER group laboratory.

A variac and a 3-phase rectifier are used to make a DC battery-like voltage. The 3-phase rectifier is part of a 3-phase *Semiteach* inverter from Semikron. The output DC voltage of the rectifier is regulated by the DC capacitor that comes with the Semiteach inverter package (C_{reg}) as shown in Figure 4.1. The generated DC voltage, which acts as the battery voltage, is applied to a DC inductor (L_{boost}) and then to a 3-phase switch mode converter with three legs that each has two switches. One leg (S5 and S6) is used and switched as a boost converter. The output capacitor of the boost converter ($C_{dc-link}$) is provided by the capacitor that is already present in the three-leg converter setup. A resistance (R) of 122 Ω is used as a load for the converter. To create a 200 VDC at the output of the DC/DC boost converter, a constant duty cycle is given to S6, whereas S5 is kept always OFF. All control signals are given by OPAL-RT to the gate drive circuit of the three-phase converter. Figure 4.1 shows the schematic diagram of the boost converter.

Figure 4.2 shows the experimental setup of the circuit in Figure 4.1. The values of the elements used in the setup are in Table 4.1. V_{in_boost} is the input voltage of the DC/DC boost converter. Except for the capacitors that are built-in components of the inverters, the values of the inductors and capacitors are chosen to be close to the designed circuit in Chapter 3 based on the available elements in the laboratory. The results of the boost converter are shown in Figures[8] 4.3 to 4.5.

---

[8] The 0 (s) indicated on the x-axis of the result graphs do not necessarily show the beginning of experiments, as the recording is taken for a specific period in the steady state.
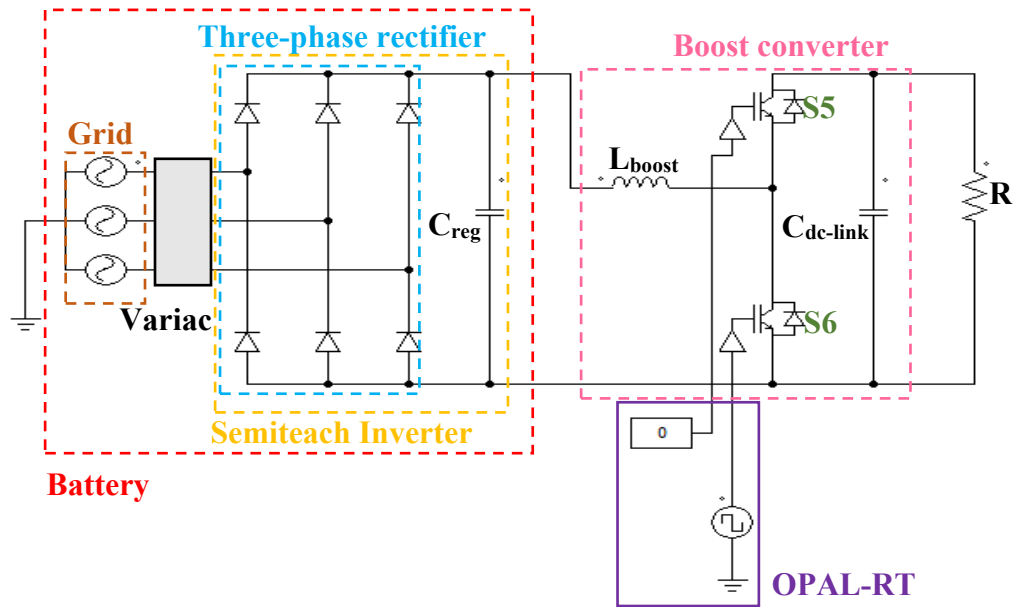
Figure 4.1 Schematic diagram of the boost converter.
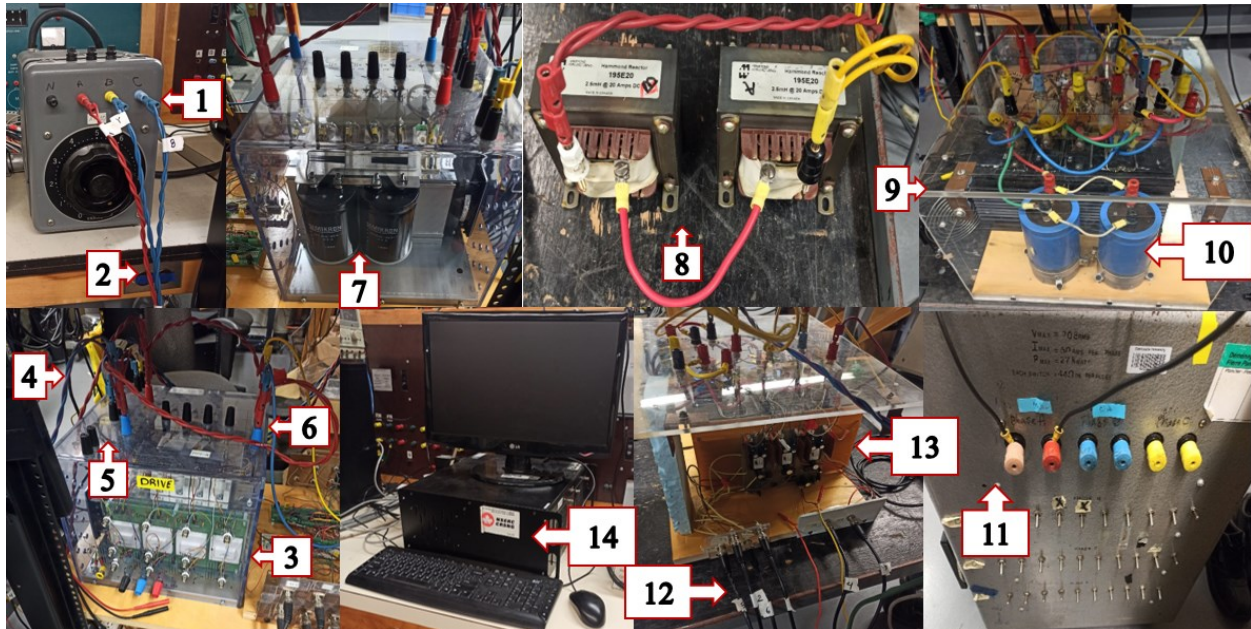
Figure 4.2 Boost converter experimental setup; (1) Variac, (2) AC 3-φ output of variac, (3) Semiteach inverter, (4) AC 3-φ input of rectifier, (5) 3-φ diode rectifier, (6) DC output of the rectifier, (7) C_{reg}, (8) L_{boost}, (9) 3-φ inverter (only one leg is used), (10) $C_{dc\text{-}link}$, (11) R, (12) Switching pulses input, (13) Gate drive, (14) Real-time simulator (OPAL-RT).

Table 4.1 Parameters' values of the experimental setup for the boost converter.

V_{in_boost}	50 V
C_{reg}	1.32 mF
L_{boost}	2.5 mH ‖ 2.5 mH = 1.25 mH, 20A

$C_{dc\text{-}link}$	3.3 mF ‖ 3.3 mF=6.6 mF, 350 VDC
R	122 Ω
Duty cycle	0.75

The switches in the other two legs (S1-S4) are switched as a single-phase inverter. At the output of the inverter, an LC filter (L_{filt} and C_{filt}) is connected to obtain a smooth AC voltage and current for the load. The schematic is shown in Figure 4.6. The inverter is switched using a bipolar SPWM technique with a 10 kHz carrier frequency. The experimental setup of the inverter is shown in Figure 4.7. The values of the filter and the load are in Table 4.2. V_{in_inv} is the input DC voltage of the inverter.
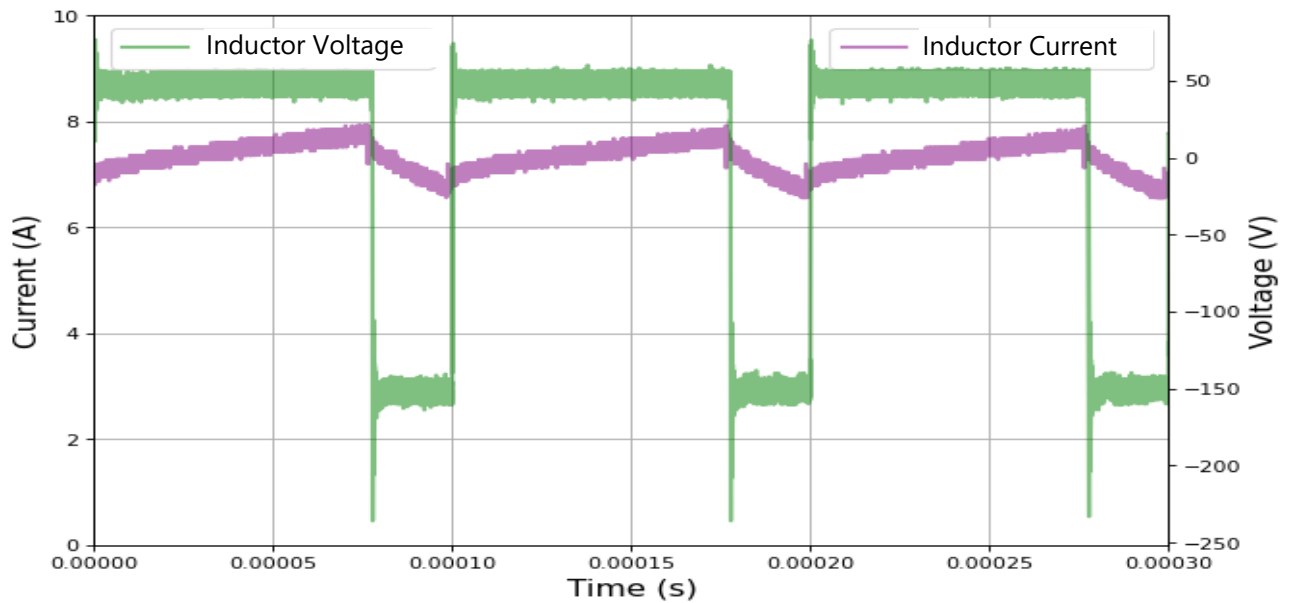
Figure 4.3 The inductance's (L_{boost}) voltage and current of the DC/DC boost converter.
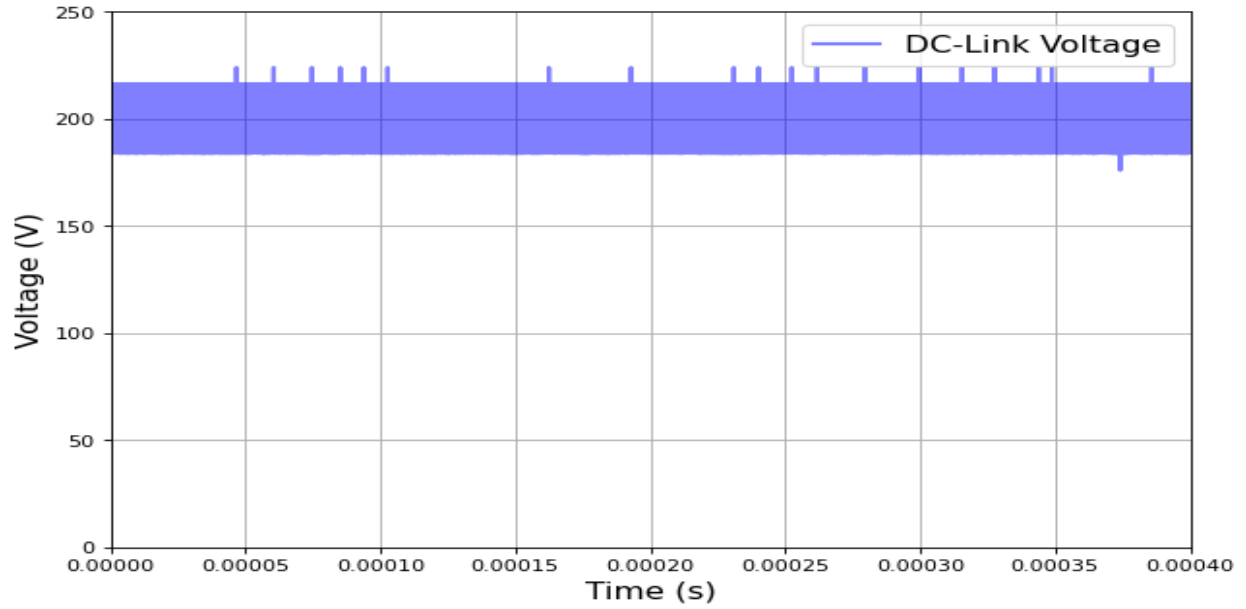
Figure 4.4 The output voltage of the DC/DC boost converter.
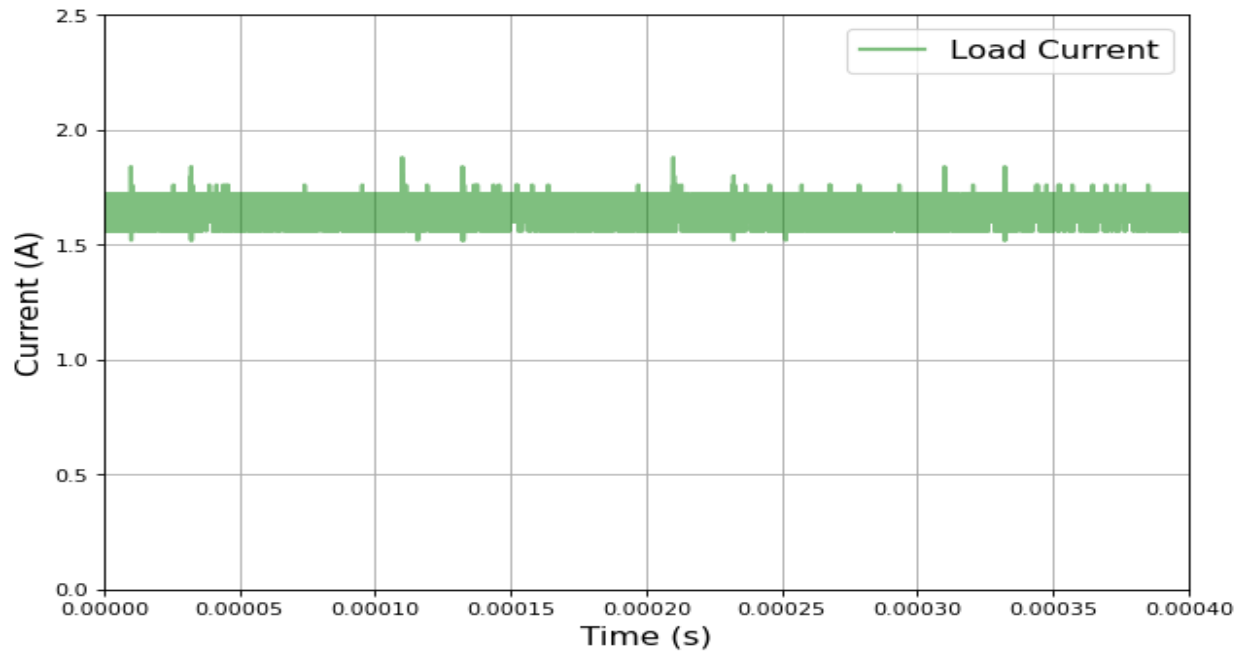
Figure 4.5 Load current.

The results of the inverter experiments are shown in Figures 4.8 and 4.9.
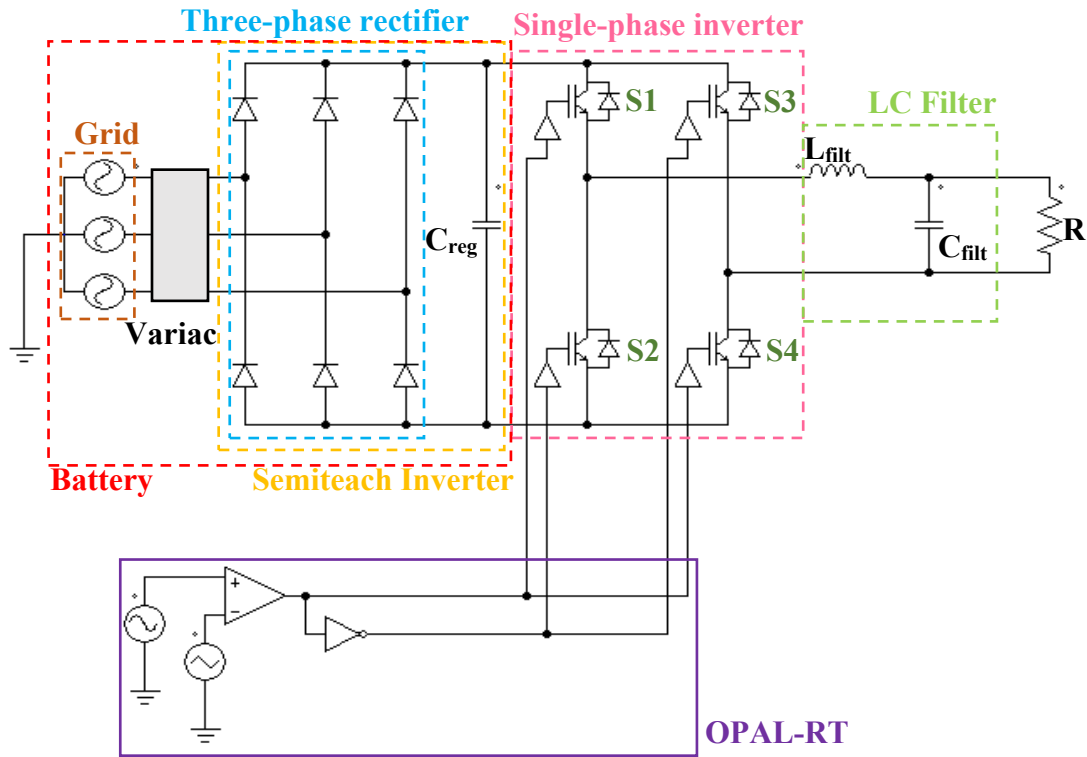
Figure 4.6 Schematic diagram of the Single-phase inverter.

Figure 4.7 Single-phase inverter experimental setup; (1) Variac, (2) AC 3-φ output of variac, (3) Semiteach inverter, (4) AC 3-φ input of the rectifier, (5) 3-φ diode rectifier, (6) DC output of the

rectifier, (7) C_{reg}, (8) 3-φ inverter (two legs are used), (9) L_{filt}, (10) C_{filt}, (11) R, (12) Switching pulses input, (13) Gate drive, (14) OPAL-RT.

Table 4.2 LC filter and load values used in the inverter setup.

$\mathbf{V_{in\text{-}inv}}$	200 V
$\mathbf{L_{filt}}$	1 mH, 100 Hz, 20 A
$\mathbf{C_{filt}}$	6 µF ‖ 6 µF=12 µF, 370 V, 60 Hz
$\mathbf{R}$	40 Ω
$\mathbf{M.I.}$	0.85

After making sure the two stages of the converter (the DC/DC boost converter stage and the inverter stage) can perform separately as desired, the two stages are put together to make the grid-forming inverter. Two control techniques are used for the DC/DC boost converter. In the first one, which is depicted in Figure 4.10, an open-loop control of the DC/DC boost converter is implemented. A duty cycle of 0.78 with a switching frequency of 10 kHz is given to S6, whereas S5 is kept OFF. The results of the grid forming converter with open-loop control are shown in Figures 4.13 and 4.14. In the second technique, a closed-loop control is implemented for the boost converter where the output voltage is controlled by a PI controller. This is shown in Figure 4.11. Figure 4.12 shows the setup for the grid-forming inverter. The results of the grid forming converter with a closed-loop control of the DC/DC boost converter are shown in Figures 4.15 and 4.16.
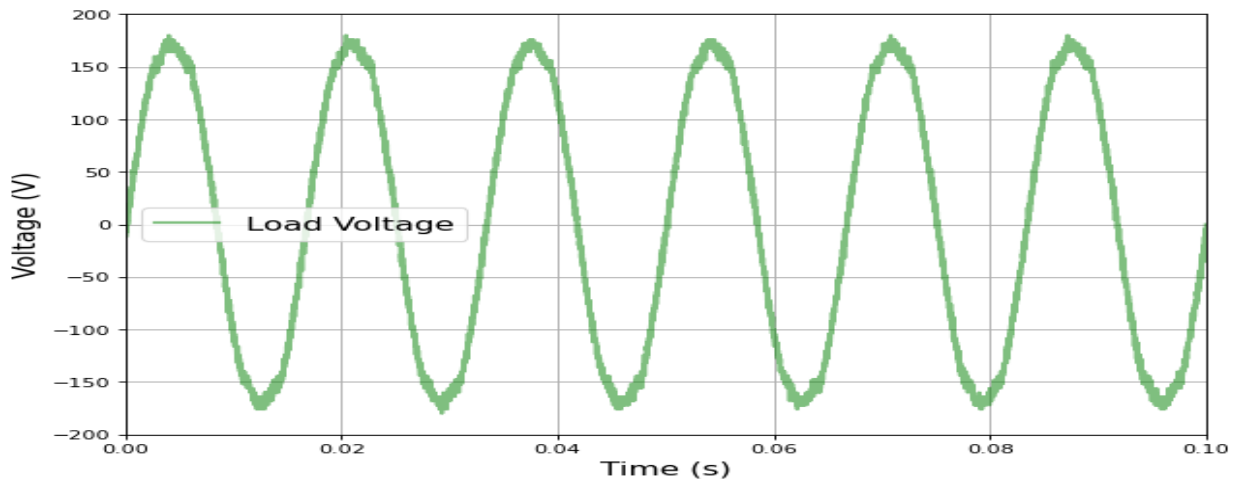
Figure 4.8 Load voltage of the inverter.

58
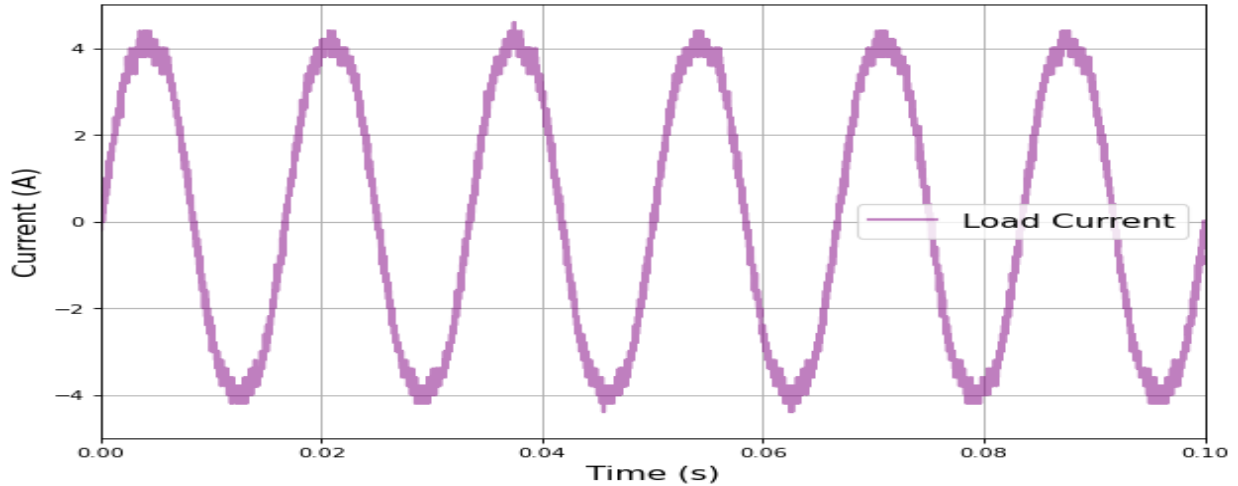
Figure 4.9 Load current of the inverter.

The load of the grid-forming inverter is an 80 Ω resistive load and the DC-link voltage is kept at 200 V. Table 4.3 shows the controller parameters of the grid-forming inverter.

Table 4.3 PI controller and SPWM parameters.

Boost converter PI controller	K_p	0.01
	K_i	0.02
Bipolar SPWM	M.I.	0.92
	Modulating signal frequency	60 Hz
	Carrier frequency	10 kHz

As can be seen, the results of the grid-forming inverter are very similar to the ones derived from the simulation. A fast Fourier transformation (FFT) is done to determine the total harmonic distortion of the experimentally obtained voltage and current signals of the grid-forming inverter. Figures 4.17 to 4.20 show the FFT of the voltage and current waveforms of the grid-forming inverter[9].

---

[9] In the FFT graphs, the value of the fundamental is scaled to 1 and the harmonics are brought in comparison with the fundamental to better demonstrate the power of the harmonics.
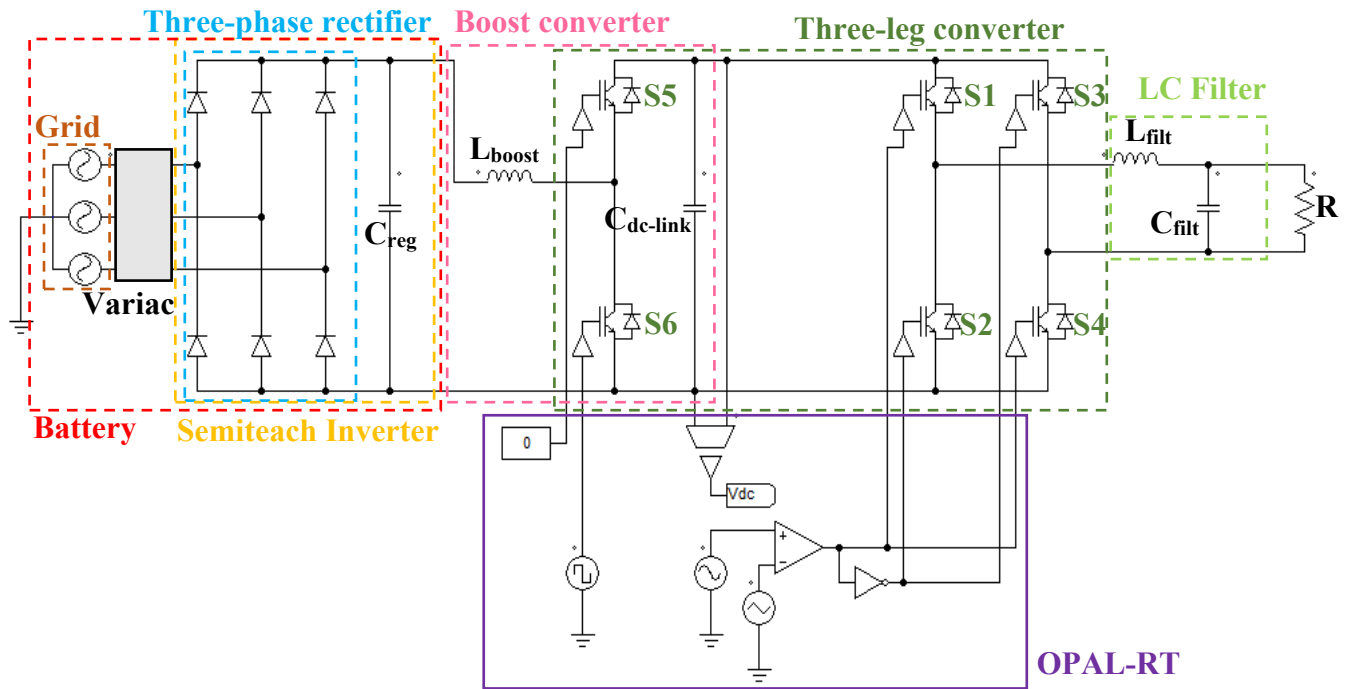
Figure 4.10 Grid-forming inverter with open-loop control.
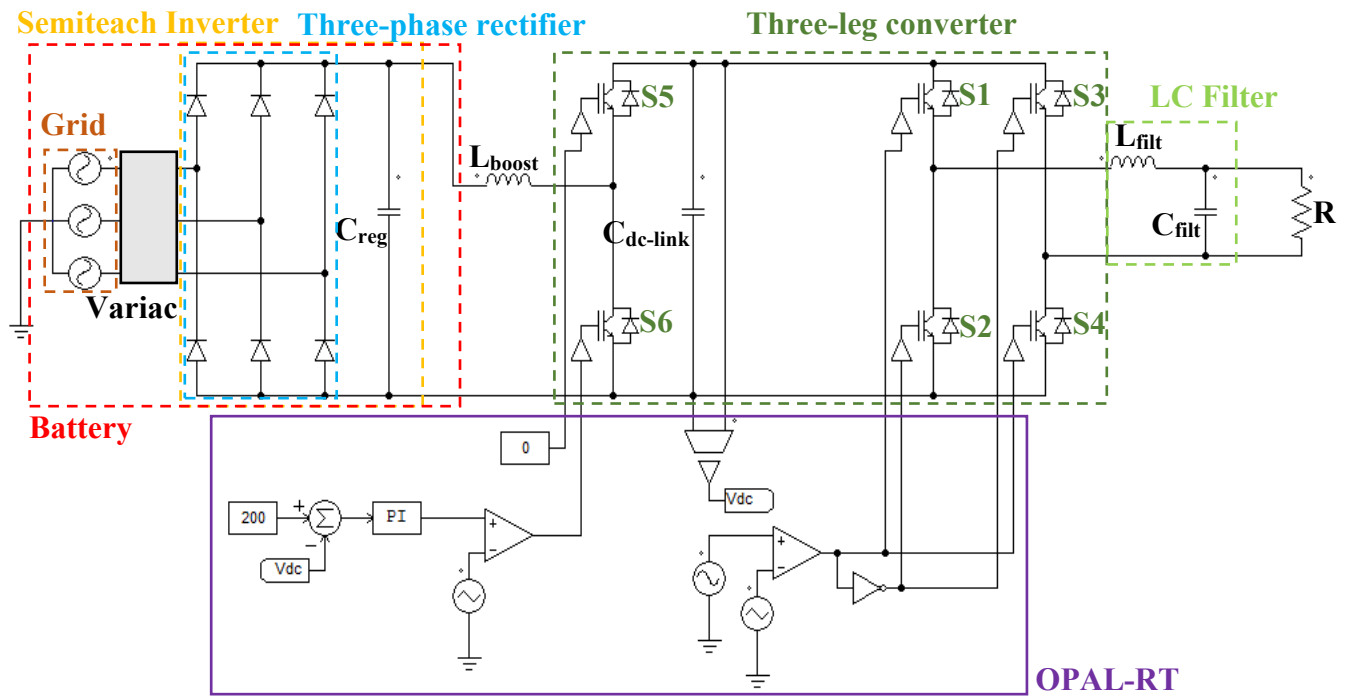
Figure 4.11 Grid-forming inverter with a closed-loop control for the DC/DC boost converter.

60
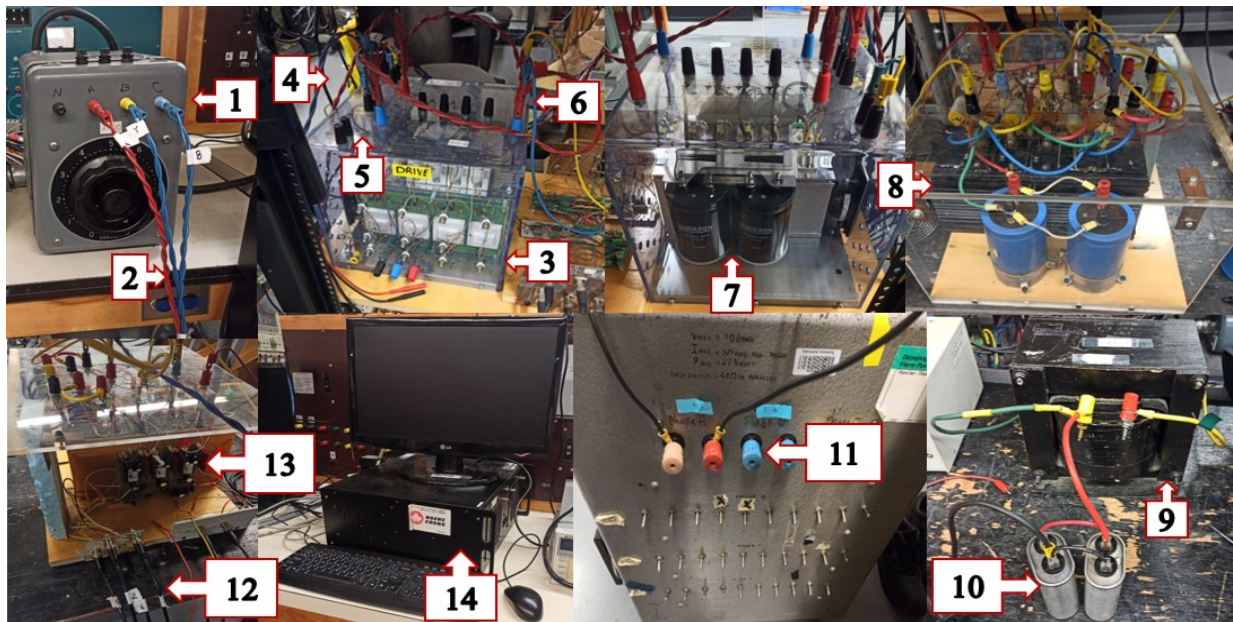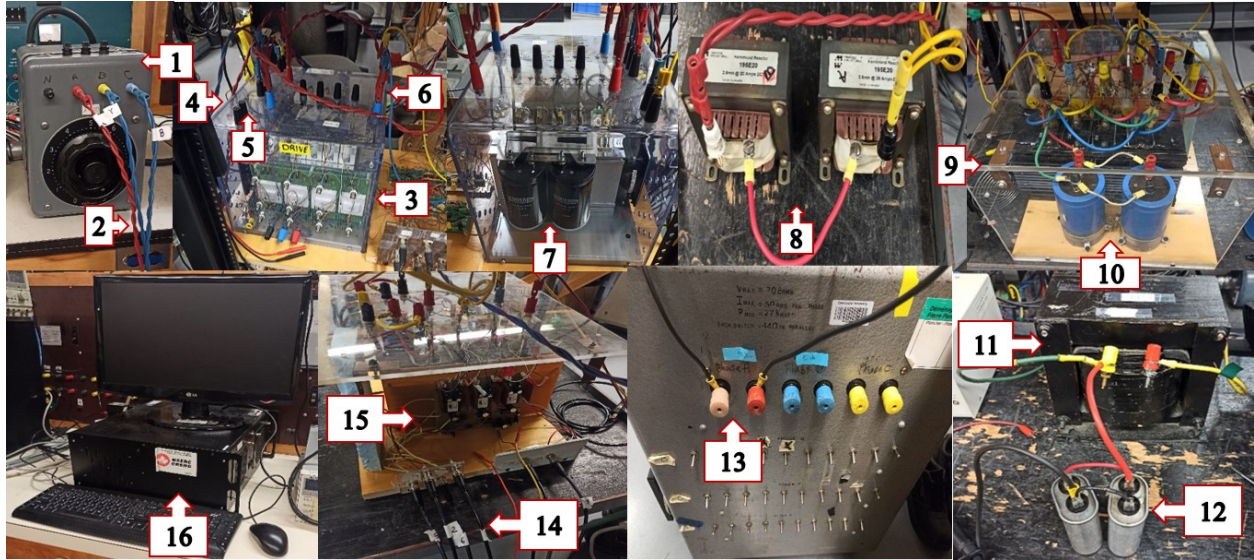
Figure 4.12 Grid-forming inverter experimental setup; (1) Variac, (2) AC 3-φ output of variac, (3) Semiteach inverter, (4) AC 3-φ input of rectifier, (5) 3-φ diode rectifier, (6) DC output of rectifier, (7) C_{reg}, (8) L_{boost}, (9) 3-φ inverter (one leg is used for the boost converter and the other two legs are used for the single-phase inverter), (10) $C_{dc\text{-}link}$, (11) L_{filt}, (12) C_{filt}, (13) R, (14) Switching pulses input, (15) Gate drive, (16) OPAL-RT.
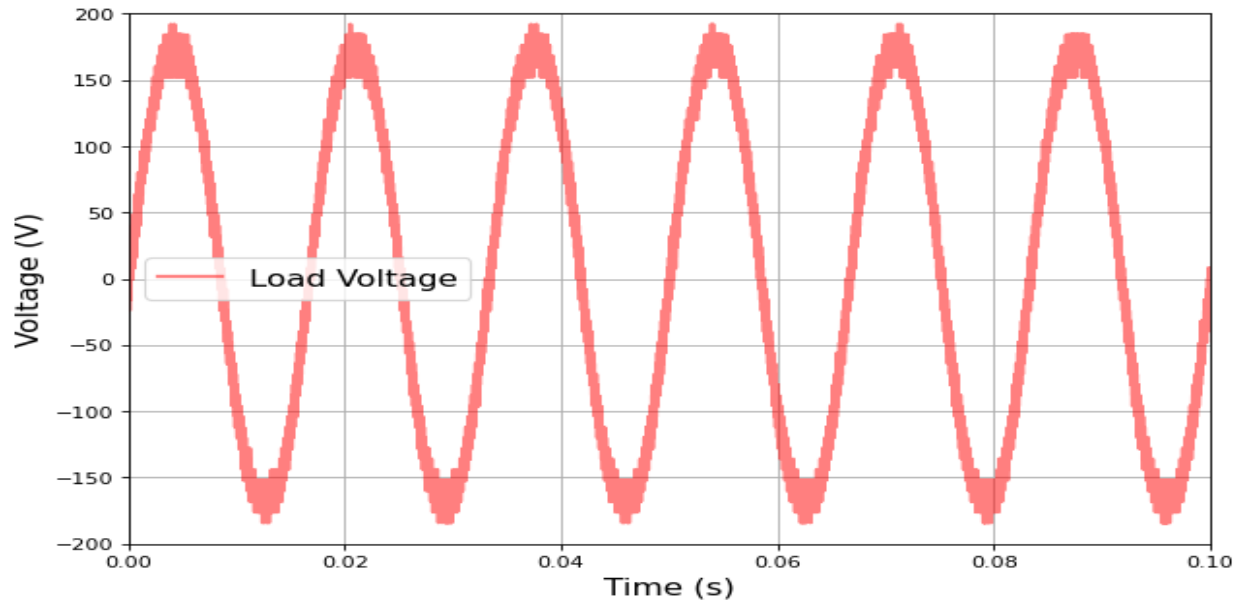
Figure 4.13 Load voltage of the grid-forming inverter with open-loop control.
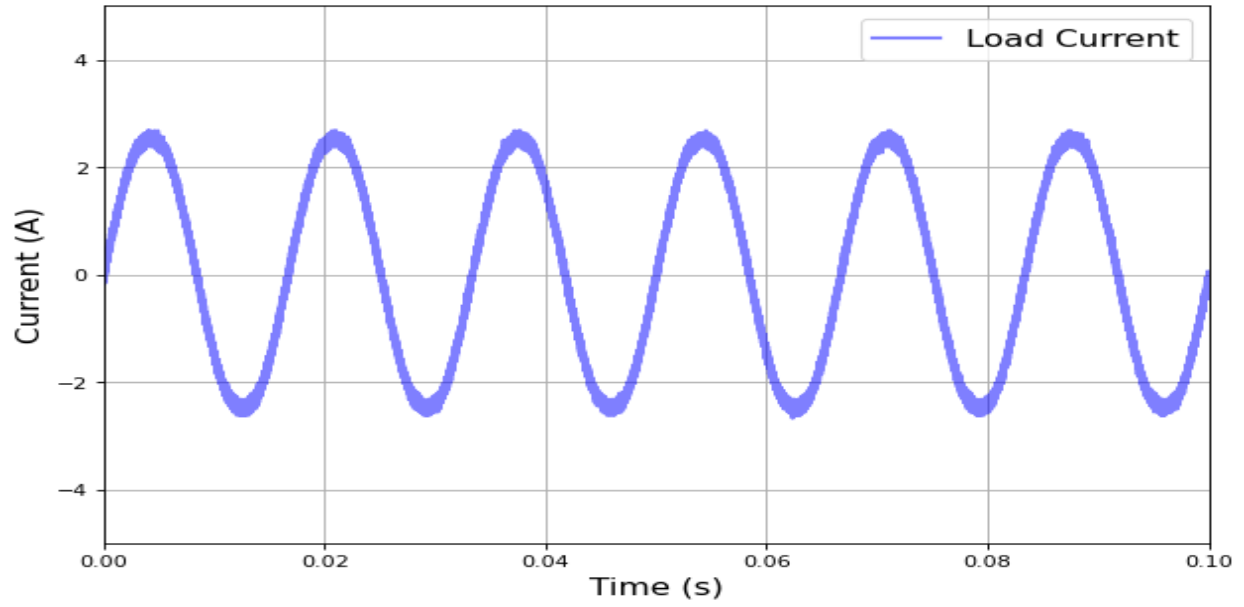
Figure 4.14 Load current of the grid-forming inverter with open-loop.
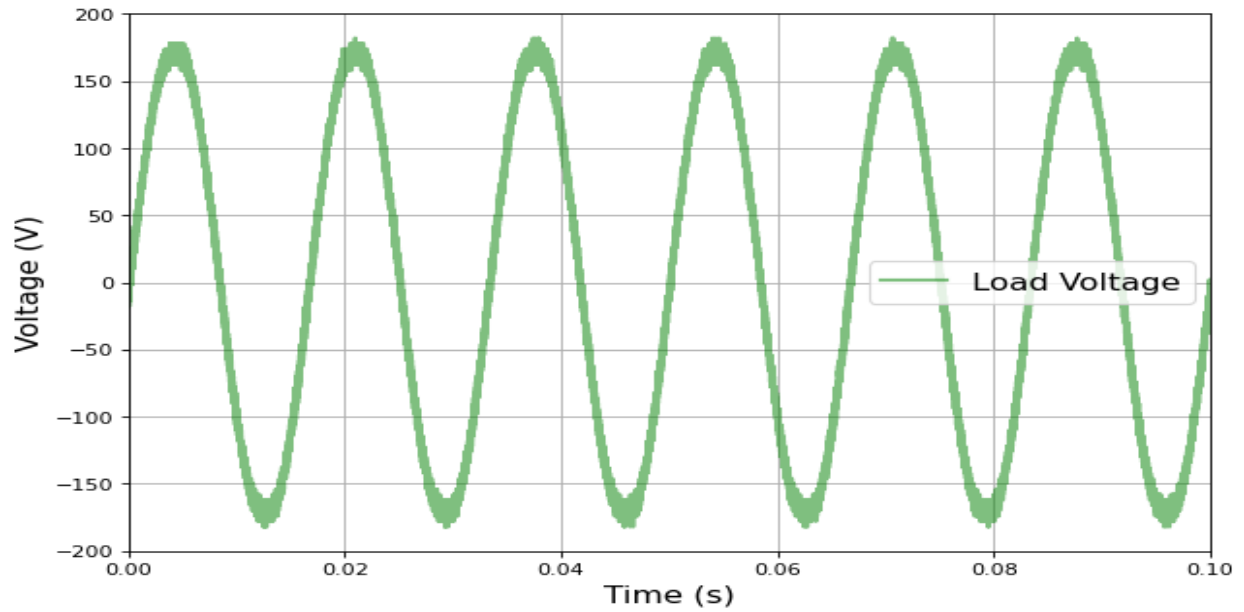
Figure 4.15 Load voltage of the grid-forming inverter with a closed-loop control of the DC/DC boost converter.
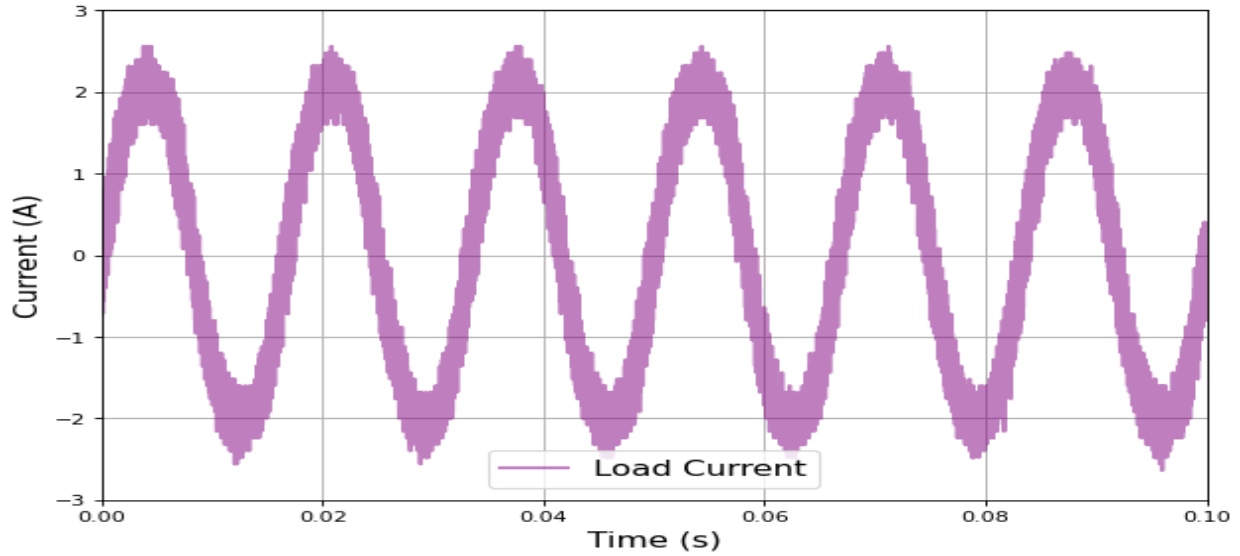
Figure 4.16 Load current of the grid-forming inverter with a closed-loop control of the DC/DC boost converter.
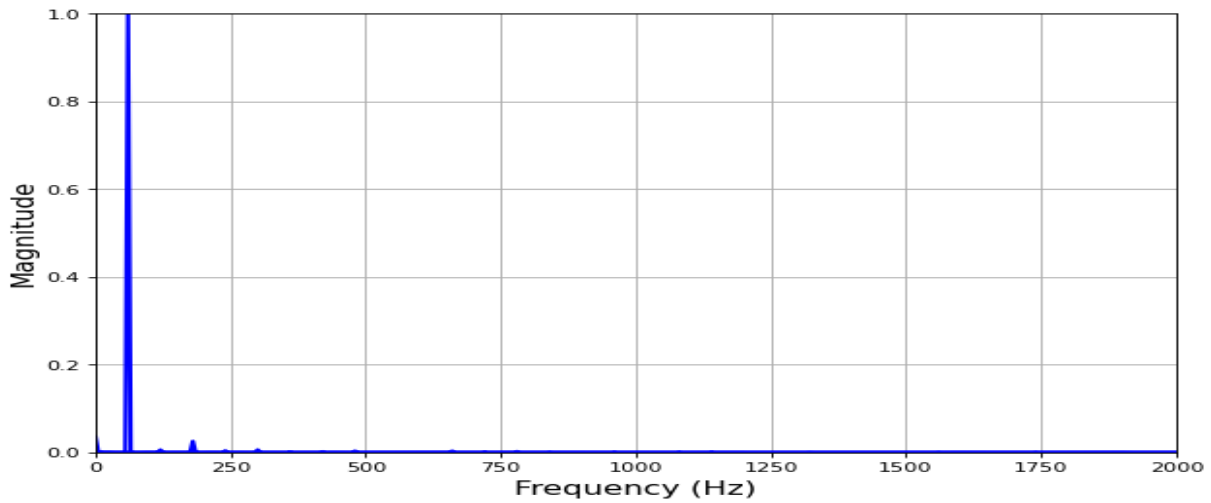
Figure 4.17 FFT of the output voltage waveform of the grid-forming inverter with open-loop control. The Total Harmonic Distortion (THD) is 0.07%.

Figure 4.21 shows the step response of the system when the DC-link voltage reference is changed from 20 V to 50 V. Figure 4.22 shows the same waveforms in the steady state. In these two figures, V_load is the load voltage, I_load is the load current, and Vdc_boost is the DC-link voltage.
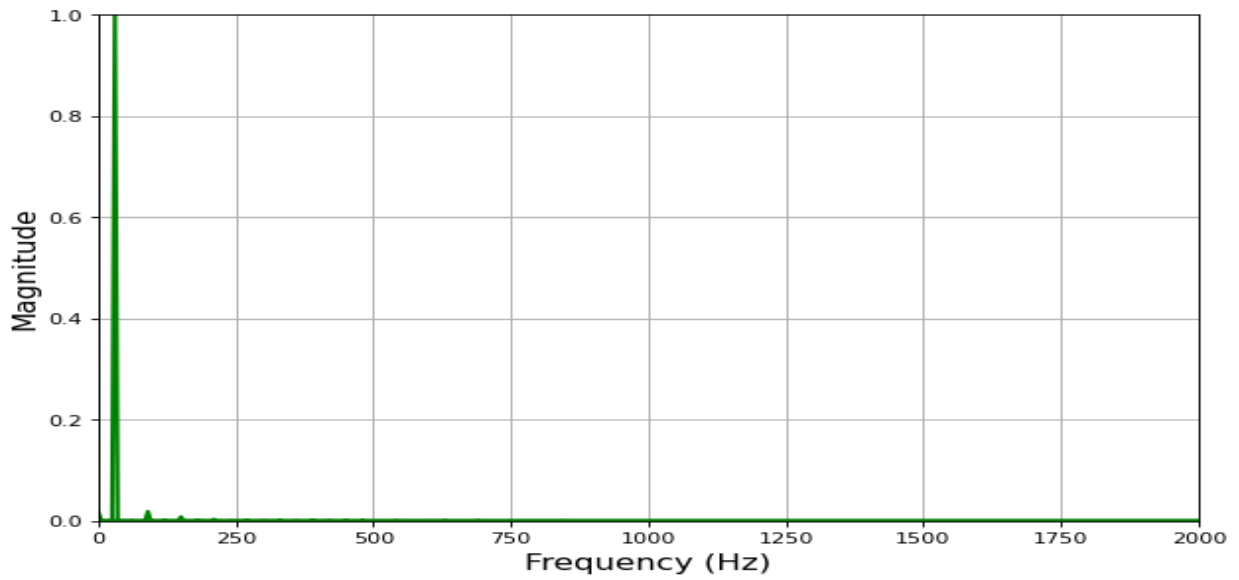
Figure 4.18 FFT of the output current waveform of the grid-forming inverter with open-loop control. The THD is 0.17%.
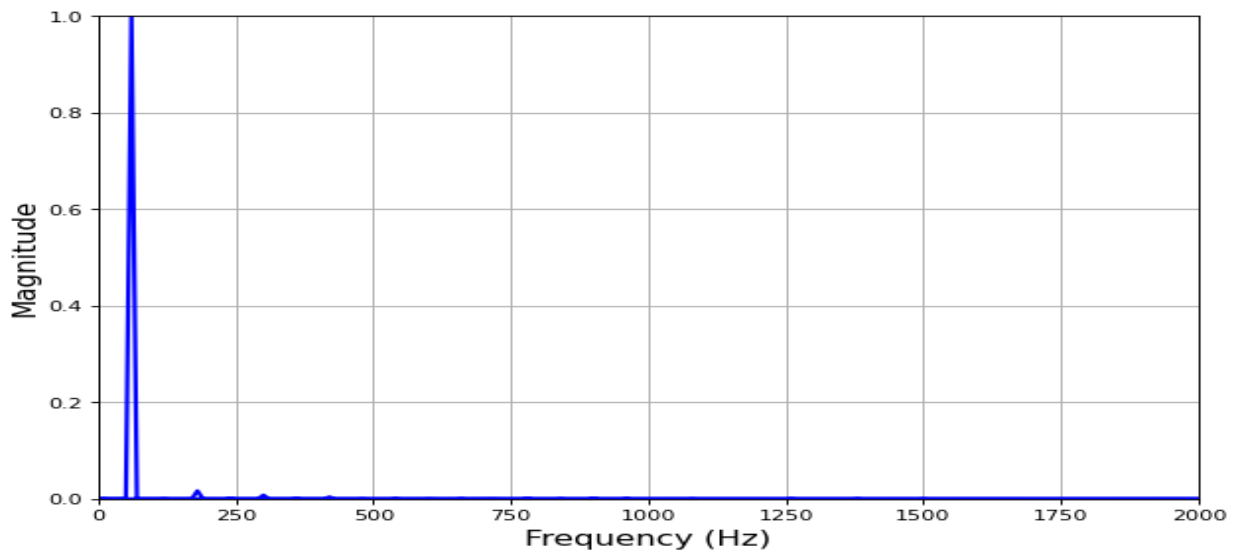
Figure 4.19 FFT of the output voltage waveform of the grid-forming inverter with a closed-loop control of the DC/DC boost converter. The THD is 0.16%.
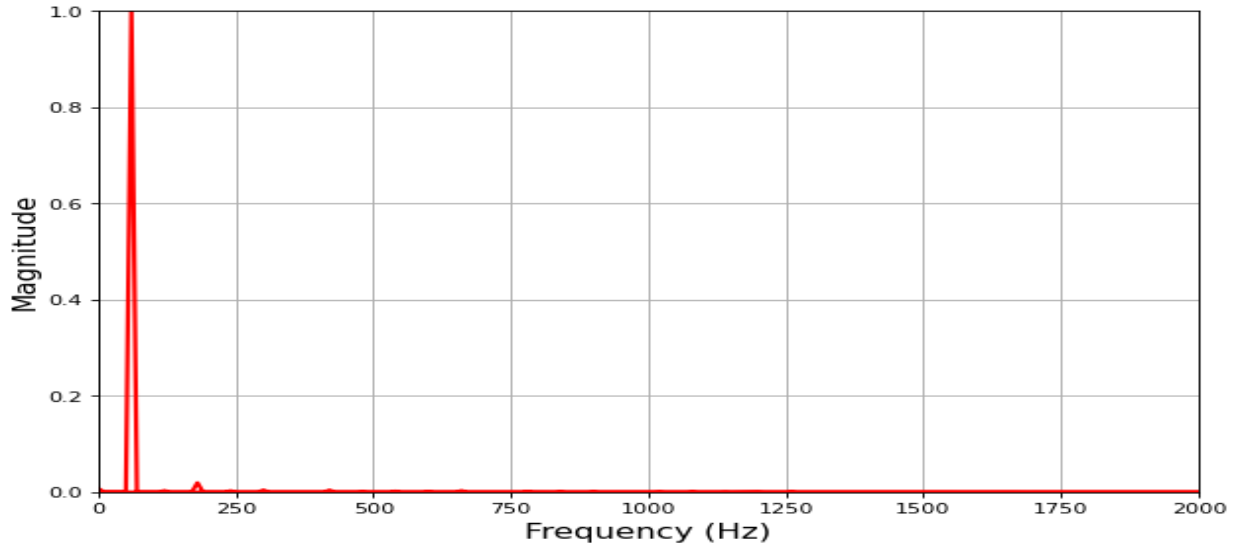
Figure 4.20 FFT of the output current waveform of the grid-forming inverter with a closed-loop control of the DC/DC boost converter. The THD is 0.17%.
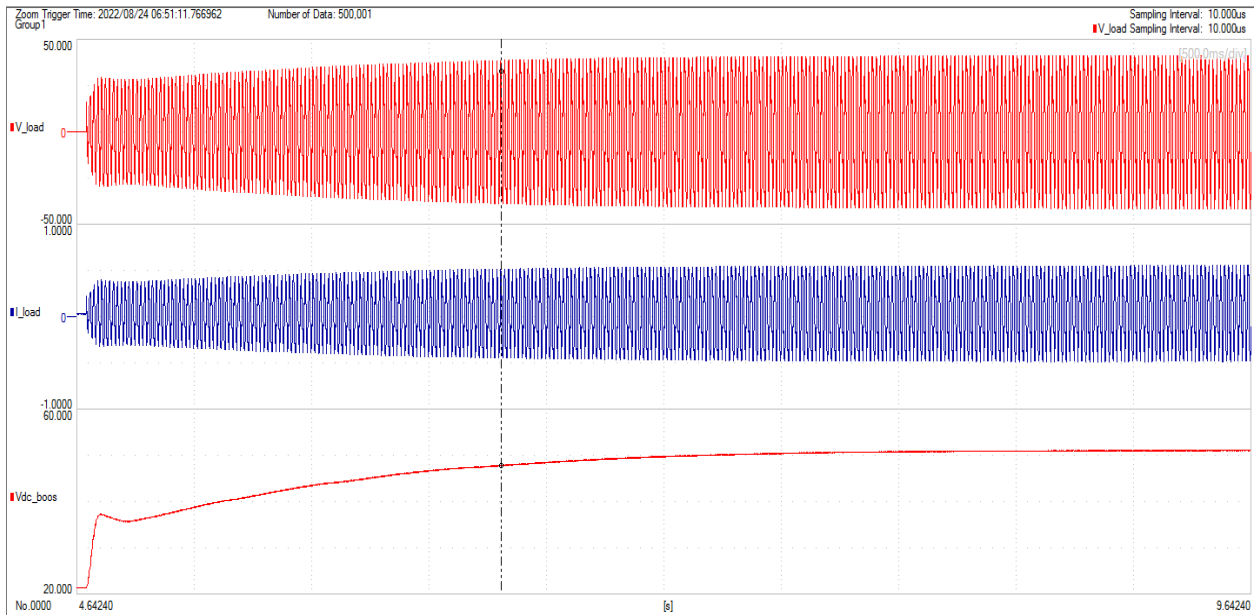
Figure 4.21 Step response of the grid-forming inverter with a closed-loop control when reference DC-link voltage is changed from 20 V to 50 V.
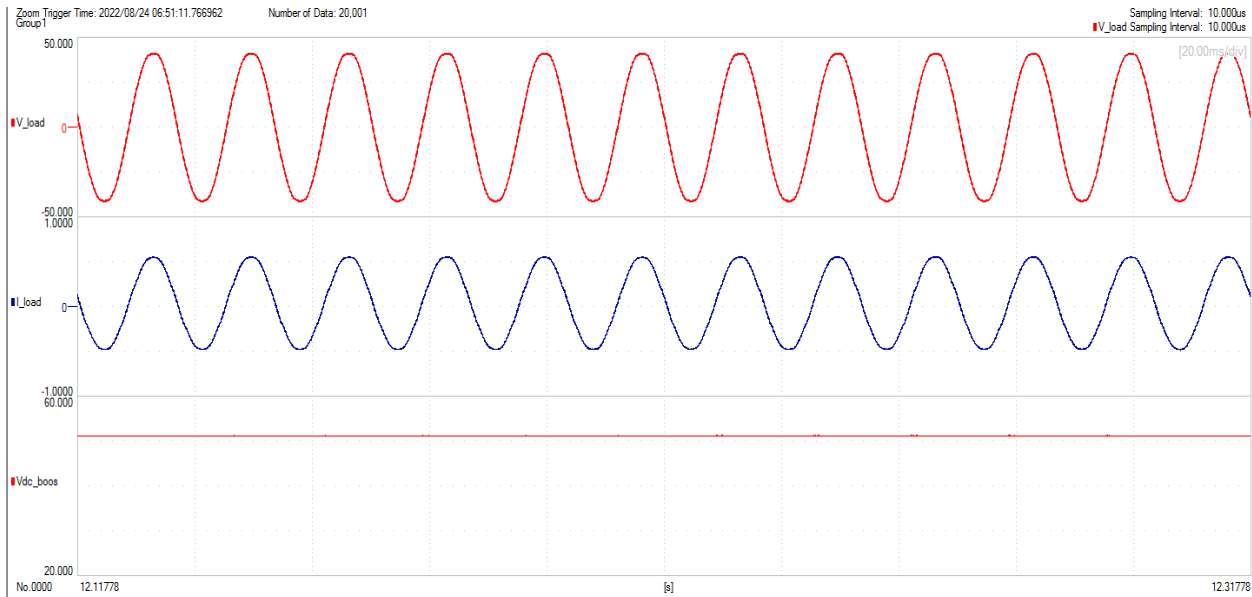
Figure 4.22 Step response of the grid-forming inverter with a closed-loop control when reference DC-link voltage is changed from 20 V to 50 V; a steady-state result.

The load voltage and current in Figure 4.22 are captured for low voltage of 30 V RMS, and low load current of 0.3 A RMS. This test is done at low voltage and low load because of safety reasons. The step response for the DC-link could not be performed from 0 to 200 V, as it requires a significant amount of energy, which is beyond the controller capability. In practice, the dc-link voltage changes in a ramp fashion and not in a step fashion with the load is not being connected. However, to show that the closed-loop control for the boost converter is working properly, a step response must be performed. Therefore, the test is done at low voltage from 20 to 50 V as shown in Figure 4.21. Now, at low loads, we have smoother current than at higher loads. This is because as the load increases the output inverter current increases and the filter inductance gets saturated. Thus, its filtering ability reduces. This explains why the load waveforms in Figures 4.15 and 4.16 are more distorted than the ones in Figure 4.22.

Figure 4.25 shows the whole experimental setup in detail with the connections.

4.3 Transfer function

The experimentally captured input and output data of the converter are used to estimate the transfer function of the system using the same method in 3.3.3.5. Equation (4.1) shows the estimated fifth-order transfer function using the System Identification Toolbox in MATLAB. The

estimated transfer function of the converter gives an output that fits[10] 96% to the measured output data. Figure 4.23 shows the frequency response of the estimated transfer function. Figure 4.24 shows the transfer function estimated from the experimentally collected data in comparison with the one that was previously estimated from the simulation results' data. The comparison shows that the two frequency responses are stable, and their gains almost match each other.

$$\frac{V_{load}}{V_{bat}} = \frac{5.33 \times 10^{15} s - 2.5 \times 10^{14}}{s^5 + 1.9 \times 10^4 s^4 + 4.84 \times 10^8 s^3 + 4.02 \times 10^{12} s^2 + 6.88 \times 10^{13} s + 5.71 \times 10^{17}} \tag{4.1}$$
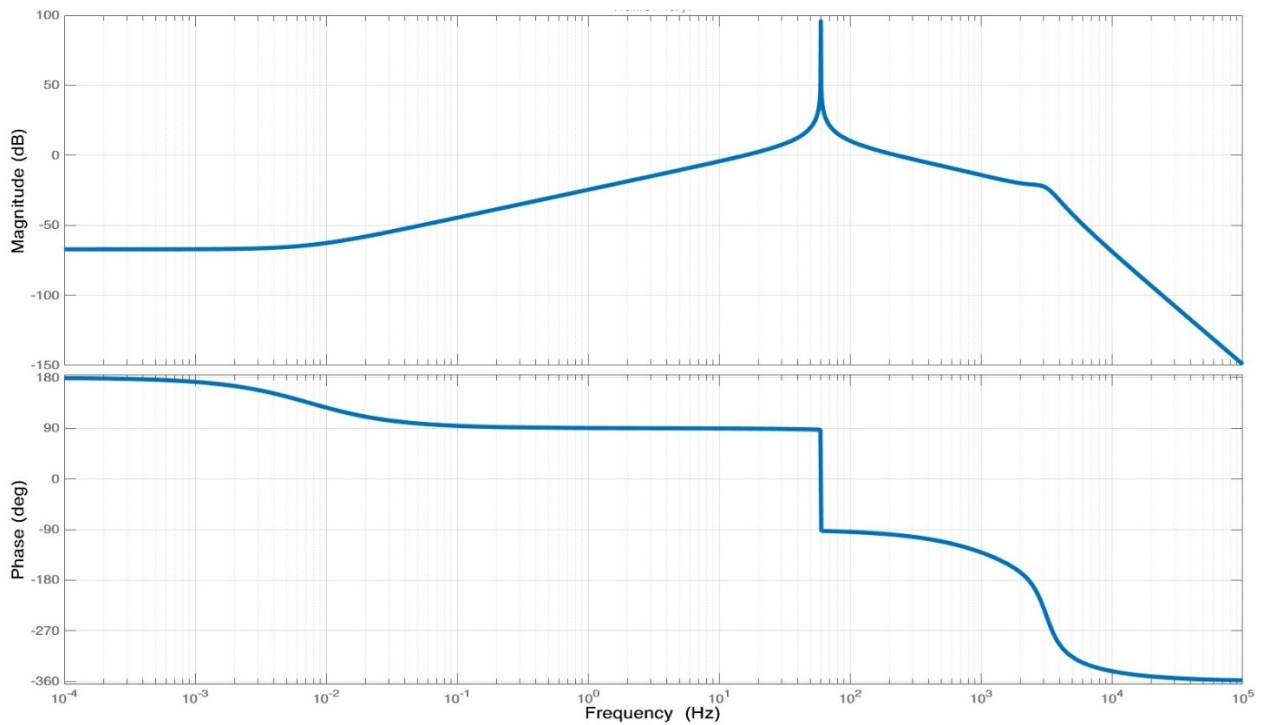
Figure 4.23 Frequency response of the fifth order estimated transfer function; 96% fit to the output.

---

[10] See section 3.3.3.6 for the explanation of fitting.
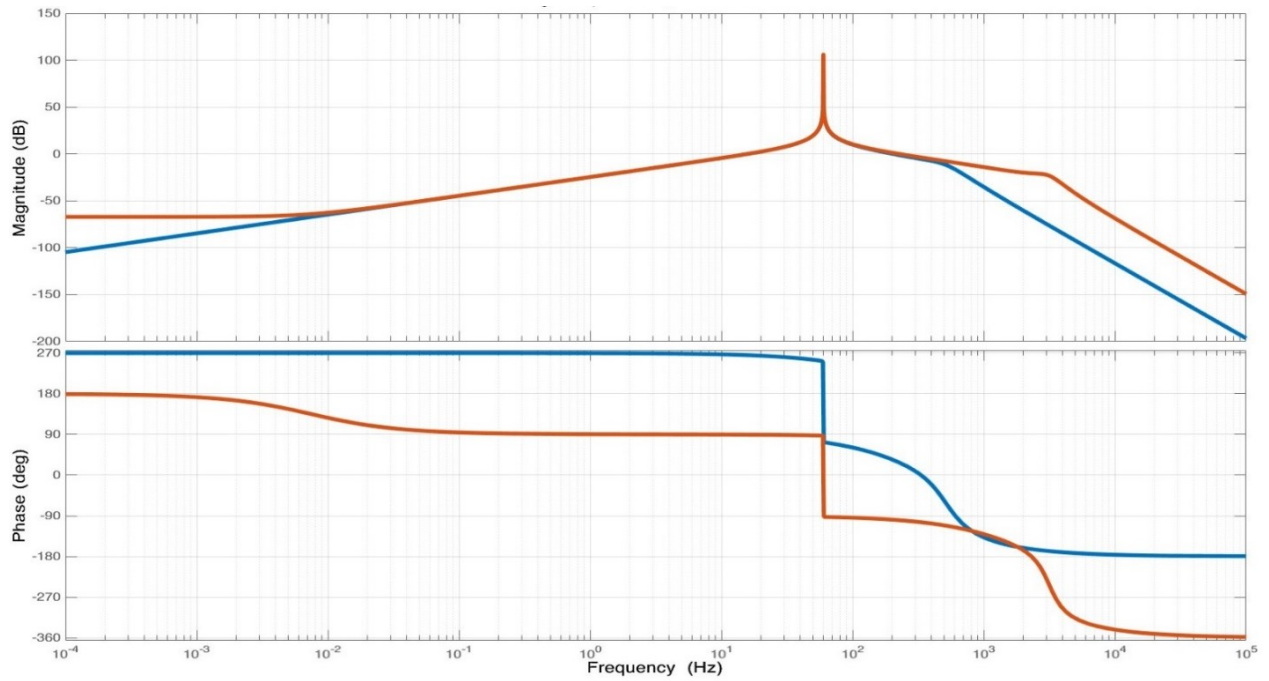
Figure 4.24 Frequency response comparison of the 5th order estimated transfer functions from the simulation data (blue trace) as in (3.59) and from the experiment data (orange trace) as in (4.2).
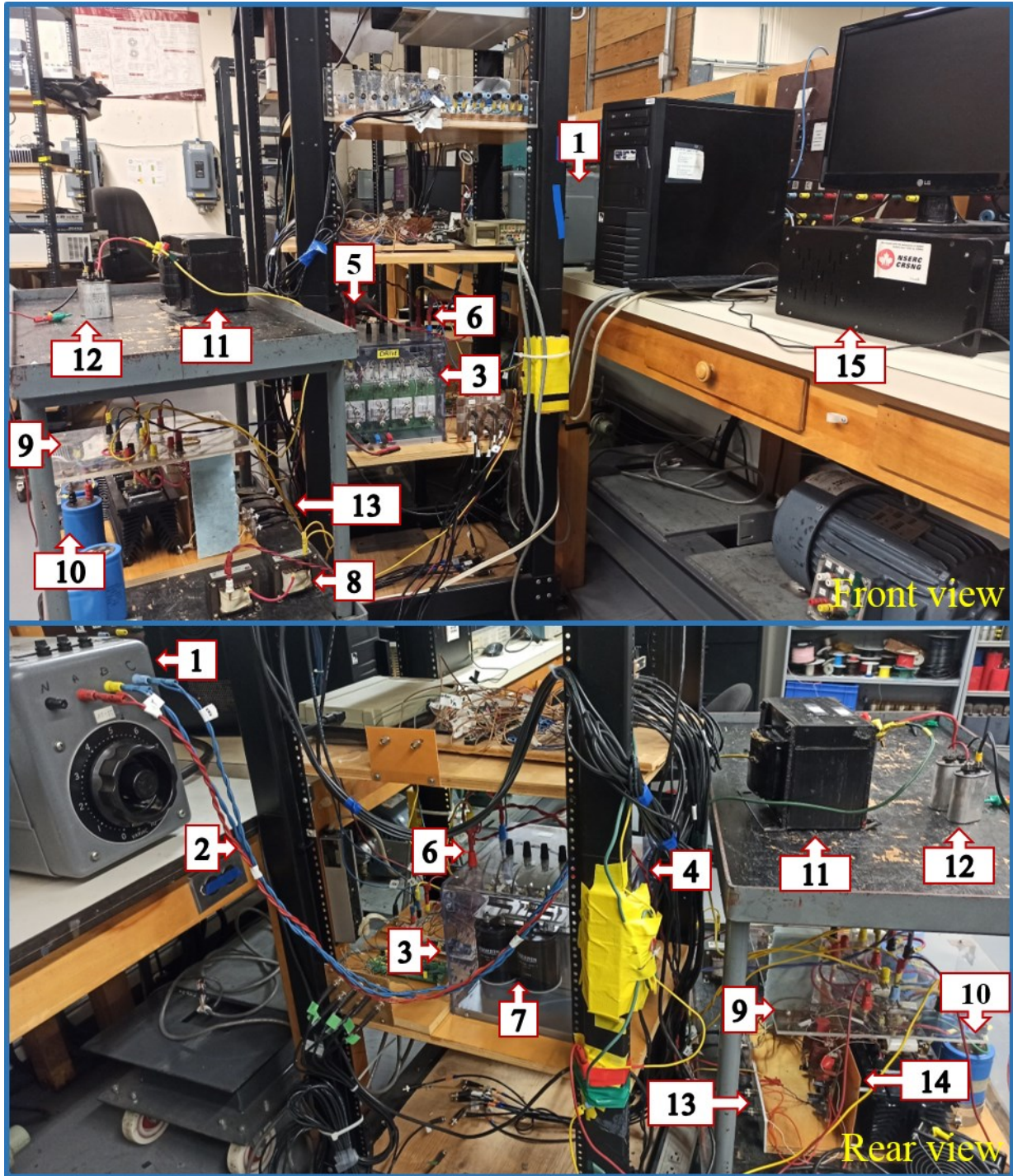
Figure 4.25 Experimental setup; (1) Variac, (2) AC 3-φ output of variac, (3) Semiteach inverter, (4) AC 3-φ input of rectifier, (5) 3-φ diode rectifier, (6) DC output of rectifier, (7) C_{reg}, (8) L_{boost}, (9) 3-φ inverter (one leg is used for the boost converter and the other two legs are used for the single-phase inverter), (10) $C_{dc\text{-}link}$, (11) L_{filt}, (12) C_{filt}, (13) Switching pulses input, (14) Gate drive, (15) OPAL-RT.

4.4 Summary

In this chapter, an experimental setup is performed for the third mode of operation, which is the battery system feeds the house loads. The purpose of the experiments was to see if it is possible to make a grid-like voltage in real conditions with this topology. This goal is reached through this experiment. Moreover, by using the input and output data of the built grid-forming inverter, the transfer function of the system is estimated. As can be seen from the results, both time-domain and frequency-domain models work well and as expected.

Chapter 5 Conclusion and Future Works

5.1 Conclusion

This research is done to explain the performance of the solar power system of the FBL, forthrightly. The simulation results have shown that the topologies and controller circuits used in this research adequately and precisely show how the system performs in different modes. The results derived from the experimental setup were exactly as expected and matched the simulation results. It is also seen that it is possible to estimate the transfer function of a system by just knowing the input and output signals. The estimated transfer function is very close to the one calculated analytically.

A summary of Chapters 1 to 4 is presented below.

Chapter 1. In this chapter, a review of the global warming issue is done. The suggested methods to reduce carbon footprint are mentioned. The concept of NZEB is elaborated on and followed by examples of NZEBs in Canada and the case study of this research.

Chapter 2. In this chapter, the related material and previous work available in the literature are studied. Different types of power converters are studied. As this research is done on the electrical aspects of the FBL, the types of converters that are used specifically in this thesis are discussed along with the available control methods.

The topologies available in the literature for the grid-forming inverter, which is the main converter designed in this research, are investigated and the proposed topology is brought at the end of this chapter. This topology doesn't have a transformer and is smaller in size. It also has the advantage of being easier to implement.

Chapter 3. In this chapter, the electrical characteristics of the research house and its devices are presented. Based on the conditions of different parts of the system, different modes of operation can be defined. Out of all possible modes, three modes of operation 1) grid feeds the load, 2) grid charges the battery, and 3) battery feeds the load are studied, designed, and simulated. The simulation results are shown throughout the chapter. The simulation results for each mode of operation match the prior expected trends. The frequency domain modeling of the two operating modes in which the grid-forming inverter is involved is done. The estimated transfer function using

the System Identification Toolbox in MATLAB, which considers only the input and output signals and sees the converter as a black box, is observed to match the analytically derived transfer function.

Chapter 4. In chapter 4, a setup is prepared for the third mode of operation (battery feeds the load) at the PEER group laboratory, Concordia University. The process and the results of the experiments are presented. The estimated transfer function from the experimental data is compared with the one estimated from the simulated data. The results obtained in this chapter validate the simulation results.

5.2 Future Work

The proposed future work of this thesis is to design other modes of operation that may occur under different circumstances, which were not considered in this thesis. Furthermore, the experiments can be done at the Future Buildings Laboratory with the solar power system installed in place. In the future, the designed models can be validated by the data obtained from the performance of the solar house in real life.

References

[1] "Global Temperatures," Earth Observatory, [Online]. Available: https://earthobservatory.nasa.gov. [Accessed August 2022].

[2] "Overview: Weather, Global Warming, and Climate Change," NASA, [Online]. Available: https://climate.nasa.gov. [Accessed 20 04 2022].

[3] "United Nations Climate Change," 2018. [Online]. Available: http://www.unfccc.int. [Accessed 2022].

[4] B. E. E. Taskgroup, "Building Energy Performance Metrics," International Energy Agency, 2015.

[5] P. Nejat, F. Jomehzadeh, M. M. Taheri, M. Gohari and M. Z. A. Majid, "A global review of energy consumption, CO2 emissions and policy in the residential sector (with an overview of the top ten CO2 emitting countries)," *Renewable and Sustainable Energy Reviews,* vol. 43, pp. 843-862, 2015.

[6] W. O'Brien and A. Athienitis, Modeling, design, and optimization of net-zero energy buildings, John Wiley & Sons, 2015.

[7] P. Torcellini, S. Pless and M. Deru, "Zero Energy Buildings: A Critical Look at the Definition," in *ACEEE Summer Study*, Pacific Grove, 2006.

[8] "Progress towards Canada's greenhouse gas emissions reduction target," Government of Canada, March 2021. [Online]. Available: https://www.canada.ca/en/environment-climate-change/services/environmental-indicators/progress-towards-canada-greenhouse-gas-emissions-reduction-target.html. [Accessed February 2022].

[9] "PVPS Annual Report," International Energy agency, 2021.

[10] V. Dermardiros, *Data-Driven Optimized Operation of Buildings with Intermittent Renewables and Application to a Net-Zero Energy Library,* Montréal: Concordia University, 2020.

[11] "LEED," Canada Green Building Council, [Online]. Available: http://www.cagbc.org. [Accessed 2022].

[12] "Building Integrated Combined Solar Thermal and Electric Generation Demonstration Project at Concordia University," NSERC Solar Buildings Research Network.

[13] "Bibliothèque de Varennes," [Online]. Available: https://biblio.ville.varennes.qc.ca/. [Accessed 2022].

[14] N. R. Canada, "R-2000 Net-Zero Energy Pilot Case study," National Resources Canada, 2019.

[15] M. Abtahi, A. Athienitis and B. Delcroix, "Control-oriented thermal network models for predictive load management in Canadian houses with on-Site solar electricity generation: application to a research house," *Journal of Building Performance Simulation,* 2021.

[16] F. Blaabjerg, Control of Power Electronic Converters and Systems, Elsevier, 2018.

[17] N. Mohan, T. Undeland, M. Robbins and W. P., Power Electronics - Converters, Applications, and Design (3rd Edition), John Wiley & Sons, 2003.

[18] R. Strzelecki and G. S. Zinoviev, "Overview of Power Electronics Converters and Control," in *Power Electronics in Smart Electrical Energy Networks*, London, Springer, 2008, pp. 55-105.

[19] C. Shah, J. D. Vasquez-Plaza, D. D. Campo-Ossa, J. F. Patarroyo-Montenegro, N. Guruwacharya, N. Bhujel, R. D. Trevizan, F. A. Rengifo, M. Shirazi, R. Tonkoski, R. Wies, T. M. Hansen and P. Cicilio, "Review of Dynamic and Transient Modeling of Power Electronic Converters for Converter Dominated Power Systems," *IEEE Access,* vol. 9, pp. 82094-82117, 2021.

[20] J. Choi, A. Khalsa, D. A. Klapp, S. Baktiono and M. S. Illindala, "Survivability of Prime-Mover Powered Inverter-Based Distributed Energy Resources During Microgrid Islanding," *IEEE Transactions on Industry Applications,* vol. 55, no. 2, pp. 1214-1224, 2019.

[21] R. H. Lasseter, "Microgrids," in *IEEE Power Engineering Society Winter Meeting*, 2002.

[22] R. H. Lasseter and P. Paigi, "Microgrid: A Conceptual Solution," in *IEEE 35th Annual Power Electronics Specialists Conference*, 2004.

[23] P. Piagi and R. H. Lasseter, "Autonomous control of microgrids," in *IEEE Power Engineering Society General Meeting*, 2006.

[24] Q. Liu, T. Caldognetto and S. Buso, "Review and Comparison of Grid-Tied Inverter Controllers in Microgrids," *IEEE Transactions on Power Electronics,* vol. 35, no. 7, pp. 7624-7639, 2020.

[25] P. C. Loh and D. G. Holmes, "Analysis ofmultiloop control strategies for LC/CL/LCL-filtered voltage-source and current-source inverters," *IEEE Transactions on Industrial Applications,* vol. 41, no. 2, pp. 644-654, 2005.

[26] Y. Han, Z. Li and J. M. Guerrero, "Dynamic Evaluation of LCL-type Grid-Connected Inverters with Different Current Feedback Control Schemes," in *9th International Conference on Power Electronics and ECCE Asia*, Seoul, 2015.

[27] S. N. Afrasiabi, C. Lai and P. Pillay, "Dead Time Analysis of a Power-Hardware-in-the-Loop Emulator for Induction Machines," in *47th Annual Conference of the IEEE Industrial Electronics Society*, Toronto, 2021.

[28] P. Pillay and R. Krishnan, "Modeling, simulation, and analysis of permanent-magnet motor drives. I. The permanent-magnet synchronous motor drive," *IEEE Transactions on Industry Applications,* vol. 25, no. 2, pp. 265-273, 1989.

[29] Y.-Y. Tzou, "DSP-based fully digital control of a PWM DC-AC converter for AC voltage regulation," in *Power Electronics Specialist Conference*, Atlanta, 1995.

[30] P. Tenti, T. Caldognetto, S. Buso and A. Costabeber, "Control of utility interfaces in low voltagemicrogrids," in *IEEE 5th International Symposium in Power Electronics Distribution and Generation Systems*, 2014.

[31] S. Yazdani, M. Ferdowsi, M. Davari and P. Shamsi, "Advanced Current-Limiting and Power-Sharing Control in a PV-Based Grid-Forming Inverter Under Unbalanced Grid Conditions," *IEEE Journal of Emerging and Selected Topics in Power Electronics,* vol. 8, no. 2, pp. 1084-1096, 2020.

[32] "Grid-Forming Inverter Controls," NREL, [Online]. Available: https://www.nrel.gov. [Accessed 2022].

[33] G. Song, B. Cao and L. Chang, "Review of Grid-forming Inverters in Support of Power System Operation," *Chinese Journal of Electrical Engineering,* vol. 8, no. 1, pp. 1-15, 2022.

[34] U. Peter, N. Maria, S. Philip and W. Friedrich, "Overview on Grid-Forming Inverter Control Methods," *Energies,* vol. 13, no. 10, 2020.

[35] L. S., S. J., E. B., B. T. and P. D., "Substitution of synchronous generator based instantaneous frequency control utilizing inverter-coupled DER," in *7th International Symposium on Power Electronics for Distributed Generation Systems (PEDG)*, Vancouver, 2016.

[36] T. U. B., R. M. A. B., H. L. J. and M. Kashif, "A review of droop control techniques for microgrid," *Renewable and Sustainable Energy Reviews,* vol. 76, pp. 717-727, 2017.

[37] M. O., D. S. and S. J. A., "Evaluation of Virtual Synchronous Machines With Dynamic or Quasi-Stationary Machine Models," *IEEE Transactions on Industrial Electronics,* vol. 64, no. 7, pp. 5952-5962, 2017.

[38] L. A. B. Torres, J. P. Hespanha and J. Moehlis, "Power supply synchronization without communication," in *IEEE Power & Energy Society General Meeting*, San Diego, 2012.

[39] Z. L., H. L. and N. H.-P., "Power-synchronization control of grid-connected voltage-source," *IEEE Transactions on Power Systems,* vol. 25, pp. 809-820, 2010.

[40] R. D., A. M. Cantarellas, R. E., I. Candela and P. Rodriguez, "An active power synchronization," in *IEEE Power & Energy Society General*, National Harbor, 2014.

[41] M. F., D. F., H. G., H. D. J. and V. G., "Foundations and challenges of low-inertia systems," in *Power Systems Computation Conference (PSCC)*, Dublin, 2018.

[42] A. Alberto, "Arrangement of Parallel Static AC Power Sources Proportions". United Stated of America Patent 3864620A, 11 September 1973.

[43] K. T. and H. S., "Parallel operation of voltage source inverters," *IEEE Transactions on Industrial Applications,* vol. 24, no. 2, pp. 281-287, 1988.

[44] C. M. C., D. D. M. and A. R., "Control of parallel connected inverters in standalone AC supply," *IEEE Transactions on Industry Applications,* vol. 29, pp. 136-143, 1993.

[45] H. Zhang, W. Xiang, W. Lin and J. Wen, "Grid Forming Converters in Renewable Energy Sources Dominated Power Grid: Control Strategy, Stability, Application, and Challenges," *Journal of Modern Power Systems and Clean Energy,* vol. 9, no. 6, pp. 1239-1256, 2021.

[46] C. Yang, L. Huang, H. Xin and P. Ju, "Placing Grid-Forming Converters to Enhance Small Signal Stability of PLL-Integrated Power Systems," *IEEE Transactions on Power Systems,* vol. 36, no. 4, pp. 3563-3573, 2021.

[47] R. Rye, R. Burgos, Y. Tang, Q. Lin and D. Boroyevich, "AC Impedance Characterization of a PV Inverter with Grid-Forming Control," in *2020 IEEE Energy Conversion Congress and Exposition (ECCE)*, Detroit, 2020.

[48] F. Sadeque and F. Fateh, "On Control Schemes for Grid-Forming Inverters," in *IEEE Kansas Power and Energy Conference (KPEC)*, Manhattan, 2022.

[49] PYLONTECH, *Low Voltage Energy Storage System -For Residential and SME.*

[50] IEEE, *IEEE Recommended Practice and Requirements for Harmonic Control in Electric Power Systems,* IEEE SA, 2014.

Appendix

The parameters used for the Lithium-ion Battery block in PSIM are calculated based on the Lithium-ion Battery Model Tutorial available in PSIM software and the characteristics available in the datasheet of the commercial battery Pylontech - US3000C LiFePO$_4$. The characteristics obtained from the battery are brought in Table A.1.

Table A.1 Characteristics of the commercial battery [49].

Basic Parameters	US3000C
Nominal Voltage（V）	48
Nominal Capacity (Wh)	3552
Usable Capacity (Wh)	3374.4
Dimension（mm）	442*420*132
Weight（Kg）	32
Discharge Voltage（V）	44.5 ~ 53.5
Charge Voltage（V）	52.5~53.5
Charge / Discharge Current（Amps）	37 (Recommend)
	74 - 89 (Max@60s)
	90 - 200 (Peak@15s)
Communication Port	RS485，CAN
Single string quantity(pcs)	16
Working Temperature/℃	0~50
Shelf Temperature/℃	-20~60
Humidity	5%~95%
Altitude (m)	<4,000
Design life	15^+ Years（25℃/77℉）
Cycle Life	>6,000, @25℃（EOL@60%*）
Authentication Level	VDE2510-50 / IEC62619 /UL/CAN/ANSL1973 UL/CAN/ANSL9540A / IEC61000-6-2/3 / UN38.3
Feature	Pre-Charge Dual-active protection Flexible current steps Dry contact wake up

At the beginning of the discharge process of a Lithium-ion battery, the battery voltage starts to decrease exponentially until it reaches a value that is called the exponential point voltage E_{top}. At this point, the capacity of the battery is equal to the exponential point capacity Q_{top}. After this point, the change in the battery voltage is almost linear until the battery voltage equals its nominal voltage. After this point, the decrease in voltage occurs exponentially again. The above explanation can be seen in the discharge curve shown in Figure A.1.
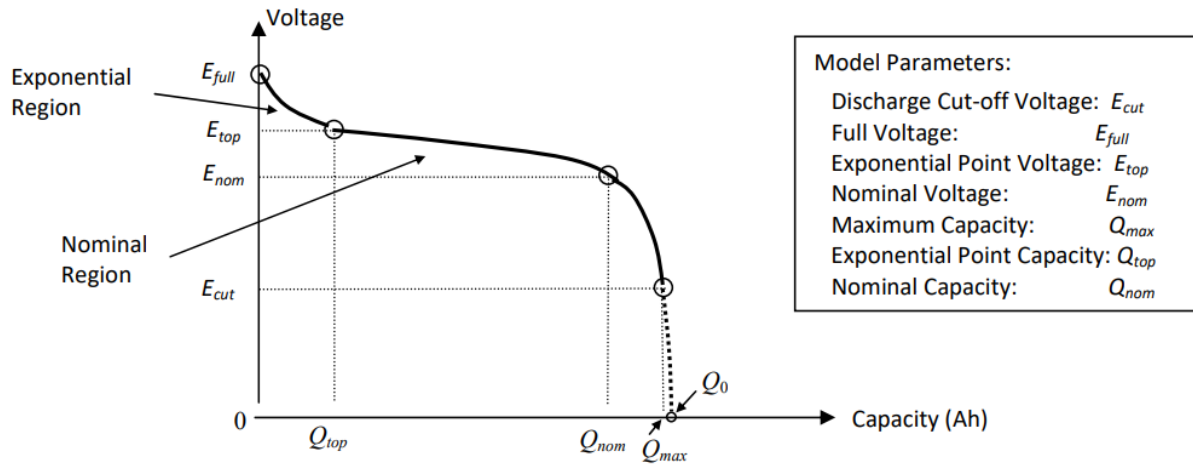
Figure A.1 A typical discharge curve of a Lithium-ion battery.